# Department of Precision and Microsystems Engineering

Design of pH sensor for liquid cell Transmission electron microscopy

Deep Patel

Report no   : 2020.031
Coach   : Dr. H.H. Pérez Garza
Professor   : Dr. M.K. Ghatkesar
Specialisation   : Micro and Nano Engineering
Type of report   : Master Thesis
Date   : 19 October 2020

TUDelft
Delft
University of
Technology

Challenge the future
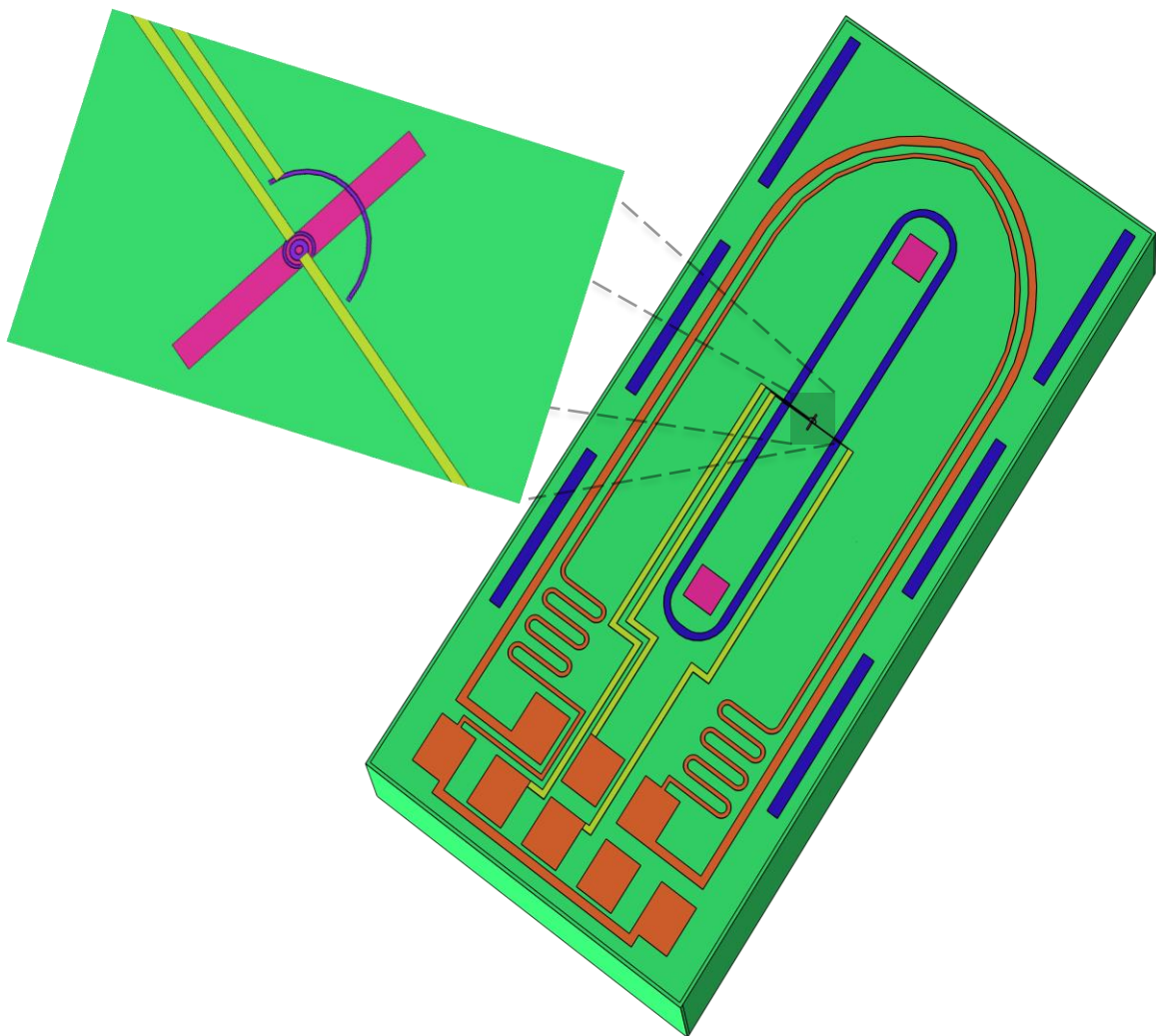
Design of pH sensor for liquid cell Transmission electron microscopy

by

Deep Patel

Master of science thesis

to be defended publicly on Friday October 30, 2020 at 13:00.

Student Number: 4804465
Project duration: September 2, 2019 – October 30, 2020
Thesis committee: Dr. Ivan Buijnsters   3mE, PME, Micro and Nano Engineering
         Dr. M. K. Ghatkesar   3mE, PME, Micro and Nano Engineering
         Dr. Y. Gonzalez Garcia   3mE, MSE, Materials Science and Engineering
         Dr. H. H. Pérez Garza   DENS Solutions B.V.

An electronic version of this thesis is available at http://repository.tudelft.nl/.

ABSTRACT

Electron microscopy has enabled us to visualize objects that are not observable with a light microscope. With Transmission electron microscope observation up to subatomic level is possible. Generally, the sample is under vacuum in an electron microscope. But in real life sample is under influence of environmental conditions like liquid, gas, temperature. Development in Micro electro mechanical systems (MEMS) has made it possible to make nanocell, which encloses sample and provide different stimuli like gas, liquid, voltage, temperature. This allows real-time changes in the sample in different environmental conditions. This has a wide area of application in the field of physics, chemistry, biology, and material science.

Imaging in liquid environment contains encapsulated liquid (liquid nano cell), which allows high energy electron beam passes through thin windows and reaching to detectors. While the electron beam passing through the liquid, the interaction of both splits water and generates radiolysis products. These radiolysis products contain gases, ions, radicals, and other chemical compositions. These products affect the chemistry in liquid and therefore the observations in the experiment. So it is important to quantify these generated species. One of the species that is generated due to radiolysis is H^+ ion. Because of this, pH of the liquid changes. Numerical studies are available to quantify this pH change but species generation data is interpolated to several orders of magnitude and very limited experimental work is available. Especially for pH change, no experimental attempts are found.

The goal of this thesis was to measure pH change due to radiolysis. For this two problems need to tackle simultaneously, making micro size pH sensor on-chip and trying to find out what species due to radiolysis has the potential to affect pH measurements. Radiolysis generates 15 species for pure water and characterizing all of them is difficult. So here approach is taken to measure species effect just outside the electron beam area, which reduces to only 5 species to consider. Species generation and its effect on the platinum electrode are analyzed. For Ultra pure water (pH 7.2), the measured voltage shift was negative and for pH 4.01 (Buffer solution) and pH 2.45 (H_2SO_4 solution), it was positive with increase in dose rate. The reason for this could be the generation of excess H_2O_2 for acidic solutions and generation of excess O_2^- for neutral pH solutions. So it is important to shield the effect of these two species for successful pH measurement just outside the beam region. The optimization code is written to decide the place and thickness of two pH measuring electrodes for maximum H^+ ion detection and minimum effect for other species. From literature it is found that IrO_2 has selectivity of 10^{-4} for H_2O_2. Results from the optimization code conclude that the sensing layer should have minimum selectivity for $O_2^- = 0.1$, to measure any meaningful pH change outside the beam area.

pH sensing characteristics of the Platinum electrode reveal a maximum error of 0.4 pH in measurement. Manufacturing of the Iridium oxide layer is done to see pH sensing properties. Error estimation concludes that due to Iridium oxide with the current

manufacturing technique maximum error is 0.4 pH. However, according to simulations outside the beam area, maximum pH change is 1.34 pH. From the optimization code dimensions of two pH sensing electrodes are decided. Considering maximum error from pH measurement experiments and error from species interference from simulations, an electrode configuration has been designed. The design allows pH measurement for the dose rate $5 * 10^7$ Gy/s and above for initial pH of solution ranging from 6 to 8.

PREFACE

This thesis represents my results for MSc project of pH measurement in liquid nanocell. Most of the work is done at DENSsolutions B.V. and some work within High-Tech Engineering department at TU Delft.

Many people have helped me during my thesis, without whom this project would not have been possible.

First of all, I would like to appreciate my guides Murali Ghatkesar (TU Delft) and Hugo Perez Garza (DENSsolutions) for their guidance. Hugo has been my supervisor from the company, who has pitched this very interesting project to me. His guidance and recommendations have been helpful for experiments and meetings with him are inspiring mainly because of his positive attitude and the freedom he gave to play around. I would like to thank him for his kind support and patience. Murali is my guide from TU Deft, and bi-weekly meeting with him has always been filled with discussion about fundamentals and understanding of the subject. His right questions and guidance have made me think and understand this subject better.

I would like to thank Anne Beker and Hongyu Sun from DENSsolutions for every planned/ unplanned meeting that helped me directly or indirectly. Throughout this project, Anne has helped me understand electrochemistry and trained me to use experimental setup and SEM. Technical discussions with her have guided me with many answers and sometimes questions that are useful to make some conclusions in this project. Hongyu's knowledge about microscopy and support during my experiments has facilitated thesis work. His wide knowledge of literature has been useful to understand different papers in this field. Overall genuine support from both of them makes this thesis work possible.

Additionally, colleagues at DENSsolutions has helped me at many points to do experiments. It is because of them doing thesis was fun and exciting with getting a lot of leanings. Tijn van Omme has helped me doing TEM experiments, Raman analysis, and his suggestions during stream meetings have been insightful. Ronald Spruit has helped to do Raman analysis, Hanieh Mastyani trained me with the White light interferometer, Mathilde Lemang checked and corrected my literature review report, Magda Wierzba and Ton Kerpel has been there when I need anything from the warehouse, Christian Deen, Yevheniy Pivak, Merijn Pen, Diederik Morsink, Daan Bormans, Ronald Marx, Dan Zhou, Olaf Weller, Berend Bormans, Ben Bormans, Qiang Xu, Robert Endert and Tom van Osch has ensured great environment at workplace. I thank all of them for accommodating me at DENSsolutions and ensuring a wonderful time at the company.

I would also like to thank all my friends for reaching out for hangouts and make me remind to take breaks. Additionally, I am really grateful to my parents who have shown great confidence in me and their unconditional and well-needed support.

CONTENTS

1

INTRODUCTION

Transmission Electron Microscopy (TEM) allows study of objects at the nano scale. Eliminating aberration problems with aberration correction enhances the ability to go up to subatomic level. TEM is mainly composed of a vacuum chamber with typically electron beam source (electron gun) of 100 – 300 KV. Vacuum chamber ensures minimum interference of electron beam with other molecules. The electron beam is directed and focused by magnetic lenses. Sample holder holds sample at correct location and angle of observation. The sample is very thin (few hundred nano meter) so that the electron beam could pass through. Interaction of electron beam and sample deflects the electron beam that is captured by detectors to create image of sample. A schematic of TEM is shown in figure 1.1a. Analyzing the sample under static conditions (vacuum and room temperature) does not represent real life situation for many cases. To understand the structure-property relationship of the different samples, it would be necessary to visualize (in real time) the dynamic mechanisms of the specimen as a function of different stimuli (e.g. temperature, pressure, bias, liquid, etc) that would manipulate and mimic the real life conditions to which such sample is normally exposed. In-situ TEM makes it possible.

1.1. TRANSMISSION ELECTRON MICROSCOPY IN LIQUID CELL

Development of Micro Electro Mechanical System (MEMS) has facilitated in-situ TEM. There are functionalized holders that contain MEMS chip, within which it is possible to combine different native environment (e.g. liquid , gas) surrounding the sample. MEMS gives possibility to combine different stimuli (e.g. gas heating, liquid heating, gas biasing, liquid biasing etc.). Liquid sample holder with exploded view of holder tip is shown in figure 1.2. It consists of two chips (Top chip and Bottom chip) and a O-ring, combination of these three is called nano cell. MEMS chip is located in tip area with O-ring to seal the liquid within cell. Bottom chip (figure 1.2c) has features to make flow in nano cell possible. Inlet and outlet is shown on chip. Electron transparent window is made of Si_3N_4, which allows to pass electrons. Similar type of holders are available for gas system with some modifications.
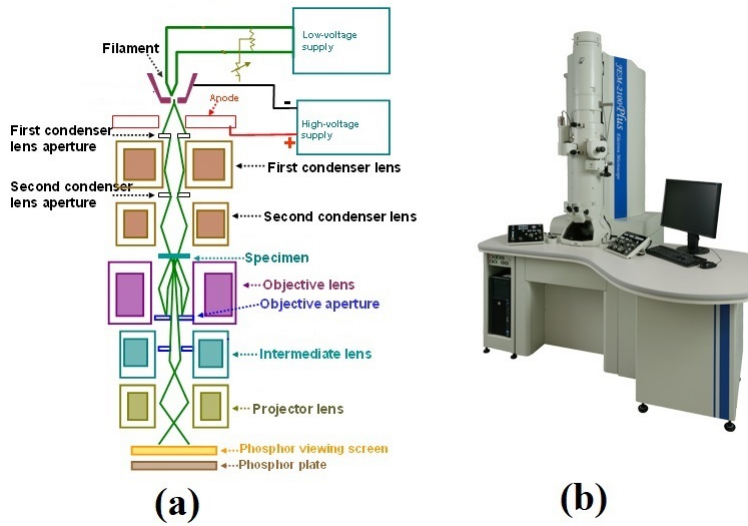
Figure 1.1: (a) Schematic diagram of TEM[1] (b) Commercial transmission electron microscope (JEM-2100Plus) [2]
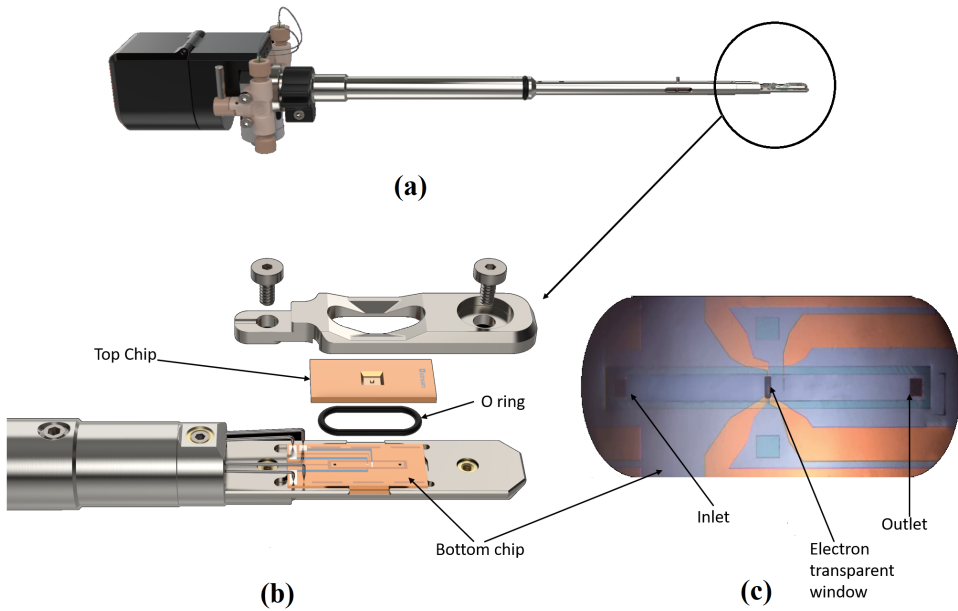

Figure 1.2: DENSsolutions Stream system (a) sample holder for liquid sample (b) sample holder tip with liquid cell and (c) MEMS chip with electrodes and inlet and outlet channel [3]

Many processes occur in moist environment, most of biological species naturally occur liquid environment. These processes can be captured using specially designed liquid cell. Mainly two types of liquid cells are used for this purpose, open cells and encapsulated cells (or monolithic cells) [4]. In open cell differential pressure is maintained in the sample by special differential pumping system, which ensures vacuum in other parts of chamber. Low vapour pressure liquids and particularly ionic liquids can be easily imaged this way. Water which has high vapour pressure can also be imaged by this method but that will require cooling stage with TEM [5]. Closed cell is under vacuum from the outside and the inside will be pressure with few bars, so it should withstand that pressure difference. Material with high Young's modulus is required to avoid bulging of cell. Silicon nitride, hexagonal boron nitride, graphene are some materials that can be used for this application. Silicon based micro-manufacturing techniques are well developed so membrane with silicon nitride is suitable for manufacturing. Graphene on the other side with single atomic thickness, has well known properties such as electron transparency, a very high young's modulus. it is a zero overlap semi-metal (with both holes and electrons as charge carriers) with very high electrical conductivity. However, the lack of compatible micro manufacturing techniques makes it difficult to fully integrate it within the manufacturing of liquid cells [6].
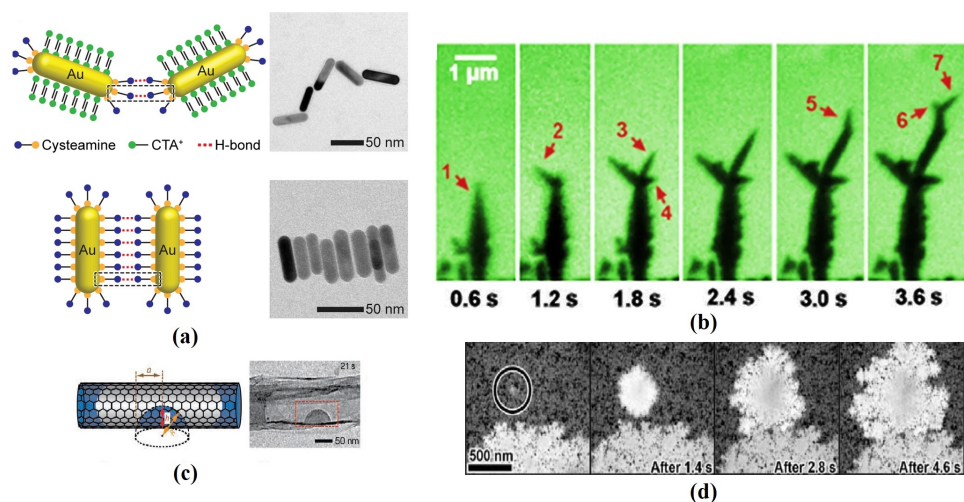
Figure 1.3: Examples of liquid sample in-situ TEM observations (a) Gold nano particles bond under different concentrations of solution [7] (b) Electrochemical deposition of Lead (Pb) (number in image shows branches of Lead (Pb) [8] (c) Nano droplet condensation inside graphane channel [9] (d) Iron (Fe) corrosion in acetic acid environment [10]

In-situ TEM for liquid samples can be used for wide area of application in physics, chemistry, biology and material science. Some examples of liquid medium in-situ TEM are mentioned here. Dynamics of nano particles generation and cluster formation can be analyzed by liquid in-situ TEM [11], like a study is done for nano gold rods bond formation under different concentration of solution (figure 1.3a), which gives better understanding of bond formation[7]. Another application is electro chemical processes,

which are important mostly for energy storage and material synthesis. Real time observation helps to reveal kinetics of electrochemical processes and composition it gets after process[12]. In-situ TEM analysis of Electro chemical deposition of lead (Pb) on gold (Au) electrode (figure 1.3b) using lead nitride solution as electrolyte reveals solution concentration significantly affects morphology of deposition [8]. Growth and uniformity of Lithium (Li) electro deposition for Li-ion batteries can be visualized under TEM and optimum current densities can be obtained [13]. TEM has already been used to see corrosion products, but in-situ TEM can make it possible to see critical changes during process [14]. Iron (Fe) thin film corrosion with acetic acid is analyzed (figure 1.3d). Dissolution of iron (Fe) grains gives insight of corrosion of different grain shape and size[10]. Liquid at nano scale behaves differently than micro scale because free energy and configuration entropy become important at nano scale. In-situ TEM can be used to visualize movement of liquid on solid substrate and solid nano particles movement in liquid [9], like nano droplet condensation inside graphane nano tube is shown in figure 1.3c.

1.2. Challenges in Liquid cell in-situ TEM

Liquid cell in-situ transmission electron microscopy allows the study of liquids or objects in liquid with atomic level resolution. There are many exciting applications in the field of corrosion, battery electrolyte, biological cell observation, etc. The main problem with these studies is the electron interaction with liquid (radiolysis), which generates species like gases, radicals, and ions. Species generated may react or change the composition of the sample. This changes the environment surrounding the observation point, so it is important to know the concentration of species generated to interpret observation from TEM correctly.

One of the chemical property that is important for liquid is pH. pH is the measurement of H^+ ions in solution. It is important to quantify pH change inside liquid nano cell while observation. Interaction of electron beam with liquid also generates heat. Heated sample can behave differently, so it is also important to quantify temperature change due to this.

To quantify these parameters main challenge is a very small confined volume (in order of nanoliter), and limited understanding of electron beam interaction with liquid at high dose rate (in order of $10^9 Gy/s$). To address these challenges this thesis focus on the measurement of pH change inside liquid nano cell and characterization of pH sensor.

References

[1] Y. Liao, "Practical electron microscopy and database." https://www.globalsino.com/EM/page4554.html, 2018.

[2] "Tem catalogue download." https://www.jeol.co.jp/en/download_catalogue.html#tem.

[3] "Stream: In situ tem liquid + biasing or heating." https://denssolutions.com/products/stream/.

[4] N. Jonge and F. Ross, "Past, present, and future electron microscopy of liquid specimens," in *Liquid Cell Electron Microscopy* (F. Ross, ed.), Advances in Microscopy and Microanalysis, ch. 1, pp. 3–25, Cambridge University Press, 2017.

[5] C. Wang, "Imaging liquid processes using open cells in the tem, sem and beyond," in *Liquid Cell Electron Microscopy* (F. Ross, ed.), Advances in Microscopy and Microanalysis, ch. 3, pp. 56–75, Cambridge University Press, 2017.

[6] E. Jensen and K. Molhave, "Encapsulated liquid cells for transmission electron microscopy," in *Liquid Cell Electron Microscopy* (F. Ross, ed.), Advances in Microscopy and Microanalysis, ch. 2, pp. 35–52, Cambridge University Press, 2017.

[7] S. F. Tan, U. Anand, and U. Mirsaidov, "Interactions and attachment pathways between functionalized gold nanorods," *ACS Nano*, vol. 11, no. 2, pp. 1633–1640, 2017.

[8] K. N. . H. Z. Minghua Sun, Hong-Gang Liao, "Structural and morphological evolution of lead dendrites during electrochemical migration," *Scientific Reports*, vol. 3, p. 3227, 2013.

[9] U. Mirsaidov and P. Matsudaira, "Nanoscale water imaged by in situ tem," in *Liquid Cell Electron Microscopy* (F. Ross, ed.), Advances in Microscopy and Microanalysis, ch. 13, pp. 276–287, Cambridge University Press, 2017.

[10] D. Gross, J. Kacher, J. Key, K. Hattar, and I. M. Robertson, "In situtem observations of corrosion in nanocrystalline fe thin films," pp. 327–338, 2018.

[11] H. Liao, K. Niu, and H. Zheng, "Nano structure growth, interactions, and assembly in the liquid phase," in *Liquid Cell Electron Microscopy* (F. Ross, ed.), Advances in Microscopy and Microanalysis, ch. 9, pp. 191–206, Cambridge University Press, 2017.

[12] F. Ross, "Quantifying electrochemical processes using liquid cell tem," in *Liquid Cell Electron Microscopy*, Advances in Microscopy and Microanalysis, ch. 10, pp. 210–233, Cambridge University Press, 2017.

[13] A. J. Leenheer, K. L. Jungjohann, K. R. Zavadil, J. P. Sullivan, and C. T. Harris, "Lithium electrodeposition dynamics in aprotic electrolyte observed in situ via transmission electron microscopy," *ACS Nano*, vol. 9, no. 4, pp. 4379–4389, 2015.

[14] S. Chee and M. Burke, "Application of liquid cell tem in corrosion science," in *Liquid Cell Electron Microscopy* (F. Ross, ed.), Advances in Microscopy and Microanalysis, ch. 12, pp. 258–272, Cambridge University Press, 2017.

2

LITERATURE AND THEORY

Discussion of electron beam interaction with water and pH sensing theory is done in this section. After extensive literature study design parameters affecting pH sensor is derived and conclusions based on that is made for selection of material and pH sensing method.

2.1. EFFECT OF ELECTRON BEAM ON LIQUID SAMPLE

To get higher resolution from TEM it is important to tackle the problem of aberration correction. Another way is to decrease the wavelength of incoming electron, therefore requiring the user to increase the accelerating voltage. Development of suitable sample preparation methods (e.g. using focused ion beam) has paved a way to make samples that are electron transparent with typical thickness < 50 nm. That has decreased requirement of high voltage for atomic level resolution. This electron beam interacts with sample during analysis [1, 2]. Electron beam damages sample in two main way, ionization damage and knock on damage. Generally speaking, increasing the electron energy results in two effects: the ionization level decreases, while the "knock-on" damage increases. Therefore, the overall electron beam effects depend on different parameters such as the beam energy, beam diameter, sample type, sample dimensions, electron current density, sample temperature and electron dose [3]. Heating, electrostatic charging, radiolysis, displacement damage, sputtering and hydrocarbon contamination are some of the effects of electron beam on sample [4]. In this thesis, where the focus will be on liquid phase experiments, the particular effects of the electron beam on sample temperature and radiolysis will be discussed. Temperature and radiolysis affects pH of sample under observation, so it is necessary to study it in detail.

2.1.1. TEMPERATURE EFFECT

Due to inelastic scattering energy is transferred from electron to atoms that ultimately rise temperature of nano cell and specimen. This nano cell, which is in vacuum, does not lose energy into surrounding by convection. If the temperature rise is small, radiation loss is also negligible. Therefore, conduction becomes the only heat loss mechanism that

plays a considerable role during the heat transfer from the nano cell to the surroundings, via the holder [3]. Depending on TEM parameters like beam size and electric current, specimen parameters like thickness, thermal diffusivity and heat capacity temperature rise can vary. Here calculations for simplified model of heat generation and diffusion is done for system shown in 1.2b. Simplified model that is used to calculate heat generation in water due to electron beam is depicted in figure 2.1, as discussed only conduction is considered for heat transfer. Top and bottom windows are 50 nm thick and with vary high thermal conductivity compared to the liquid inside the cell, so heat generation from this is neglected.
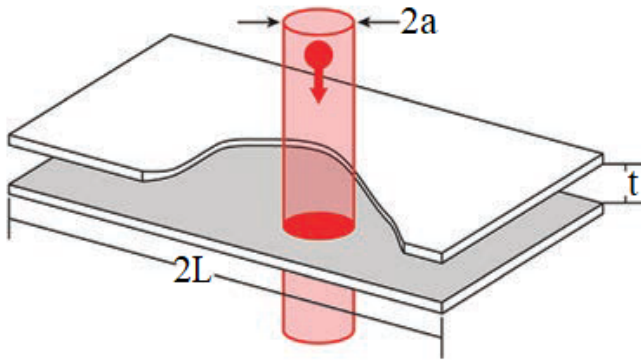
Figure 2.1: Schematic representation of cylindrical electron beam irradiating nano cell [5]

Dose rate (ψ) ($Jkg^{-1}s^{-1}$) is calculated as equation 2.1 [5]. Continuous slow down approximation (CSDA) is considered here for energy loss of e^- beam. Generally speaking, the deflection of the electron is coupled to the amount of energy they loose. For high deflections, high energy losses are expected. But CSDA represents an average of that. Here S is density normalized stopping power ($MeV cm^2 g^{-1}$), I is current (A), a is beam radius (m), t is thickness of liquid layer (m) and λ is mean free path of electrons (m) inside liquid. $\dot{q}$ is heat generated per unit volume as equation 2.2 [5]. ρ is density of medium in which electron beam travels.

$$\psi = \frac{10^5 SI}{\pi a^2} \left(1 + \frac{t}{\lambda}\right) \tag{2.1}$$

$$\dot{q} = \psi \rho \tag{2.2}$$

For maximum energy generation upper limit of TEM is considered. Energy of 300 KeV, with 10 nA current and beam radius is 1 nm. Data of stopping power is taken from NIST database [6]. Thickness of liquid layer in nano cell is 300 nm. Mean free path of electron in liquid water is 300 nm [5]. Electron beam energy loss per unit volume ($\dot{q}$) is $1.6 * 10^{18} Wm^{-3}$.

1 D steady state conduction equation is solved for cylindrical body with heat generation and maximum increase (at center of illuminated area in liquid) in temperature is calculated by equation 2.3 [5]. Here K is thermal conductivity of liquid ($Wm^{-1}K^{-1}$), L is window length (m). Maximum temperature is at center of cylinder. It is found to be 5.84 K increase for TEM condition discussed above. Which is comparable with temperature increase calculated in [5] and [4].

$$\Delta T_{max} = \frac{\dot{q}a^2}{2K}\left(\frac{1}{2} + ln(\frac{L}{a})\right) \tag{2.3}$$

For standard operating conditions temperature increase is few degrees. It can vary for different operating conditions. For example liquid nano cell under higher pressure has more liquid thickness (upto few μm), for this temperature increase can be more. Calculation here does not consider conduction between water and silicon nitride transparent window, so temperature increase by this calculation is maximum. If sample in liquid medium is poor thermal conductor, local temperature rise can be more.

Temperature change has its effect on pH of solution and electrode sensitivity. Change in pH of solution with temperature is not an error, but electrode sensitivity should be compensated to avoid error [7]. Considering maximum temperature increase of 5 K, it can be theoretically calculated that maximum error can be 0.067 pH if temperature compensation is not done. This calculation is shown in appendix A.1.

2.1.2. RADIOLYSIS

Radiolysis is the dissociation of molecules by incident radiation. When α, β, γ radiation irradiates molecules, its chemical bond (which has energy in order of 10^0 eV) disintegrates and several species (radicals, ions, molecules, atoms) are formed [8]. These species which are generated by direct effect of radiation are called primary yields. Primary yields then react with each other forming many radiolytic products [5]. Electron beam interaction with water molecule is shown in figure 2.2. Direct interaction of electron beam with water occurs within 10^{-15} second time scale, after that electron physically interacts with species formed during previous stage and species chemically reacts with each other. That is physico-chemical stage. After 10^{-12} second slow reactions starts occurring between primary yields. For water (H_2O) it forms sixteen species. If other molecules like solvent present in water, electron beam can form more species.

Some of the examples for radiolysis effect on in-situ TEM are discussed here.

P. Abellan et al. [9] observed generation of $Ce(OH)_3$ nano particles (Figure 2.3), when cerium(III) nitrate solution (pH: 5.2) is irradiated with electron beam in TEM. A Pourbaix diagram shows stability of $Ce(OH)_3$ above pH 10.4, that means pH of solution has increased due to electron beam.

S. Chee et al. [10] study corrosion of copper (Cu) in NaCl solution. Figure 2.4 shows copper (Cu) corrosion in Nacl solution, when exposed to electron beam. Radiolytic species may affect behaviour of corrosion in this case. So while interpreting the results, it is necessary to account generated species and and its concentration.
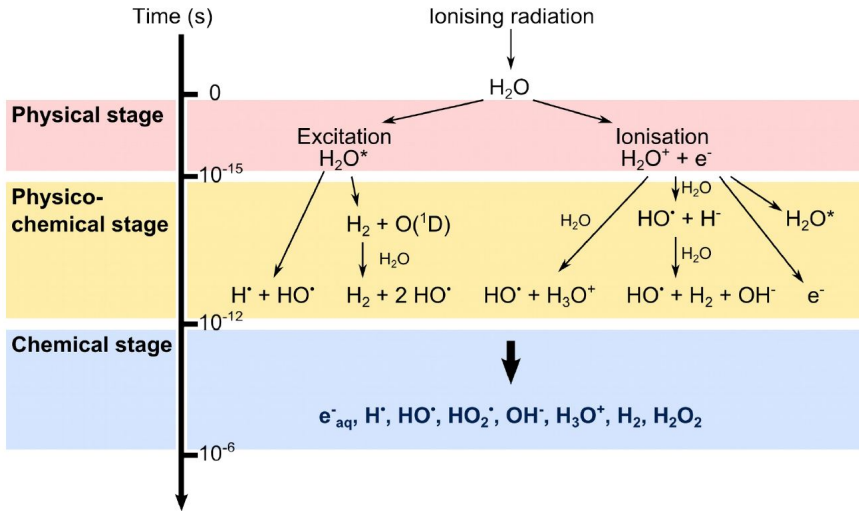
Figure 2.2: Interaction of electron beam with water molecule representing three stages of reaction [8]
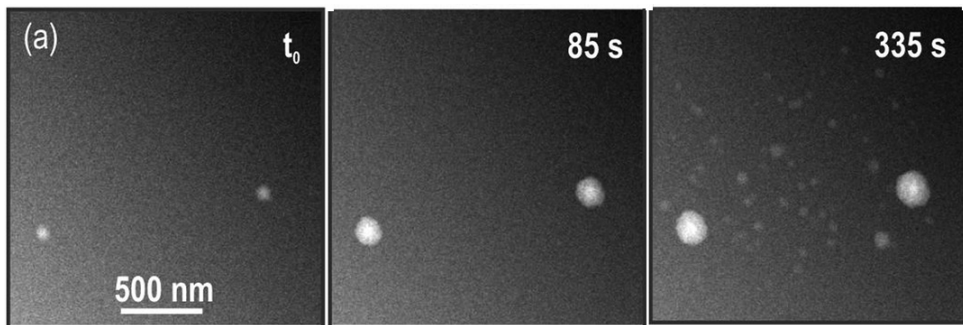
Figure 2.3: $Ce(OH)_3$ particle growth due to radiolysis effect (all figures have same scale bar (500 nm)) [9]

QUANTIFYING GENERATION OF RADIOLYSIS PRODUCTS

To quantify radiolysis several attempts has been made. Numerical and experimental studies are discussed here.

N.M. Schneider et al. [11] has numerically studied effect of electron beam on water. Radiolysis of water generates these primary products, $H_2O \rightarrow e_h^-$, H•,OH•, H_2, H_2O_2, H_3O^+,HO_2• [5]. After generation of seven primary species, sixteen species are generated due to reactions between them. This changes pH of solution. Results for generation of different species and pH change with dose rate is shown in figure 2.5. Species generation above dose rate 10^4 $\frac{Gy}{s}$ is linear. Unit Gy (Gray) is equivalent to J/kg, which means absorption of one joule of radiation energy per kilogram of matter. For dose rate more than $10^3 \frac{Gy}{s}$, pH of water decreases. This decrease in pH strongly depends on initial pH of liquid. Typical dose rate for in-situ TEM experiments ranges from $10^6 - 10^{10}$ $\frac{Gy}{s}$. This generation of species and change in pH affects the specimen to be observed
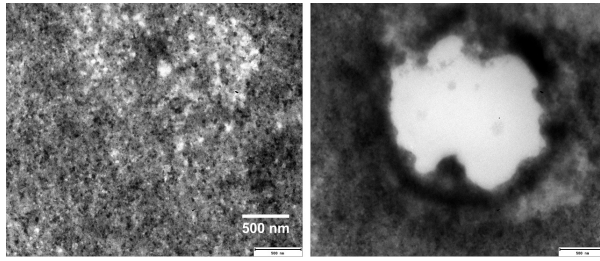
Figure 2.4: Copper (Cu) thin film corrosion in 6M NaCl solution when exposed to electron beam (all figures have same scale bar (500 nm))[10]

as discussed above. This simulation has many assumptions like, generation of species is taken from literature which has very low dose rate (3-4 order of magnitude less). It is assumed that every time electron interacts with liquid, it hits H_2O molecules. But after initial few microseconds probability of electron hitting H_2O molecule is less than 0.1 [8]. As a consequence this simulation is good for qualitative analysis but for quantitative analysis experiments should be done.

To evaluate concentration of generated species, M. Nilsen [8] tried to quantify the concentration of H_2O_2 and H_2 for in-situ SEM experiments. For water it is observed that from simulation ratio of $H_2O_2 : H_2$ is 1:1, but by experiments it is 1:2.4. For SEM entire electron beam is absorbed into liquid layer, for TEM it is not the case. It appears that radiolytic species generation in both can vary. No study for in-situ TEM/SEM which measures pH(experimentally) is done. Thus there is a need for a pH sensor for in-situ TEM measurement to understand observations by microscope.
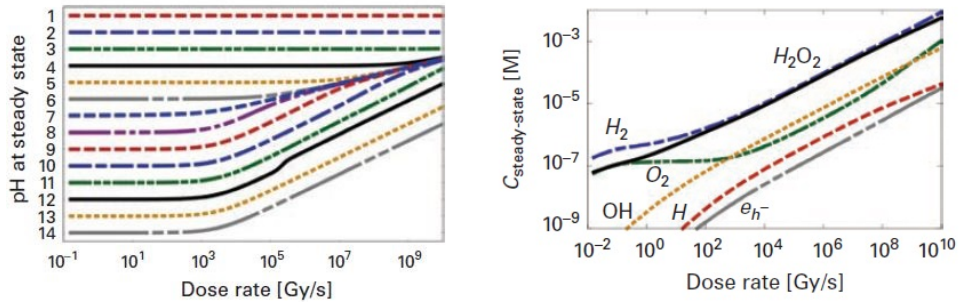
Figure 2.5: Steady state species generation and pH change for different dose rate (unit of dose rate is $\frac{Gy}{s} = \frac{J}{Kg.s}$)[11]

2.2. PH SENSING

pH is the measurement of the hydrogen ion activity in a solution, which is given as following [7]:

$$pH = -log(a^{H^+}) \tag{2.4}$$

Traditionally glass electrode is used to measure pH in solution. It measures the potential between a glass electrode with respect to some reference electrode. The potential of the reference electrode remains constant and glass electrode potential changes with pH of solution. Theoretically this potential can be represented by Nernst potential [7], which is linear with pH. Ideal slop at 25°C is -0.059 $\frac{V}{pH}$, which defines sensitivity of this sensor.

$$E = E^0 + \frac{R * T}{n * F} * ln(a^{H^+})$$ (2.5)

Here E^0: Constant, R: Gas constant, T: Temperature of solution, n: Stoichiometry for electron transfer, F: Faraday constant, a^{H^+}: Activity of Hydrogen ion in solution

Generally measurement of pH is done by open circuit potential (OCP) measurement with sensing membrane of glass. Sensing membrane is important because it makes equilibrium with hydrogen ions (H^+) in the liquid, which changes potential across membrane as function of pH. For micro scale systems different pH measurement techniques and different pH sensing membrane are explored. Those techniques and materials for membrane are discussed in following sections.

2.2.1. METHODS OF PH SENSING

Widely used glass electrode for pH measurement has limitation of miniaturization. For micro scale pH measurement many other techniques are developed based on electrical, optical, acoustic devices. H. Oh et al. [12] developed surface acoustic wave device for pH measurement. Several optical pH sensors like CCD camera pH sensor, ratiometric pH sensor, fluorometric pH sensor, Optical fiber pH sensor are described by M. Khan et al.[13] in their review of pH sensors. For current application acoustic and optical pH sensors are extremely difficult to integrate in system described in figure 1.2. Therefore detail investigation on techniques like potentiometry, chemiresistor, EIS (Electrolyte Semiconductor Insulator), ISFET (Ion Selective Field Effect Transistor) and ExGFET (Extended Gate Field Effect Transistor) is done from now on. Data for performance of pH sensor is presented in table in appendix A.2, section 2.2.1 is summery from that study.

DETECTION TECHNIQUES

1. Potentiometric (OCP: Open circuit potential)

   Potentiometric methods are most commonly used pH measurement techniques. Schematic of this is shown in figure 2.6a. It consists of two electrodes, one sensing electrode with ion selective membrane and other reference electrode with constant potential. The potential between two electrodes is measured with high impedance voltmeter.

   Ideal sensitivity of this sensor is defined by Nernst potential discussed in previous section, which is -59.16 $\frac{mV}{pH}$ at 25°C. pH measured with this method shows sub, super and ideal Nearnstian slope [14, 15]. B. Lakard et al.[16] study polymers as pH sensitive membrane. Open circuit potential response for that (figure 2.6b) shows different slope for different polymers.
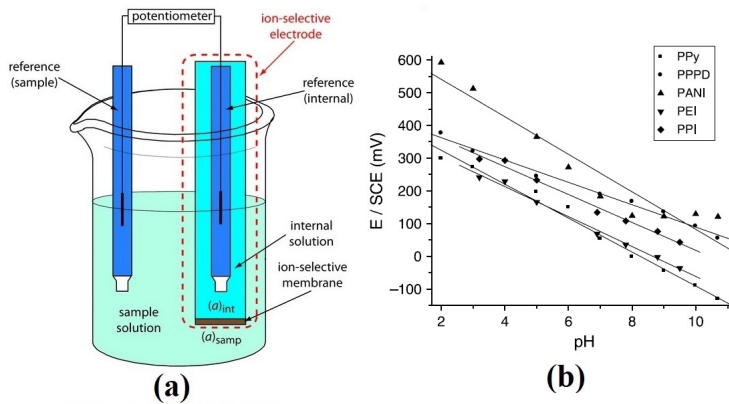
Figure 2.6: Schematic representation of pH measuring techniques (a) potentiometry [17] (b) response for potentiometry [16]

2. Chemi resistor

   A reference electrode free pH sensing technique, in which sensing material conductivity changes with pH of solution [18]. Schematic of this is shown in figure 2.7a, which has interdigitated electrode covered with sensing material.

   There are several studies available for these sensors [19–23]. The detail of that is presented in appendix table A.2. It is observed from literature that response of conductivity/impedance with pH is non linear. That makes sensor out of use unless it is calibrated at each and every pH point. B.S. Kang et al.[24] study single ZnO nano rod conductivity with pH, which showed linear response. Typical response of sensor can be seen in figure 2.7b.

3. EIS (Electrolyte semiconductor insulator)

   This type of pH sensor detects change in capacitance of its gate due to change in pH of solution. Figure 2.7f shows schematic of such a device. Response of this type of device is shown in figure 2.7g and 2.7h. M. Chen et al. [25] made EIS pH sensor which shows good linearity over period of one year.

4. ISFET (Ion Selective Field Effect Transistor)

   Bergveld [26] first used ISFET for ion measurement for biological environment. This device (figure 2.7c) is similar to MOSFET, but gate is comprised of electrolyte and reference electrode. Miniaturization and compatibility with CMOS processes for manufacturing makes this method special for micro size application. Other advantage of this device is that it offers a quick response time(less than 1 second)[27, 28]. Typical response of ISFET pH sensor is shown in figure 2.7e.

5. ExGFET (Extended gate field effect transistor)

   This sensor is extension of MOSFET. Standard MOSFET gate is extended and sensing material is attached to it. Schematic of this is shown in figure 2.7d. Response of ExGFET is similar to ISFET response.
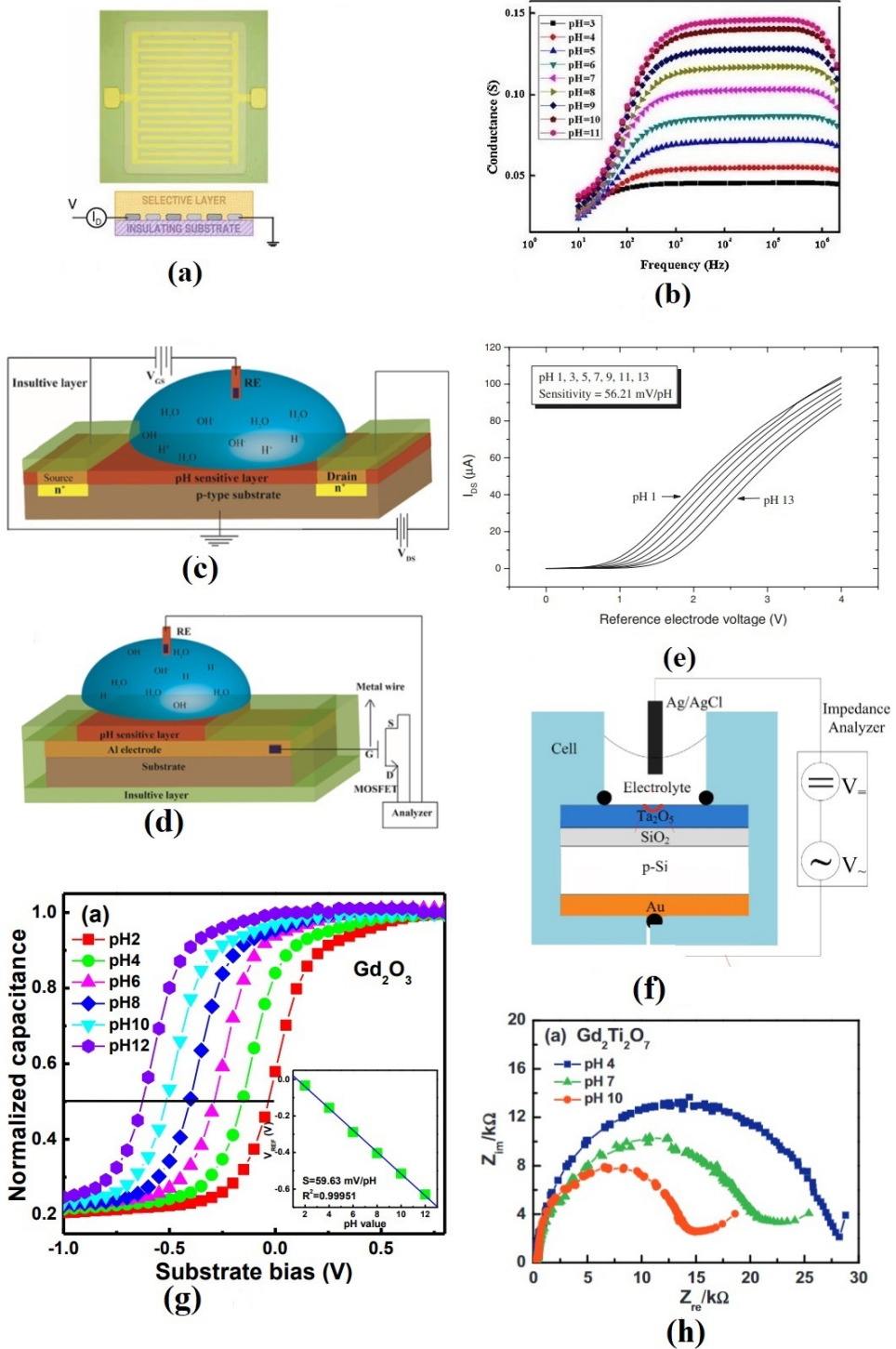
Figure 2.7: Schematic representation of pH measuring techniques and response of sensor (a) chemi resistor [18] (b) response for chemi resistor [20] (c) ISFET [29] (d) ExGFET [29] (e) response for FET devices [30] (f) EIS (impedance and capacitive) [25] (g) capacitive response [31] (h) impedance response [32]

COMPARISON OF PH SENSING METHODS

Performance and manufacturability of different methods are compared (figure 2.8) based on noise, response time, linearity, miniaturization, ease of fabrication and cost. Even though potentiometry technique is widely used, for micro application it has limitation in terms of signal to noise ratio. ISFET shows promising results for micro pH sensing, but it suffers with problem of drift and insulation of FET from solution [33]. ExGFET devices has less noise than potentiometric sensors and does not suffer of insulation problems from solution but they still suffer from drift problem [34]. Considering all of this points, it can be concluded that ISFET, ExGFET and potentiometry sensors can be used for current application of pH measurement for in-situ TEM.
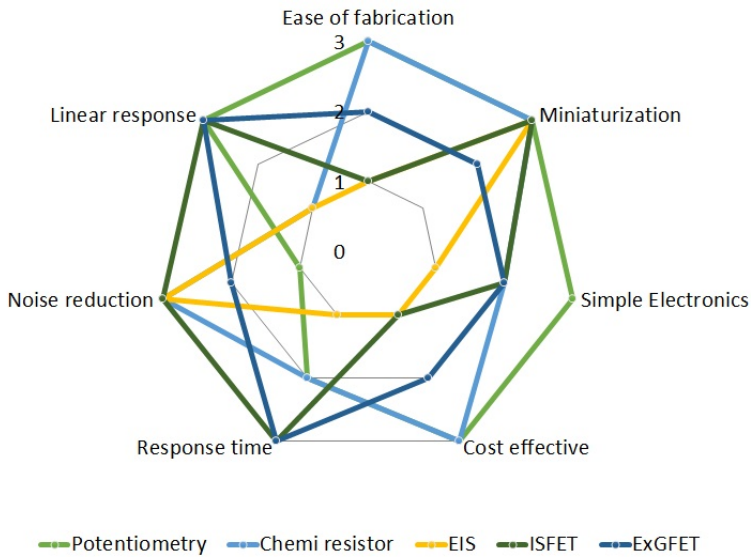
Figure 2.8: Comparison of pH sensing methods

2.2.2. PH SENSING MEMBRANE

With development of new pH sensing techniques, new materials are analysed for this application. As micro fabrication techniques are developing, many materials like metal oxide, polymers and nitride had found their way into micro pH sensing. S. Glab et all.[35] has given ideal properties for metal oxide electrode for pH sensing surface. It explains that metal oxide should be stable and in a reproducible state. Reproducible state means that during equilibrium reaction, metal oxide should be able to reach its previous oxidation states. It should be sparingly soluble and must participate in equilibrium reaction with hydrogen ion (equation 2.6). Hardly any material meet these ideal criteria and that leads to non standard properties of pH sensor like drift, hysteresis, sub or super nernstian response. Buck et al.[14] have described five possible mechanisms of metal oxide pH sensing. Among them single phase oxygen intercalation is the most possible explanation for metal oxide pH sensing [14, 29]. In this hydrogen ion forms equilibrium with metal oxide and changes its oxidation state. For this, equilibrium and electrode potential

are given as follow [14].

$$equilibrium : MO_x + 2\delta H^+ + 2\delta e^- \rightleftharpoons MO_{x-\delta} + \delta H_2O \qquad (2.6)$$
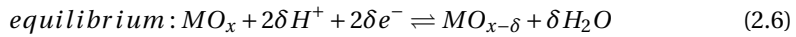
$$electrode\,potential : \phi = C + \frac{R*T}{F}ln(a^{H^+}) + \frac{R*T}{2*F}ln(a^O) \qquad (2.7)$$

Where, ϕ: electrode potential, C: constant, a^O: Activity of oxygen in solid phase

Potential of metal oxide varies with hydrogen ion (H^+) and oxygen in solid phase (equation 2.7). To measure pH, sensing membrane should be manufactured in such a way that oxygen in solid phase remains constant.

pH sensing characteristics gets affected by material of sensing membrane, technique used for manufacturing and geometry of membrane. To investigate the effect of each of the parameter this section is divided into three sub sections.

- Material for sensing membrane

- Manufacturing technique for sensing membrane

- Geometry of sensing membrane

MATERIALS FOR SENSING MEMBRANE

To understand behaviour of different materials in pH sensing, a review of many publication is done. All reviewed papers details are given in table in appendix A.2. Interpretation of material characteristics based on that is given in this section. Materials are categorised based on following characteristics:

- Species interference

- Range and sensitivity of material

- Drift and hysteresis of material.

Among them selectivity and drift properties are most important for pH sensor.

A list of material that are included in this study is presented in table 2.1. Some of materials like Pt, SiO_2 fail to obtain stable pH response so they are not considered for further study [27, 36, 37]. Some of materials like OsO_2, Diamond, AlN are analysed by fewer people, so further investigation on their behaviour is required to establish them as reliable pH sensing material.

OsO_2	Sb/Sb_2O_3	Pt	TiN	Gd_2O_3	$Polybisphenol$
IrO_2	Ir/IrO_2	ZnO	InN	AlN	$polyethyleneimine(PEI)$
RuO_2	Pd/PdO	ITO	NiO	CuO	$polypropyleneimine(PPI)$
RhO_2	PtO_2	Si_3N_4	Zr/ZrO_2	Co_3O_4	$polypyrrole(Ppy)$
Ta_2O_5	TiO_2	SiO_2	ZrO_2	WO_3	$poly(p-phenylenediamine)$
SnO_2	PdO	Al_2O_3	$Ta_2O_5 : RuO_2$	$Diamond$	$polyaniline(PANI)$

Table 2.1: List of materials included in this literature (appendix A.2)

2

Species interference Ideally sensing membrane should not be sensitive to species other than hydrogen ion (H^+) for pH sensing. Other species affecting the membrane is called interfering species. Practically the membrane always have some amount of interference from other species. This is most important parameter in selection of sensing material. Traditional glass electrode is highly effective against oxidation/reduction species and highly acidic/basic solution [38], but it gets affected by hydrogen fluoride [35]. Metal oxide and nitride are relatively new sensing material. Interferences of these materials from different species are not available in form of systematic study. R.P. Buck et al. [14] studied many metal oxide interference with variety of species which is main source of information in this section. It is clear from available studies that different materials have varying degrees of selectivity towards species like anion, H_2O_2 and redox solutions. From figure 2.2 it is clear that all oxides are unstable in presence of oxidizing/reducing species like ferrocyanide and farrocaynide. Moreover, redox species highly affects all materials except IrO_2. Figure 2.2 shows different groups of materials based on interference from species, IrO_2 is least affected by other species. Various literature also confirms that IrO_2 is best suitable material for pH sensing in terms of least affected by other species [29, 39]. Figure 2.10 represents effect of anions, cations, H_2O_2 and redox interference graphically.

Material	Anion	Cation	Oxidizing/ reducing agents	H_2O_2	Redox Interferance	Other	Score
OsO_2	Non Affecting: Br^-, I^-, Cl^-, F^-	Non Affecting: Li^+, Na^+, K^+	High	Low	±200 mV	Not stable in strong alkaline	11
IrO_2	Affecting: Br^-, I^-, Cl^- Non Affecting: F^-	Non Affecting: (Li^+, Na^+, K^+): selectivity -12.4	High	Low	±20 mV	Non Affecting: O_2<0.9 mV	11
RuO_2	Affecting: I^-, Sulphate Non Affecting: Cl^-, F^-, Br^-	NonAffecting: (Li^+, Na^+, K^+)<15 mV	High	Medium	±100 mV	Affecting:O_2	13
RhO_2	Affecting:Br^-,I^- Non Affecting: Cl^-, F^-	Non Affecting: Li^+, Na^+, K^+	High	Low	±400 mV	NA	13
Ta_2O_5	Affecting:F^-,I^- Non Affecting: Cl^-, Br^-	Non Affecting: (Cu^{+2}, Fe^{+2})<13 mV, Li^+, Na^+<1mV, K^+<1mV	High	Low	±70 mV	Stable with HCl, HNO_3, H_2SO_4	11
SnO_2	NA	Non Affecting: Li^+, Na^+, K^+	High	High	NA	NA	-
PtO_2	Affecting:I^- Non Affecting:Cl^-, Br^-, F^-	Non Affecting: Li^+, Na^+, K^+	High	High	±100 mV	Affecting: NH_4Cl, O_2	13
TiO_2	Affecting:I^-,Sulphate Non Affecting: Cl^-, Br^-, F^-	Affecting:(Na^+, K^+) selectivity -10 Non Affecting: Li^+	High	High	±100 mV	Affecting:O_2	15
ZnO	NA	Non Affecting: Na^+, K^+	NA	NA	NA	NA	-
Si_3N_4	NA	Affecting: Na^+<50 mV, K^+<25 mV	NA	NA	NA	NA	-

NA:	Not Available
3	Highly affecting
2	Medium affecting
1	Low affecting

Figure 2.9: Interference of different species on sensing material (data for this table are collected from table in appendix A.2

Least affected	Medium affected	Most affected
IrO_2	RuO_2	TiO_2
Ta_2O_5	RhO_2	
OsO_2	PtO_2	

Table 2.2: Priority of material based on Interference
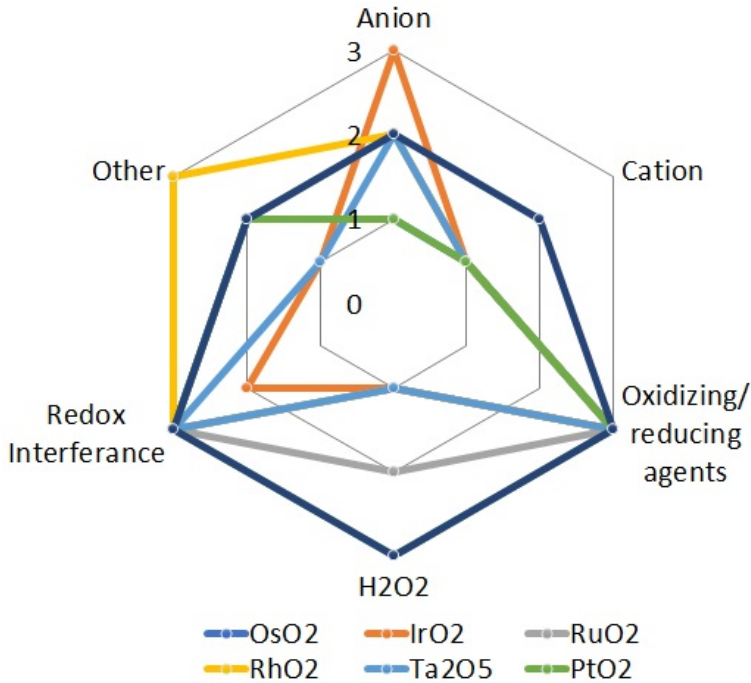
Figure 2.10: Interference of species on different material

Range and Sensitivity Range of a sensor is defined as maximum and minimum value of parameter that can be measured. For the current application range is not very much of a problem. If given sensor can detect pH within a range of 3-10, it can be used as pH sensor for in-situ TEM. From appendix A.2 it can be said that most of materials have a pH sensing range higher than this. There are few exceptions like SnO_2 and PtO_2. Some literature [14, 33] mentioned SnO_2, which does not produce any reproducible results for any pH range, but after heat and chemical treatment it shows pH range between 4-10. It is worth to mention that sputtered PtO_2 has a range of 5-10 [14, 40, 41]. But nano-porous PtO_2 has range of 2-12[40]. Maximum range(-1 to 15) is observed for polybisphenol coating on ITO [42].

Figure 2.11 represents the sensitivity of different sensing material. It can be seen that IrO_2, TiO_2 behaves near to ideal sensitivity. Material like PtO_2, Ta_2O_5, ZnO show sub-nernstian behaviours. Reasons for different behaviours of various material is unknown.

Drift and Hysteresis Drift is the continuous deviation of output of a sensor under constant input parameters and conditions. All pH sensors discussed in this review show some amount of drift. Reasons for drift are presented here.

- According to equation 2.6, presence of oxygen in solution may affect activity of oxygen in solid state (a^O) and cause drift [43].
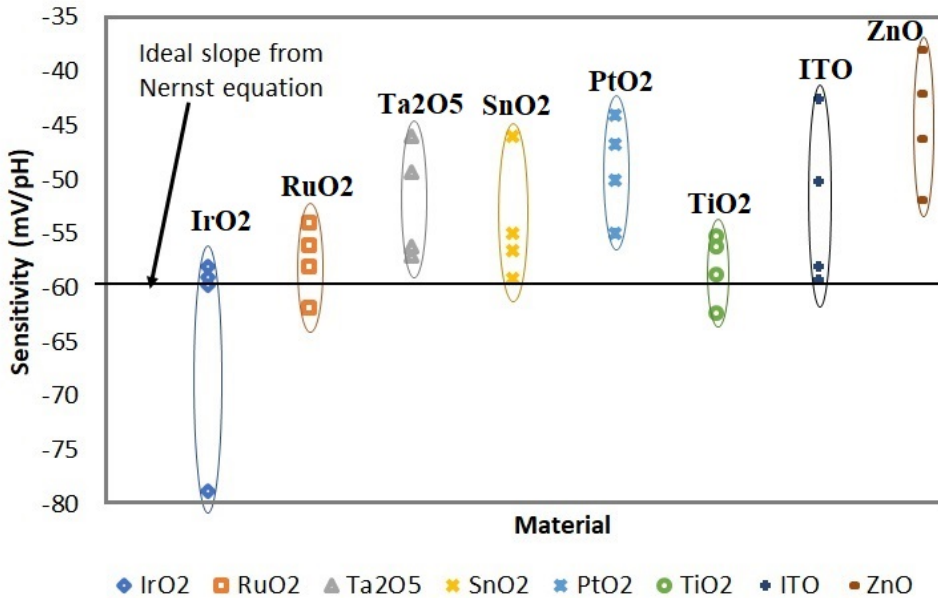
Figure 2.11: Sensitivity of different material (Nernst slope from equation 2.5) (data for this graph are collected from table in appendix A.2)

- Diffusion of ions from the measured solution to the reference electrode standard solution makes sensors drift [44].

- Asymmetry in membrane placed due to one side contact [18]

- If the time to reach equilibrium is longer than the sensor drift for that time [14]

Glass electrodes or other traditional ion selective electrodes have big advantage in terms of symmetry in both sides of their membranes. On the contrary solid state ion selective membranes have one contact with liquid and other contact with electrode. This asymmetry leads to drift of in latter membrane [18].

From reasons discussed above it can be concluded that drift can arise from many sources. To control the drift to the minimum, design (resistance and thickness of membrane) and manufacturing parameters need to be optimized. Some attempts were made to minimize drift. J. Hendrikse et al. [43] used ISFET device properties to reduce drift. They took the difference between device threshold voltage and gate voltage. Since both are drifting, their difference show stable response and small drift of $0.68 \frac{mV}{hr}$ is observed. G. Zevenbergen et al. [44] have developed a pH sensor with drift as low as $0.004 \frac{mV}{hr}$. They used modification in manufacturing (conditioned sputtered IrO_2 in H_2SO_4) and geometry (connection between sensing and reference electrode, reservoir size of reference electrode) to minimize the drift.

Hysteresis represents non ideal changes of the sensor output due to cyclic changes in input. P. Buck et al. [14] had tested many materials for hysteresis (pH: 2-12-2). Table

2.3 shows error due to hysteresis.

Material	TiO_2	RuO_2	RhO_2	SnO_2	Ta_2O_5	OsO_2	IrO_2	PtO_2
± mV	30	9	20	75	50	25	25	100

Table 2.3: Hysteresis of different material (pH: 2-12-2) [14]

Conclusion for material selection   Out of many materials discussed here, IrO_2 is found as the best suitable for species interference performance. Ta_2O_5 is a non conducting oxide, so it is resistant to species interference. However due to high impedance it has limitation for use in potentiometry. OsO_2 has good selectivity, but it is expensive and does not have extensive literature study available. In terms of range, most of the materials behave well. For sensitivity also IrO_2 performs well. TiO_2 also has good sensitivity, but it lags in selectivity. Polymer Polybisphenol shows good sensitivity and range. It is also resistive to the influence of anions and cations, but its response with redox species and H_2O_2 is unknown. So based on given parameters discussed, IrO_2 is best suitable for pH sensing. However in presence of dissolved oxygen, it generates slow drift due to slow diffusion of oxygen in membrane of IrO_2. Materials like Ta_2O_5 and ZrO_2 (electrically non conducting), do not allow oxygen to bond with sensing membranes. Hence they do not get affected by dissolved oxygen.

Several attempts are made to improve these properties by combining two or more types of materials. A film of Ta_2O_5 over IrO_2 makes the sensor more stable in environment with dissolved oxygen [38]. Ta_2O_5 and RuO_2 mixture gives a stable response and reduces drift and hysteresis compared to pure material [45]. Instead of using single materials, combinations of different materials may be useful. Generally electrically conducting materials that give good response to pH change are not good performing in selectivity (species interference). Materials that have good selectivity does not have good response, especially for potentiometric measurement due to high impedance. Although IrO_2 is kind of exception, in selectivity and response.

MANUFACTURING TECHNIQUE FOR SENSING MEMBRANE
Manufacturing of micro sensing membranes is done by several techniques. Based on which technique is used for manufacturing, it affects the performance of the sensor. Sensitivity obtained by different manufacturing processes is shown in figure 2.12. With vapor deposition techniques, sensitivity is near to ideal. For sputtered material, sensitivity varies from super to sub Nernstian. Thus post treatment is important in this method to get ideal sensitivity.
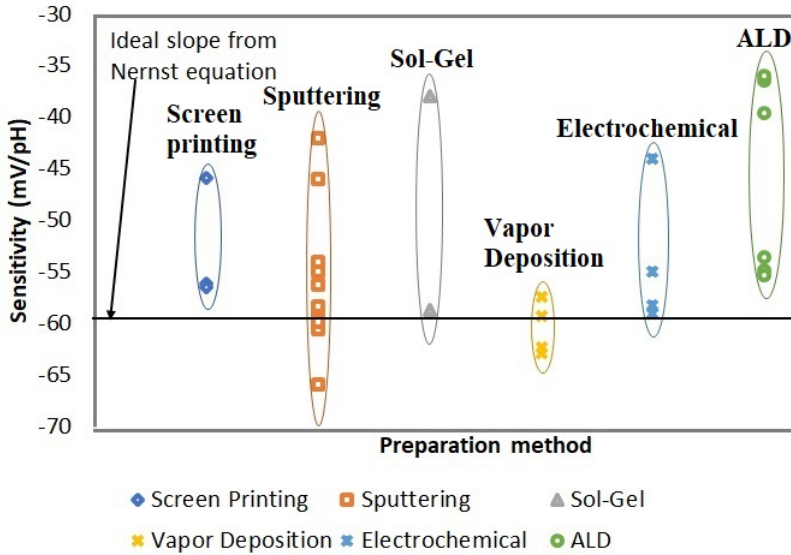
Figure 2.12: Sensitivity of different methods (data for this graph are collected from table in appendix A.2)

GEOMETRY OF SENSING MEMBRANE
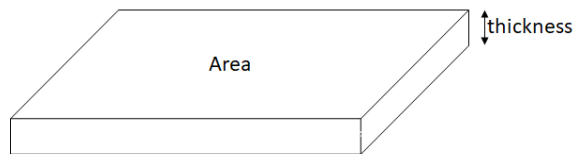
Figure 2.13: Sensing membrane geometry

Geometry of sensing membranes relies on two parameters, sensing area and thickness. Their effect on sensitivity and drift effect will be analyzed.

L. Yin et al. [33] report logarithmic decrease in sensitivity as area of sensing membrane decrease for ExGFET device. For SnO_2 over ITO if area decreases below 0.8 mm^2 the sensitivity decreases. For pH sensors described in appendix A.2, no ExGFET device can be found with an area less than 0.8mm^2. Thus ExGFET devices are not suitable for in-situ TEM application. Nernst equation does not have any area limit on sensing membrane, so with OCP it should be fine to have sensing membranes of the order of μm^2 magnitude. Figure 2.14 shows area effect on sensitivity of pH meter manufactured with sputtering for OCP and ISFET measurement. It seems that OCP and ISFET do not get affected by area of pH sensor. The smallest area reported is 0.0019 mm^2, for which sensitivity is -55 $\frac{mV}{pH}$. This area is still big for current application. Y. Zhang et al. [?] have made nano size pH probe with diameters of 2.5 μm, 1 μm and 100 nm diameter. It shows changes in pH potential with small sensitivity (-17.5 $\frac{mV}{pH}$). However they used a certain protein as sensing materials, that can also be the reason for reduced sensitivity. It is clear

from their results that smaller probes make smaller currents to flow, that are difficult to measure without noise.

Effect of thickness on drift is shown in figure 2.15. It can be said that for very low thicknesses of sensing membrane (<10 nm) the drift is very large. For thicknesses varying between 11 to 100 nm, drift of majority of sensors is less than 1 $\frac{mV}{hr}$. As the thickness increases, the drift moves towards higher values. Reason for this is large time to form equilibrium between sensing membrane and solution. For thickness < 10 nm drift is very high, reason for this is unknown.
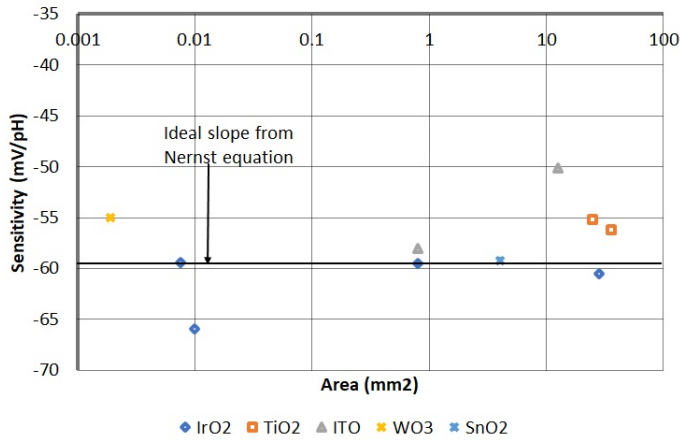
Figure 2.14: Area vs. Sensitivity (data for this graph is collected from table in appendix A.2)
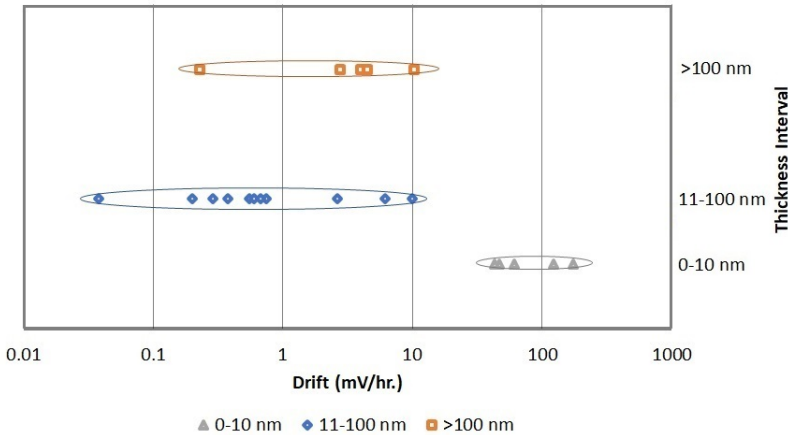
Figure 2.15: Drift for different thicknesses of sensing material (data for this graph is collected from table in appendix A.2)

SIMPLIFIED EQUIVALENT ELECTRIC CIRCUIT: POTENTIOMETRIC SENSOR

A simplified electric circuit is shown in figure 2.16. Here R1 is solution resistance, R2 is charge transfer resistance and C1 is double layer capacitance. As area of pH sensor increases R2 decreases, which leads to smaller drift of pH sensor [18].
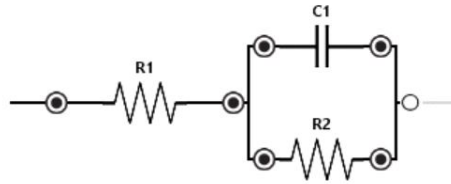
Figure 2.16: Simplified equivalent electric circuit

2.3. CONCLUSION AND LEARNING FROM LITERATURE REVIEW

- Species interference is very important in selection of membrane, specially when due to electron beam many species are created. IrO_2 has been identified as least affected by other species.

- Most of pH sensing materials studied have range more than pH 3 to 10, so range is not an criteria for selection of material.

- Sensitivity of membrane varies with manufacturing technique used and processing of membrane before using as pH sensor.

- Drift can be seen in sensor due to very high charge transfer resistance between ions and membrane. Hydration of pH sensing layer takes time, which can also induce drift. To reduce drift area of pH sensor should be sufficiently large (which reduces charge transfer resistance) and membrane can be hydrated before use.

- Nernst equation does not depends on area, so pH sensor sensitivity is independent of area. So theoretically there is no restriction of pH sensor area.

- Temperature increase due to electron beam is very limited, so there is no need to compensate pH for same.

- Thickness of sensing membrane should be >80 nm, according to hydrated layer theory to get fully Nernst response from pH sensor [18].

2.3.1. RESEARCH QUESTION AND CHALLENGES

How does pH changes temporally and spatially, during radiolysis in the TEM liquid chamber.

- Remove the effect of species other than H^+ to sensing membrane: As discussed in the radiolysis, it generates many species that may react with pH sensor. To measure pH accurately effect of other species should be quantified or eliminated.

- Integration of reference electrode into the system: TEM liquid cell is small enclosure with limited space, which makes integration of reference electrode into TEM liquid cell challenging.

REFERENCES

[1] H. Ichinose, H. Sawada, E. Takuma, and M. Osaki, "Atomic resolution HVEM and environmental noise," *Microscopy*, vol. 48, pp. 887–891, 01 1999.

[2] R. Egerton, "Choice of operating voltage for a transmission electron microscope," *Ultramicroscopy*, vol. 145, pp. 85 – 93, 2014. Low-Voltage Electron Microscopy.

[3] M. L. Taheri, E. A. Stach, I. Arslan, P. Crozier, B. C. Kabius, T. LaGrange, A. M. Minor, S. Takeda, M. Tanase, J. B. Wagner, and R. Sharma, "Current status and future directions for in situ transmission electron microscopy," *Ultramicroscopy*, vol. 170, p. 86—95, November 2016.

[4] R. Egerton, P. Li, and M. Malac, "Radiation damage in the tem and sem," *Micron*, vol. 35, no. 6, pp. 399 – 409, 2004. International Wuhan Symposium on Advanced Electron Microscopy.

[5] N. M. Schneider, "Electron beam effects in liquid cell tem and stem," in *Liquid Cell Electron Microscopy* (F. Ross, ed.), Advances in Microscopy and Microanalysis, ch. 7, pp. 140–163, Cambridge University Press, 2017.

[6] M. Berger, J. Coursey, M. Zucker, and J. Chang, "Nist stopping-power range tables for electrons, protons, and helium ions." https://www.nist.gov/pml/stopping-power-range-tables-electrons-protons-and-helium-ions, 1998.

[7] R. Webber, "More about meaning of ph," in *The book of pH*, ch. F, pp. 83–93, 1957.

[8] Møller-Nilsen, *In-situ SEM electrochemistry and radiolysis*. PhD thesis, DTU nanotech, 2016.

[9] P. Abellan, T. H. Moser, I. T. Lucas, J. Grate, J. E. Evans, and N. D. Browning, "The formation of cerium(iii) hydroxide nanoparticles by a radiation mediated increase in local ph," *RSC Adv.*, vol. 7, pp. 3831–3837, 2017.

[10] S. W. Chee, S. H. Pratt, K. Hattar, D. Duquette, F. M. Ross, and R. Hull, "Studying localized corrosion using liquid cell transmission electron microscopy," *Chem. Commun.*, vol. 51, pp. 168–171, 2015.

[11] N. M. Schneider, M. M. Norton, B. J. Mendel, J. M. Grogan, F. M. Ross, and H. H. Bau, "Electron–water interactions and implications for liquid cell electron microscopy," *The Journal of Physical Chemistry C*, vol. 118, no. 38, pp. 22373–22382, 2014.

[12] H. Oh, K. J. Lee, J. Baek, S. S. Yang, and K. Lee, "Development of a high sensitive ph sensor based on shear horizontal surface acoustic wave with zno nanoparticles," *Microelectronic Engineering*, vol. 111, pp. 154 – 159, 2013.

[13] M. Khan, K. Mukherjee, R. Shoukat, and D. Huang, "A review on ph sensitive materials for sensors and detection methods," *Microsystem Technologies*, 07 2017.

[14] A. Fog and R. P. Buck, "Electronic semiconducting oxides as ph sensors," *Sensors and Actuators*, vol. 5, no. 2, pp. 137 – 146, 1984.

[15] C.-W. Pan, J.-C. Chou, T.-P. Sun, and S.-K. Hsiung, "Development of the tin oxide ph electrode by the sputtering method," *Sensors and Actuators B: Chemical*, vol. 108, no. 1, pp. 863 – 869, 2005. Proceedings of the Tenth International Meeting on Chemical Sensors.

[16] B. Lakard, G. Herlem, S. Lakard, R. Guyetant, and B. Fahys, "Potentiometric ph sensors based on electrodeposited polymers," *Polymer*, vol. 46, no. 26, pp. 12233 – 12239, 2005.

[17] "Overview of electrochemistry." https://chem.libretexts.org/Courses/Northeastern_University/11%3A_Electrochemical_Methods/11.2%3A_Potentiometric_Methods, 2019.

[18] J. Janata, "Conductometric sensors," in *Principle of chemical sensors*, ch. 8, pp. 241–245 150–153, Springer, 2019.

[19] M. Simić, L. Manjakkal, K. Zaraska, G. M. Stojanović, and R. Dahiya, "Tio2-based thick film ph sensor," *IEEE Sensors Journal*, vol. 17, pp. 248–255, Jan 2017.

[20] L. Manjakkal, E. Djurdjic, K. Cvejin, J. Kulawik, K. Zaraska, and D. Szwagierczak, "Electrochemical impedance spectroscopic analysis of ruo2 based thick film ph sensors," *Electrochimica Acta*, vol. 168, pp. 246 – 255, 2015.

[21] L. Manjakkal, K. Cvejin, B. Bajac, J. Kulawik, K. Zaraska, and D. Szwagierczak, "Microstructural, impedance spectroscopic and potentiometric analysis of ta2o5 electrochemical thick film ph sensors," *Electroanalysis*, vol. 27, no. 3, pp. 770–781, 2015.

[22] K. Arshak, E. Gill, A. Arshak, and O. Korostynska, "Investigation of tin oxides as sensing layers in conductimetric interdigitated ph sensors," *Sensors and Actuators B: Chemical*, vol. 127, no. 1, pp. 42 – 53, 2007. Special Issue: Eurosensors XX The 20th European Conference on Solid-State Transducers.

[23] Y. Chen, S. C. Mun, and J. Kim, "A wide range conductometric ph sensor made with titanium dioxide/multiwall carbon nanotube/cellulose hybrid nanocomposite," *IEEE Sensors Journal*, vol. 13, pp. 4157–4162, Nov 2013.

[24] B. S. Kang, F. Ren, Y. W. Heo, L. C. Tien, D. P. Norton, and S. J. Pearton, "ph measurements with single zno nanorods integrated with a microchannel," *Applied Physics Letters*, vol. 86, no. 11, p. 112105, 2005.

[25] M. Chen, Y. Jin, X. Qu, Q. Jin, and J. Zhao, "Electrochemical impedance spectroscopy study of ta2o5 based eios ph sensors in acid environment," *Sensors and Actuators B: Chemical*, vol. 192, pp. 399 – 405, 2014.

[26] P. Bergveld, "Development of an ion-sensitive solid-state device for neurophysiological measurements," *IEEE Transactions on Biomedical Engineering*, vol. BME-17, pp. 70–71, Jan 1970.

[27] T. Matsuo and M. Esashi, "Methods of isfet fabrication," *Sensors and Actuators*, vol. 1, pp. 77 – 96, 1981.

[28] H.-K. Liao, J.-C. Chou, W.-Y. Chung, T.-P. Sun, and S.-K. Hsiung, "Study of amorphous tin oxide thin films for isfet applications," *Sensors and Actuators B: Chemical*, vol. 50, no. 2, pp. 104 – 109, 1998.

[29] L. Manjakkal, D. Szwagierczak, and R. Dahiya, "Metal oxides based electrochemical ph sensors: Current progress and future perspectives," *Progress in Materials Science*, p. 100635, 2019.

[30] J. C. Chou and L. P. Liao, "Study of TiO2thin films for ion sensitive field effect transistor application with RF sputtering deposition," *Japanese Journal of Applied Physics*, vol. 43, pp. 61–65, jan 2004.

[31] J. Her, M.-H. Wu, Y.-B. Peng, T.-M. Pan, W.-H. Weng, S.-T. Pang, and L. Chi, "High performance gdtixoy electrolyte-insulator-semiconductor ph sensor and biosensor," *International Journal of Electrochemical Science*, vol. 8, pp. 606–620, 01 2013.

[32] T.-M. Pan, P.-Y. Liao, K.-Y. Chang, and L. Chi, "Structural and sensing characteristics of gd2ti2o7, er2tio5 and lu2ti2o7 sensing membrane electrolyte–insulator–semiconductor for bio-sensing applications," *Electrochimica Acta*, vol. 89, pp. 798 – 806, 2013.

[33] L.-T. Yin, J.-C. Chou, W.-Y. Chung, T.-P. Sun, and S.-K. Hsiung, "Separate structure extended gate h+-ion sensitive field effect transistor on a glass substrate," *Sensors and Actuators B: Chemical*, vol. 71, no. 1, pp. 106 – 111, 2000.

[34] J. Chou and C. Chen, "Fabrication and application of ruthenium-doped titanium dioxide films as electrode material for ion-sensitive extended-gate fets," *IEEE Sensors Journal*, vol. 9, pp. 277–284, March 2009.

[35] S. Głab, A. Hulanicki, G. Edwall, and F. Ingman, "Metal-metal oxide and metal oxide electrodes as ph sensors," *Critical Reviews in Analytical Chemistry*, vol. 21, no. 1, pp. 29–47, 1989.

[36] W.-C. Lin, K. Brondum, C. W. Monroe, and M. A. Burns, "Multifunctional water sensors for ph, orp, and conductivity using only microfabricated platinum electrodes," *Sensors*, vol. 17, no. 7, 2017.

[37] N. J. Finnerty and F. B. Bolger, "A platinum oxide-based microvoltammetric ph electrode suitable for physiological investigations," *Analyst*, vol. 143, pp. 3124–3133, 2018.

[38] I. Lauks, "5009766 united states patent." http://www.everypatent.com/comp/pat5009766.html, 1991.

[39] D. O'Hare, K. H. Parker, and C. P. Winlove, "Metal–metal oxide ph sensors for physiological application," *Medical Engineering Physics*, vol. 28, no. 10, pp. 982 – 988, 2006. Developments in Biosensors: New Structural Designs for Functional Interfaces.

[40] S. Park, H. Boo, Y. Kim, J.-H. Han, H. C. Kim, and T. D. Chung, "ph-sensitive solid-state electrode based on electrodeposited nanoporous platinum," *Analytical Chemistry*, vol. 77, no. 23, pp. 7695–7701, 2005.

[41] K. G. Kreider, M. J. Tarlov, and J. P. Cline, "Sputtered thin-film ph electrodes of platinum, palladium, ruthenium, and iridium oxides," *Sensors and Actuators B: Chemical*, vol. 28, no. 3, pp. 167 – 172, 1995.

[42] Q. Li, H. Li, J. Zhang, and Z. Xu, "A novel ph potentiometric sensor based on electrochemically synthesized polybisphenol a films at an ito electrode," *Sensors and Actuators B: Chemical*, vol. 155, no. 2, pp. 730 – 736, 2011.

[43] J. Hendrikse, W. Olthuis, and P. Bergveld, "A method of reducing oxygen induced drift in iridium oxide ph sensors," *Sensors and Actuators B: Chemical*, vol. 53, no. 1, pp. 97 – 103, 1998.

[44] M. A. G. Zevenbergen, G. Altena, V. A. T. Dam, M. Goedbloed, P. Bembnowicz, P. McGuinness, H. Berney, A. Berduque, T. O'Dwyer, and R. van Schaijk, "Solid state ph and chloride sensor with microfluidic reference electrode," in *2016 IEEE International Electron Devices Meeting (IEDM)*, pp. 26.1.1–26.1.4, Dec 2016.

[45] C. Miao and V. Mikko, "2015227394 al, australian patent." https://worldwide.espacenet.com/publicationDetails/biblio?FT=D&date=20180425&DB=&locale=en_EP&CC=EP&NR=3189327A4&KC=A4&ND=1, 2015.

3

EXPERIMENTAL SETUP AND RADIOLYSIS SIMULATION

3.1. APPROACH

Learning from literature review sets guidelines to design pH sensor and measuring performance characteristics. Since this is the first attempt to measure pH for TEM liquid nanocell, requirements for performance parameters are not defined quite strictly. This study reveals up to how much extent pH can be measure using the open circuit potential method for pH change due to radiolysis. Sensitivity is the main parameter that represents up to what magnitude pH resolution can be achieved. Drift and Hysteresis are parameters that represent the reliability of the pH sensor. The impedance characteristic of the sensor membrane is also measured to derive charge transfer resistance and double-layer capacitance. Comparison of these characteristics for two materials Platinum (Pt) and Iridium oxide is done. After that final design is proposed based on numerical analysis from radiolysis species generation. Combining radiolysis simulation and experiments, error estimation is made on the final design. The following section discusses the experimental methods used for characterization.

3.2. EXPERIMENTAL SETUP

Since the potentiometric method is considered here to measure pH, two electrodes are needed for it. Ideally, two electrodes should be on the chip and pH should vary in the area marked as a black circle (figure 3.1). So it allows measurement of differential pH between two electrodes. One of the methods to vary pH locally is using TEM, which generates an electron beam near one of the electrodes changing pH in a nearby area. But electron beam and solution interaction generate a lot of other species, making pH meter characteristics measurement difficult to interpret. So the configuration is shown in figure 3.1 is only used for interference measurement due to radiolysis species. To measure drift, hysteresis, sensitivity external reference electrode arrangement (figure 3.3) is used. The addition of an external reference electrode brings a new challenge to set up, which

is described in the next section.
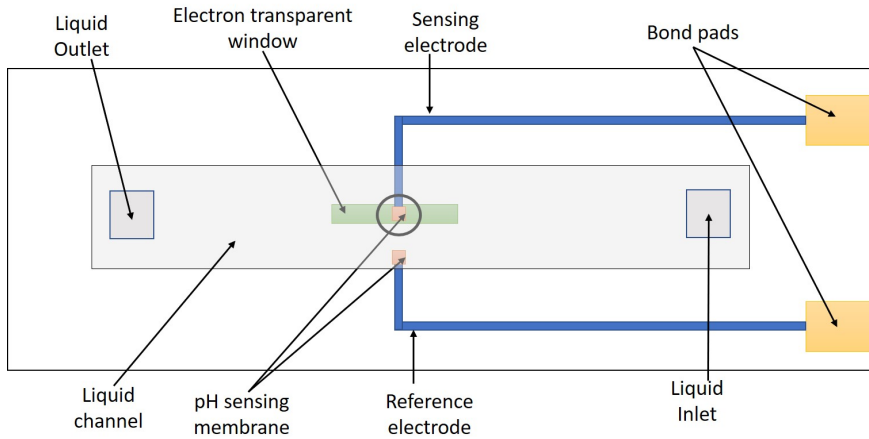
Figure 3.1: Schematic of on chip electrodes to measure pH. Inlet, outlet and flow channel facilitate flow of liquid and bond pads makes electrical connection with outside sensing device.

3.2.1. INTEGRATION OF REAL REFERENCE ELECTRODE

Due to size variation in nanocell and the real reference electrode, the connection between them is a challenge. It is visible from figure 3.2, that flow channel dimensions are approx 10 times smaller compared to the real reference electrode. Especially the thickness of nanocell is around 200-500 nm, which is 10^4 times smaller compared to the reference electrode. Both are connected with a microfluidic channel. Schematic of which is shown in figure 3.3. This microfluidic channel has an approximate length of 20 cm, so it has a high resistive component for charge transfer. Because of this high resistance configuration is very sensitive to electromagnetic noise from the environment. It is important to identify noise sources and eliminate noise as much as possible. To eliminate noise whole setup is placed inside a Faraday cage made of Aluminium foil. Apart from that instead of using crocodile cables, banana cables are used for connections. That further reduced the noise. The laptop charging adapter is also creating noise in the system, so while taking reading it is disconnected. Noise reduction is shown in table 3.1. To measure noise PalmSens4 [1] potentiostat is used. It shows the noise level with color-coding of green, yellow, orange, and red, where green is less noise and red is more noise level. It also gives noise level value scaled to the measurement current range. Noise is reduced 25 times by usage of Faraday-cage and removal of crocodile cables. For all further measurement arrangement for least noise is used. The real experimental setup with the real reference electrode is shown in the appendix B.
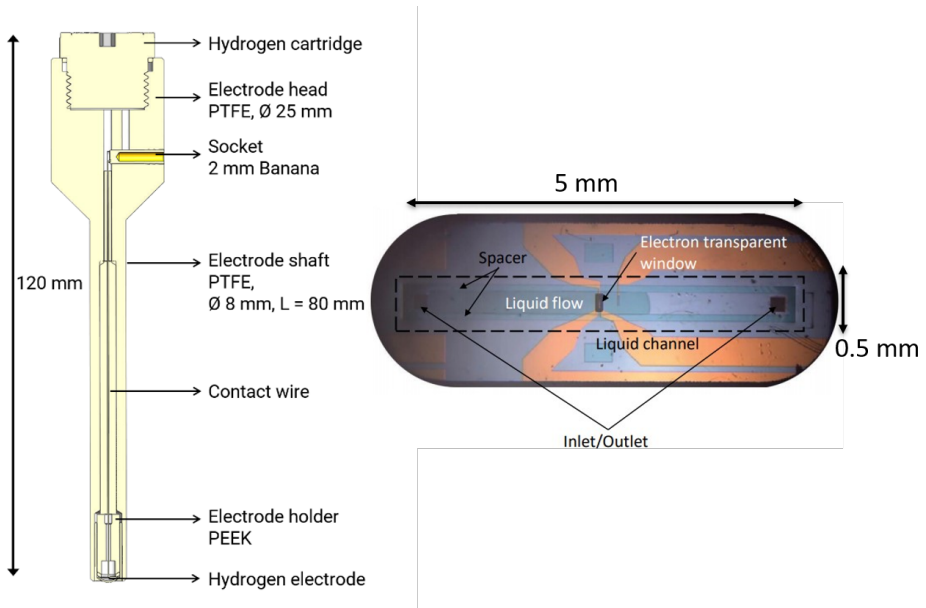
Figure 3.2: Size comparison of nano cell flow channel and real reference electrode [2]
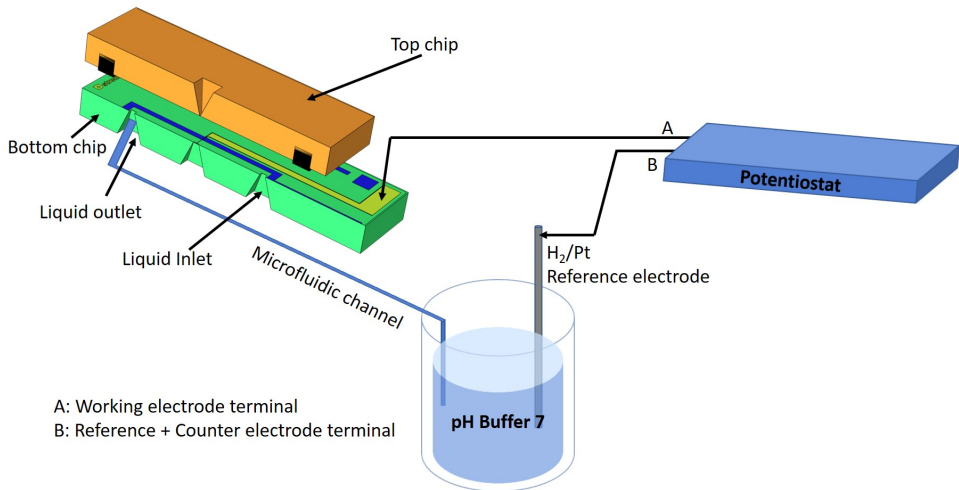
Figure 3.3: Schematic diagram of real reference electrode integrated into system. To visualize inlet and outlet, a sectioned view of the chip is presented. This configuration is used to characterize sensitivity, linearity, hysteresis and drift property of pH sensing membrane.

	Scaled noise value	
Condition	Minimum Noise	Maximum Noise
Laptop power adapter on	-	0.176
Without Faraday cage	0.932	1.014
Using Faraday cage	0.025	0.053
Elimination of crocodile cable	0.025	0.041

Table 3.1: Scaled noise value for different setup conditions. Scaling is done with respect to current range potentiostat is measuring to pick to pick current noise value.

3.2.2. CHIP CONFIGURATION

A flow channel with inlet and outlet is also shown in figure3.4. This chip has three Platinum electrodes. Nomenclature for three on chip electrodes is selected as WE, RE, and CE. Out of three electrodes, only one is used for pH measurement as a pH sensing electrode connected with external the real reference electrode. Electrode covered with white box (Figure3.4) is a platinum electrode. pH sensing characteristics of this is measured. The same electrode is covered with iridium oxide, to measure pH sensing characteristics. The procedure for covering the Platinum electrode with Iridium oxide is given in the next section.
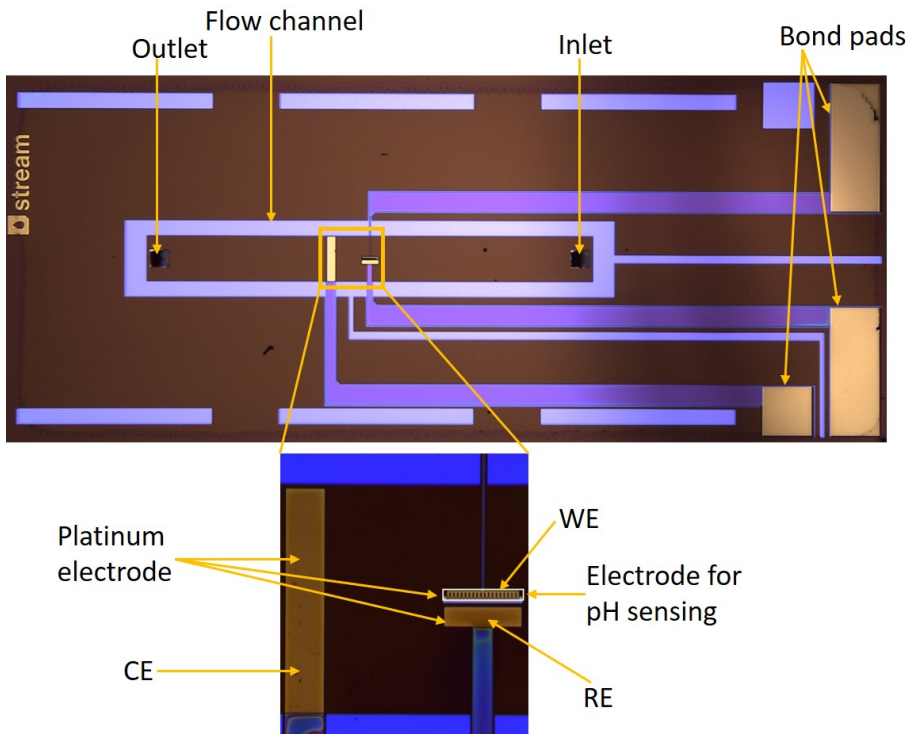
Figure 3.4: Chip configuration showing inlet, outlet, and flow channel for flow of liquid. Nomenclature for three on-chip electrode is also shown:WE, RE and CE.

3.2.3. PRINTING AND CHARACTERIZATION OF IRIDIUM OXIDE

Iridium oxide is deposited as a sensing layer on the electrode shown in figure 3.6. Characterization of this layer is done using Raman spectroscopy to see if annealed material peaks are matching with Iridium oxide peaks from literature. The film thickness is analyzed under the white light interferometer (WLI) and film surface characteristics are observed under the scanning electron microscope (SEM).

PRINTING OF IRIDIUM OXIDE

The deposition of the pH sensing Iridium oxide layer is done by VSParticle nanostructured material printer [3]. It generates nanoparticles from the spark ablation technique. Figure 3.5 shows a schematic of the spark ablation technique. Here two Iridium rods are placed facing each other and a spark is generated by applying 13 W electrical signal. Argon (Ar) is used as a carrier gas with a flow rate of 1 l/min. This gas and nanoparticles mixture passes through a nozzle of size 0.1 mm diameter and nanoparticles are printed on the chip. The scan speed of the printer is 0.8 mm/s and the height from the substrate is kept 600 μm. The gas carrying Iridium nanoparticles is inert, so the printed layer is not oxidized. To oxidize deposited Iridium, annealing is done in atmospheric air on a hot plate. The chip containing the layer of Iridium is put on a hot plate for 4 hours at 400 °C in an open environment.
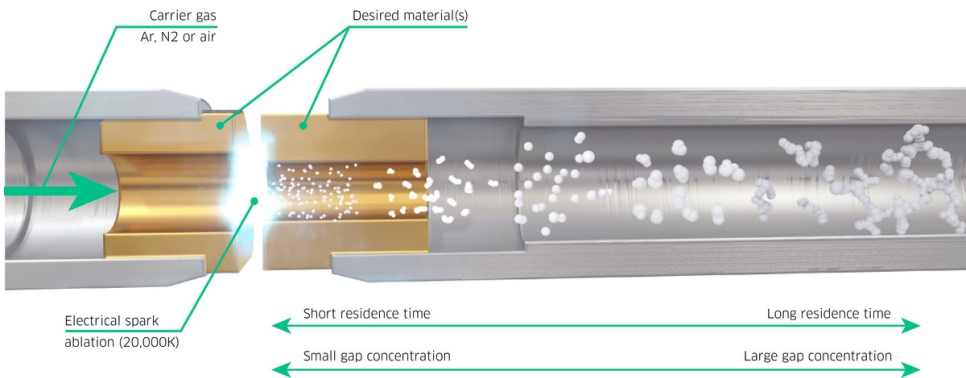
Figure 3.5: Schematic of spark ablation method for generation of nano particles [3].
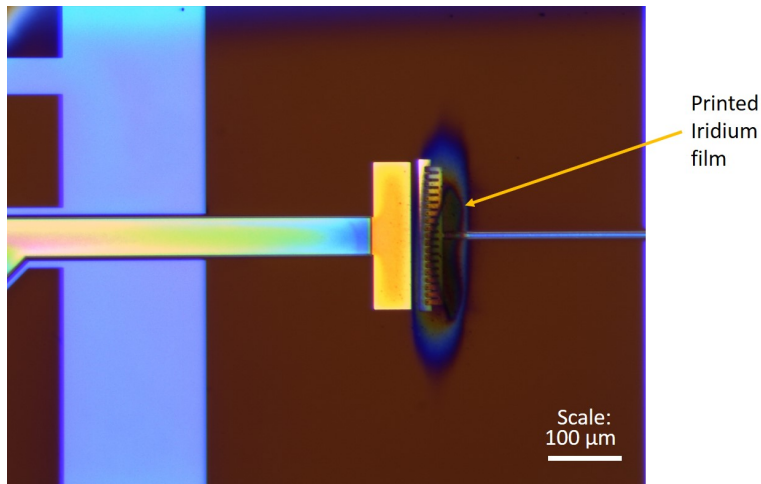
Figure 3.6: Printed Iridium on chip with spark ablation method. Variation in color is due to thickness variation of film.

RAMAN SPECTROSCOPY

Raman measurements are done in the backscattering mode with the Horiba LabRAM S3000 system. Spectra is taken with 514.51 nm frequency laser at 100% (Figure3.7)and 10% (Figure3.8) of intensity. The laser of 5 μm spot size diameter is focused on the sample. Readings are taken from 0 to 1000 cm^{-1} range of wavenumber. It can be concluded from figure3.7 that the peak observed at 520 cm^{-1} with 100% intensity of the laser is because of laser penetration up to silicon substrate. Because of this peaks from Iridium oxide are suppressed. When laser intensity is reduced to 10% of the initial level, the penetration depth is reduced and silicon substrate peak disappears(Figure3.8). Three Raman peaks for single crystal IrO_2 are at 561 (E_g), 728 (B_{2g}) and 752 (A_{1g}) cm^{-1} [4]. Raman spectrum is obtained at two different places shows peaks, which are shown in figure3.8. Peaks of B_{2g} and A_{1g} are obtained through deconvolution in which it is assumed to be composed of two Gaussian components. All Raman peaks shift the lower side compared to single-crystal IrO_2, which is in line with observation found from literature [4]. A comparison of Raman peaks for two locations with single-crystal IrO_2 is shown in table3.2. For both locations also Raman peaks slightly deviate. Reason can be a nonuniform structure of Iridium oxide due to nonuniform oxidation or different strains between Iridium oxide and substrate [4]. Additional peaks below 200 cm^{-1} are also detected, the reason for that is unknown.
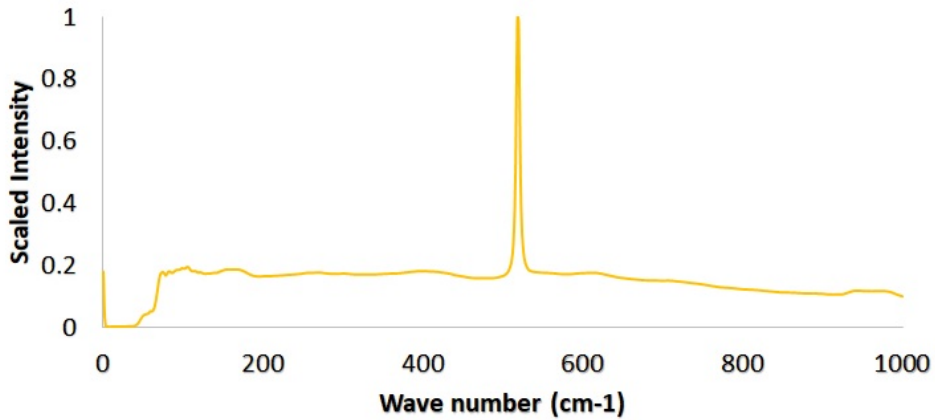
Figure 3.7: Raman spectroscopy result for printed Iridium oxide after annealing at 400 °C for 4 hours with 100 % intensity of laser

	E_g (cm^{-1})	B_{2g} (cm^{-1})	A_{1g} (cm^{-1})
Single crystal [4]	561	728	752
Spot 1	558	725	736
Spot 2	557	728	747

Table 3.2: Raman peaks comparison at two different location with single crystal IrO_2 and printed Iridium oxide after annealing at 400 °C for 4 hours
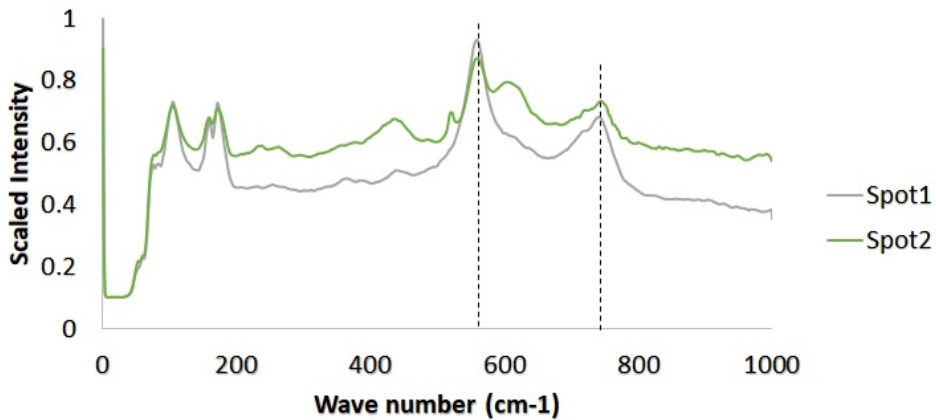
Figure 3.8: Raman spectroscopy result for printed Iridium oxide after annealing at 400 °C for 4 hours with 10 % intensity

THICKNESS OF DEPOSITED IRIDIUM OXIDE

From the literature, it is clear that the thickness of the pH sensing membrane should be more than 80nm. Here printing parameters are set such that a minimum thickness layer is printed. This is because the overall thickness of the nanocell is 200-500 nm. So it is desirable to have minimum thickness electrodes. The thickness of the deposited layer is measured by the white light interferometer. Wyko surface profiler (NT3300) is used for this purpose. First, the thickness of the Platinum layer is measured and then the thickness of the Iridium oxide and Platinum layer is measured together. Both thicknesses are subtracted to get the thickness of the Iridium oxide layer. Although pH measurement is done with electrode WE (figure3.9b), thickness measurement is done at electrode CE (Figure3.9b). The reason for this is, electrode B (Figure3.9b) is on a Silicon nitride suspended membrane. This suspended membrane is not reflective enough to get a measurement with the white light interferometer. An attempt is made to measure thickness at electrode WE (Figure3.10b), which shows very uneven results. So similar Iridium oxide layer is deposited at electrode CE(figure3.9b), and thickness is measured (Figure3.10a).
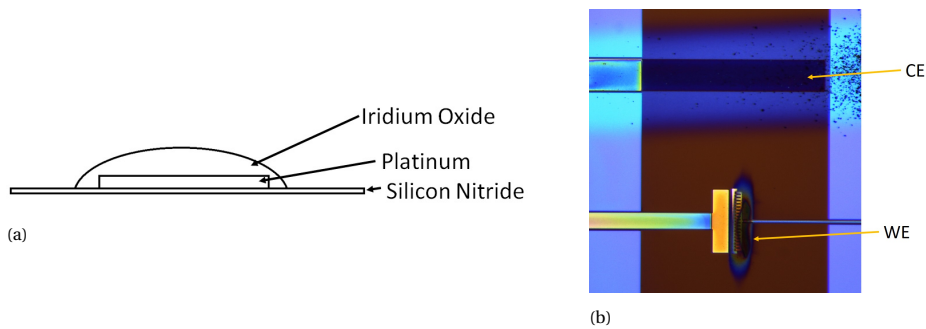
Figure 3.9: (a) Schematic of layers on which Iridium oxide layer is deposited (b) Printed Iridium oxide on chip showing deposition at two location: WE and CE

From the white light interferometer profile, it is clear that the deposited layer is not uniform over the entire electrode. The main reason for this is the deposition technique itself. Since the nanoparticle generator generates particles and their agglomeration process is not precisely controlled. So when they hit the substrate, a non-uniform profile is generated. Particles may fuse and that gives an uneven profile. The thicknesses measured at three locations are shown in table3.3. The thickness of the Iridium oxide layer varies from 138 to 174 nm. Ideally, the thickness should be 80 nm, but the deposition of a very thin layer with this technique could not be achieved.

	Iridium Oxide + Platinum (nm)	Platinum (nm)	Iridium oxide (nm)
Spot 1	318	144	174
Spot 2	282	144	138
Spot 3	302	144	158

Table 3.3: Thickness of Iridium oxide at different location on electrode at CE

(a)

(b)
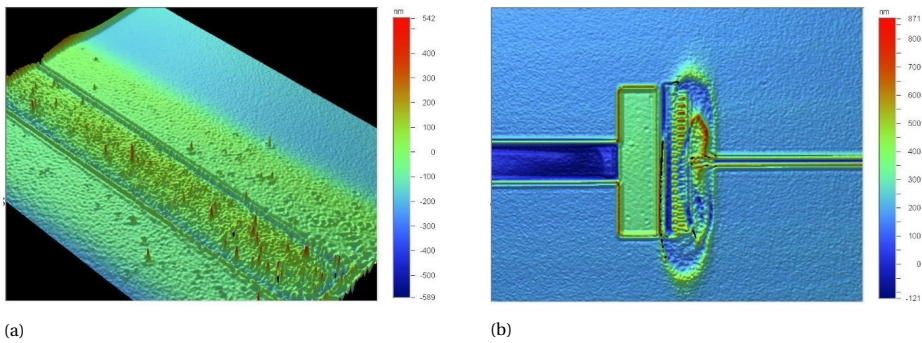
Figure 3.10: Thickness profile with white light interferometer (a) Electrode CE (Figure3.9b) (b) Electrode WE (Figure3.9b)

VISUALIZATION OF IRIDIUM OXIDE SURFACE

Scanning electron microscopy is used to visualize the printed Iridium oxide. Phenom microscope with backscatter detector mode (BDS) is used for this. This microscope has four detectors and it can operate in two modes. In Full mode, it gives contrast mainly due to different sample compositions. Imaging is done with a 5kV beam and 2450X magnification. Iridium oxide has the brightest contrast and the Silicon nitride window has the darkest contrast (Figure3.11a). Imaging in this mode does not reveal the surface features of Iridium oxide. So other image is taken in topographic mode (Figure3.11b). It can be seen that the Iridium oxide membrane is not smooth, but it has a rough surface. In some places agglomeration of particles can also be seen, which is due to the manufacturing process used to deposit this film.

(a)

(b)
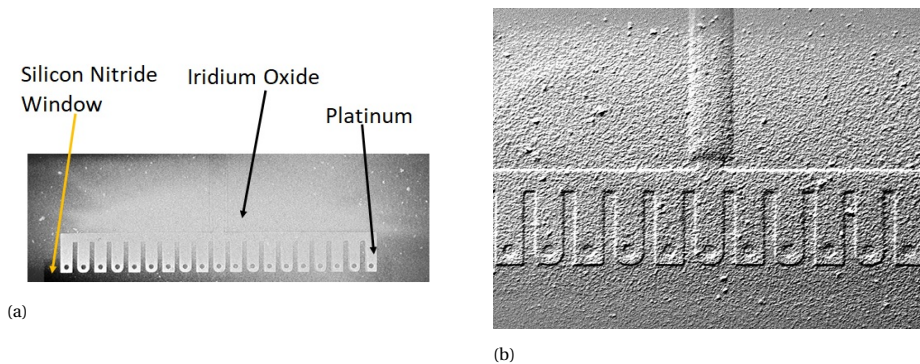
Figure 3.11: SEM image of Iridium oxide membrane (a) Full mode (shows elemental contrast) (b) Topographic mode (showing surface feature)

3.3. PH SENSOR CHARACTERISTICS MEASUREMENT METHOD

pH sensor performance parameter includes sensitivity, linearity, drift, hysteresis, response time analysis, selectivity. Apart from that sensing membrane charge transfer resistance and double-layer capacitance plays important role in sensor performance.

These characteristics are measured using potentiostat Palmsens4.

BASICS OF ELECTROCHEMICAL MEASUREMENT AND POTENTIOSTAT

The characteristics of the pH sensor are analyzed by two electrochemical techniques namely, potentiometry and impedance analysis. Basic of electrochemical measurement and equipment used for measurement is described here.

Electrochemistry is the transfer of the charge from the electrode to another phase, chemical changes take place, and electron and charge transfer occurs. Some examples of electrochemical processes are corrosion, electroplating, water splitting by applying voltage. In these processes, the reaction takes place at the interface of the electrode and electrolyte. Quantification of this electrochemical process is measured by the electrochemical cell. Generally for solid electrode and liquid electrolyte three-electrode setup is used for measurement (Figure 3.12). The working electrode (WE) is the one which is the region of interest for an electrochemical process, reference electrode (RE) is used to measure the potential of the working electrode, and (ideally) no current passes through it. The counter electrode (CE) is used to deliver current so potential between reference and working electrode is controlled.

A potentiostat is used to measure and control the voltage of this electrochemical cell. The schematic of the potentiostat (Palmsens4) is shown in figure 3.13. The reference electrode is connected to a high impedance amplifier. For Palmsens4 impedance is around 1 TΩ, which ensures ideally zero current through this electrode. For potential measurement two modes are present, OCP (Open circuit potential) and Chronopotentiometry. Condition for potential measurement is ideally no current should pass through circuit (Reference and working electrode). This condition is satisfied in OCP and Chronopotentiometry differently. In OCP measurements counter electrode is disconnected and potential is measured between the working and the reference electrodes while a high impedance resistor (1 TΩ) is connected between them. In chronopotentiometry current through working electrode can be set to zero, so it actively maintains zero current by signal manipulation via the counter electrode and measures voltage between the reference and the working electrodes. While the electron beam is passing through the nanocell, some electrons may find its way through the working electrode. Which violates the condition of zero current and ultimately affecting potential readings. While measuring with electron beam no difference is found between OCP and chronopotentiometry, so OCP is used for further measurement.
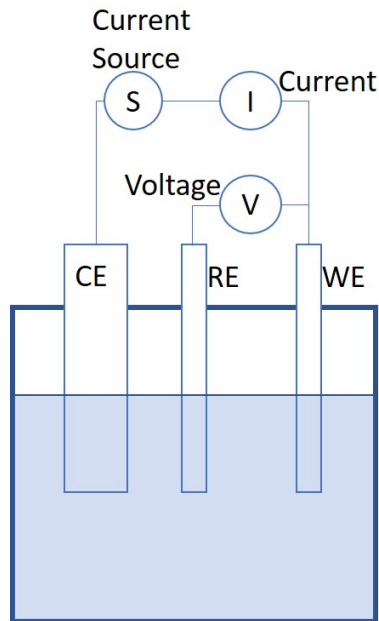
Figure 3.12: Typical electrochemical cell with three electrodes: WE- Working electrode, RE- Reference electrode, CE- Counter electrode
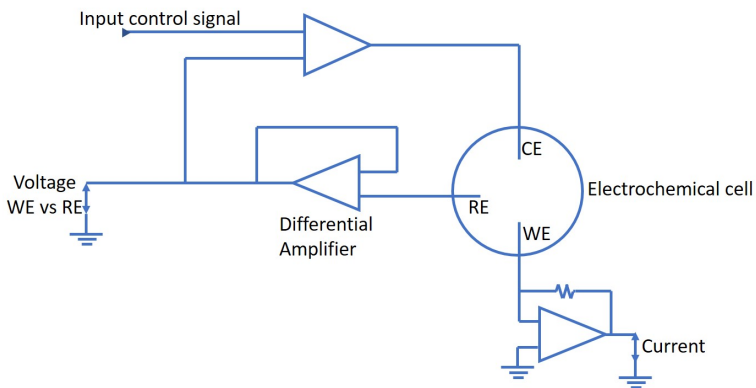
Figure 3.13: Schematic of potentiostat circuit diagram used here for measurement

3.4. RADIOLYSIS SIMULATION

N.M. Schneider et al. [5] have numerically quantified the radiolysis process that was discussed in Chapter 2. Although the explicit value of species generation may not be exact from simulation, they are good to get a qualitative idea for species generation. Here, similar simulations are done for water to see how species are diffusing in current nanocell design, and what species can affect most.

To setup simulation, COMSOL multi-physics is used. The model is setup in chemistry and transport of diluted species module. In the chemistry module, 73 reactions are defined for 16 species. In the transport of diluted species, diffusion coefficients for these species are defined. Data for reaction rates, species generation, and diffusion coefficient is taken from N.M. Schneider et al. [5]. This COMSOL simulation is compared with MATLAB code available from N.M. Schneider et al. [5] and found species concentration is matching from both. Results from the simulations are used for the reasoning of experimental data of potential measurement under the electron beam. Mesh in simulations are used auto generated Normal mesh size. Simulations are done in time domain, and all simulation results are obtained at 2000 seconds. Reason for this is, mostly simulation reaches steady states within few minutes but to make sure it stabilizes data is obtained at 2000 seconds.

3.4.1. OPTIMIZATION

An optimization code is written to define the dimensions of two potential measuring electrodes. The objective of this code is 1. Maximum H^+ ion difference on both electrodes 2. Minimum other species difference on both electrodes. This objective ensures given design measures maximum possible pH change while shielding the effect of other species. Constraints for electrode geometry comes from micro-manufacturing techniques. To ensure a defect-free manufacturing minimum feature size is decided 2 μm. The optimization code is given in the appendix C.2. This optimization is done for 1D geometry. Since the electron beam would be circular and radiolytic products diffuses radially, electrode geometry should be circular. So for optimization thickness of two circular electrodes and the position of these two electrodes with the center of the beam is determined.

REFERENCES

[1] "Palmsens4." https://www.palmsens.com/product/palmsens4/.

[2] "Pt/h2 reference electrode." https://gaskatel.de/en/reference-electrode/.

[3] "Vsparticles nano printer." https://vsparticle.com/products/vsp-p1-nanoporous-printer/.

[4] P. Liao, C. Chen, W. Ho, Y. Huang, and K. Tiong, "Characterization of iro2 thin films by raman spectroscopy," *Thin Solid Films*, vol. 301, no. 1, pp. 7 – 11, 1997.

[5] N. M. Schneider, M. M. Norton, B. J. Mendel, J. M. Grogan, F. M. Ross, and H. H. Bau, "Electron–water interactions and implications for liquid cell electron microscopy," *The Journal of Physical Chemistry C*, vol. 118, no. 38, pp. 22373–22382, 2014.

4

RESULTS AND DISCUSSION

4.1. CHARACTERIZATION FOR PLATINUM ELECTRODE

pH sensing properties of the Platinum electrode are analyzed in this section. Platinum gets equilibrium with H^+ ion, the equilibrium reaction is as follows.

$$2H^+ + 2e^- \rightleftarrows H_2 \tag{4.1}$$

Figure 4.1, shows the Platinum electrode used for characterization of sensitivity, linearity, drift, and hysteresis.
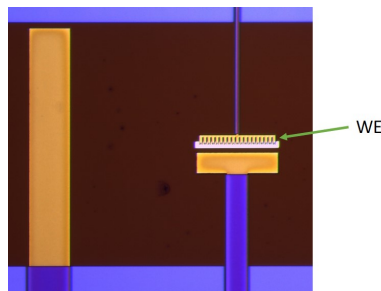
Figure 4.1: Platinum electrode that used for characterization (WE)

4.1.1. SENSITIVITY AND LINEARITY

Ideally at 25 °C, slope from the Nernst equation defines sensitivity -0.059 $\frac{V}{pH}$ (equation 2.5). As it can be observed from figure 4.2, for the Platinum electrode slope is near to that value. For two days this slop is measured, and it is changing over time. For the first day linearity (R^2) of 1 is observed and on the second day, it is dropped to 0.995. Results for sensitivity and linearity are calculated after 500 seconds when a new solution is inserted.
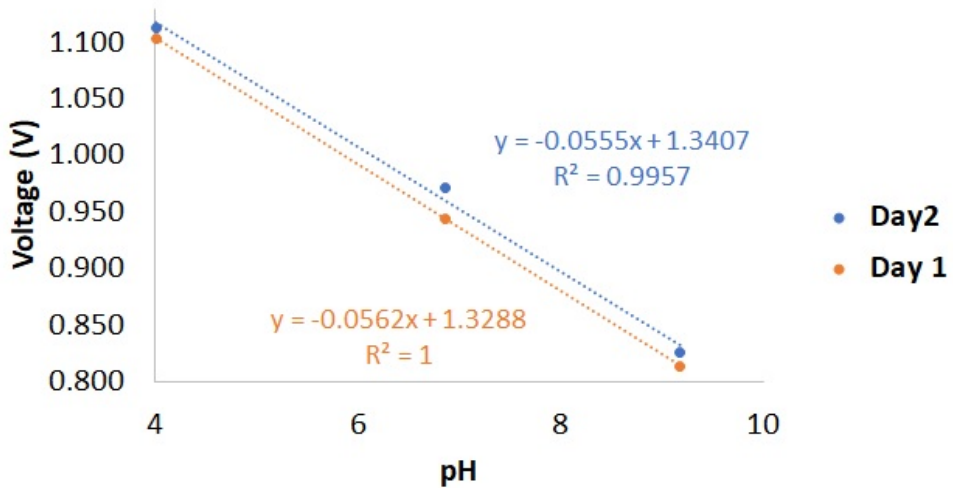
Figure 4.2: Calibration of Platinum electrode showing change in sensitivity and linearity for two days

4.1.2. DRIFT AND HYSTERESIS

Compared to commercial pH meters, a large drift is found for the current Platinum electrode. Also, the drift value is changing for different pH solutions and over time also change in drift is observed. A normal TEM experiment can be several hours long. Drift that is measured here, makes a potential shift of 12-48 mV in one hour. This potential correlates to a pH change of 0.2-0.86 per hour. This magnitude error due to drift is generally undesirable. Drift and Hysteresis are calculated after 500 seconds when a new solution is inserted.

	Drift (mV/min)	
pH	Day 1	Day 2
4.01	0.4	-0.2
6.86	-0.4	0.2
9.18	-0.4	0.8

Table 4.1: Drift for Platinum electrode for three pH buffer solution on day 1 and day 2

To measure hysteresis, pH solutions from 4 to 9.1 are inserted in the nanocell (figure 4.3). Maximum hysteresis of 28 mV is found for pH buffer 6.86 solution. From the sensitivity graph (figure 4.2) it can be seen that the potential of the reference electrode is shifted by 12 mV, so compensating that hysteresis for pH 4.01, 6.86, and 9.18 is -2 mV, 16 mV and 0 mV respectively.
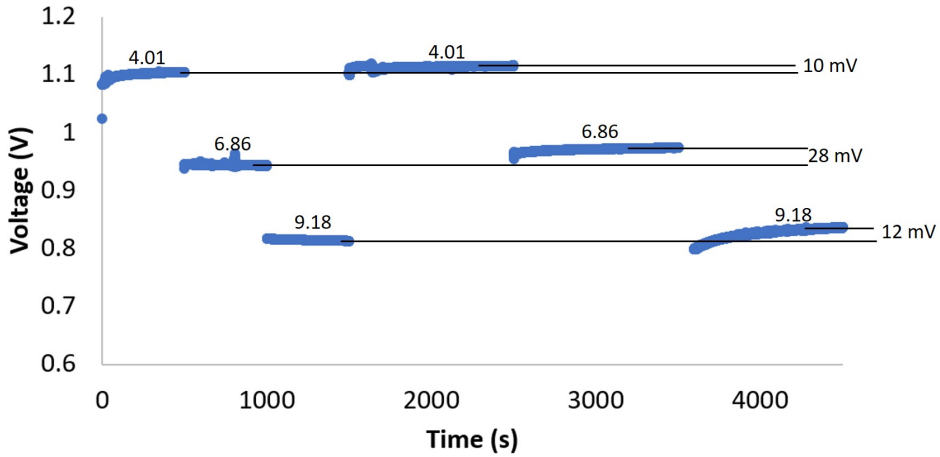
Figure 4.3: Hysteresis for Platinum electrode from measured potential on day 1 and day 2

4.1.3. IMPEDANCE ANALYSIS

Impedance analysis can give information about solution resistance and charge transfer resistance. For this frequency spectrum from 1K to 0.1 Hz is scanned for 5 mV signal. Nyquist plot (figure 4.4) shows measured spectrum. A basic impedance electrical circuit (figure 2.16) is fitted for these results to obtain solution resistance and charge transfer resistance (table 4.2). Solution resistance for pH 6.86 is highest, which is in line with the concentration of H^+ and OH^- ions present. Charge transfer resistance for the given configuration is in the GOhm range.
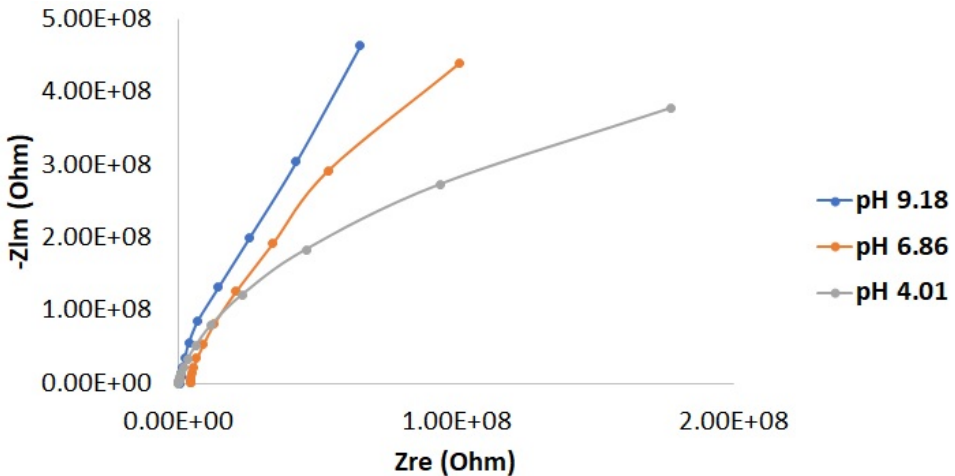
Figure 4.4: Impedance analysis for 1K to 0.1 Hz spectrum, with 5mV signal

pH	Rct Charge Transfer resistance (Ohm cm^2)	Cdl Double layer capacitance ($\mu F/cm^2$)	Rs Solution resistance (Ohm)
4.01	2.77E4	86.8	5.10E+04
6.86	5.54E4	94.8	4.60E+06
9.18	7.83E4	88.3	3.80E+05

Table 4.2: Fitted circuit components for impedance measured for 1K to 0.1 Hz spectrum, with 5mV signal

4.1.4. TEM ANALYSIS FOR SPECIES INTERFERENCE

Radiolysis of water generates 15 species. Out of which, within the beam area all species are present in varying concentrations. But just outside the beam area, many unstable species concentration decreases drastically. Radiolysis simulation is done for water to determine what species has comparatively more concentration with H^+ ions outside the beam area. It is found that H_2, H_2O_2, O_2, and O_2^- have comparatively more concentration just outside the beam area. Other species are present in concentration around 10 times or less compared to H^+ (appendix D.2).

Measurement of potential is done between two electrodes WE and RE (figure 4.5). The solution is flown through nanocell passing over electrodes and the electron beam of size around 3.5 μm is positioned nearby WE. Then keeping beam position and size constant, beam current changed. For this arrangement, change in potential is recorded. Beam current changes dose rate, which changes species generation. Change in species generation with dose rate is shown in appendix D.3. H_2 and H_2O_2 is generated more in acidic pH solutions. O_2^- and O_2 are generated more in basic pH solution. The pH of the basic solutions changes to acidic and for solutions with pH 4 or less pH does not change much due to the electron beam (figure 2.5).
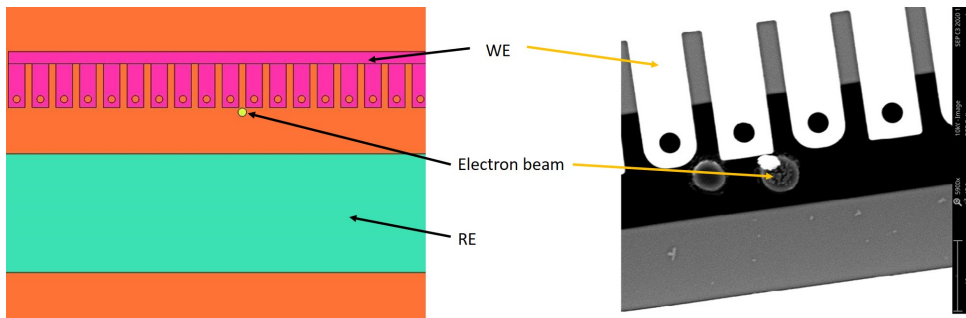
Figure 4.5: Schematic and SEM image of chip with electron beam spot. Electron beam size is 3.5 μm.

In TEM to change the current, finite numbers of steps (from 1 to 10) are available named as spot size. As spot size changes, current changes and that makes a change in dose rate. Current is calculated with equation 4.2 [1]. Where exposure time is measured from the screen with each spot size. From current the dose rate is calculated from equation 2.1. To calculate the dose rate thickness of nano cell is not available, so the dose rate is calculated for nano cell thickness of 200-500 nm. The value of the dose rate varies

from 10^6 to 10^8 Gy/s (appendix D.4). Potential change is observed for Ultra pure water (pH 7.2), pH buffer 4, and H_2SO_4 solution with pH 2.45.

$$Current(A) = \frac{(1.875 * 10^{-12}) * 2 * 1.3}{Exposuretime(s)} \tag{4.2}$$

Ultrapure Water (pH 7.2) is flown into the nanocell, and then the electron beam is turned on. Spot size is changed from 7-6-5-4-5-6-7, and potential is measured for that. Initially, when the electron beam is turned on, a big jump (around 80 mV) is observed in a positive direction. With time this has drifted to the negative potential region. After that, as the dose rate is increased the potential goes towards more negative. And when the dose rate is decreased the potential jumps towards positive. These potential jumps are around 10 mV (figure 4.6). At the end of this measurement, a bubble is observed inside the nanocell.
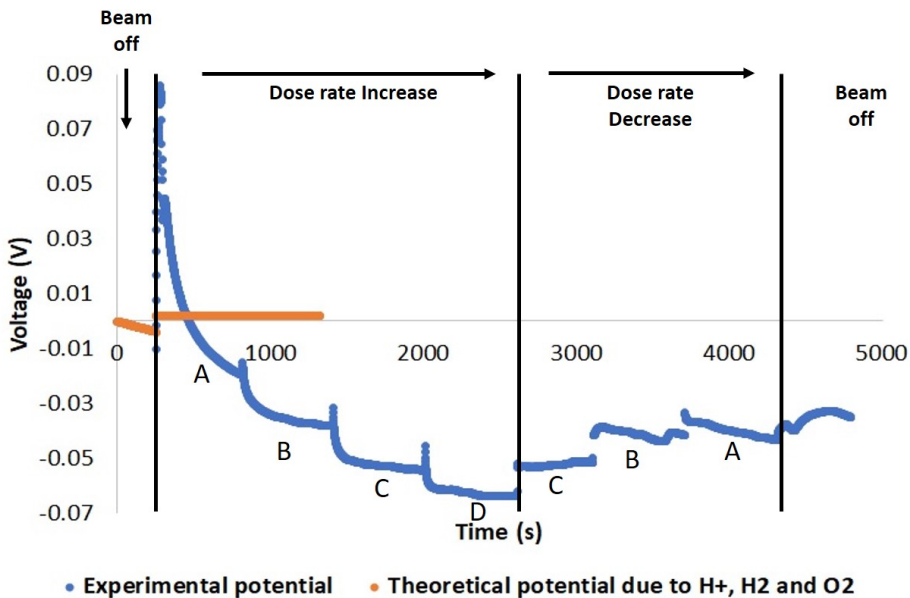
Figure 4.6: Potential between WE and RE, for ultra pure water with changing electron beam spot size. A, B, C, D corresponds to spot size 7, 6, 5, 4 respectively. Dose rate calculation for a given spot size is given in appendix D.4. Theoretical potential is relevant for only jump in potential when the electron beam is turned on. Before that, the drift in potential is superimposed with the experimental result.

pH buffer 4.01 is flown into the nanocell, and then the electron beam is turned on. Spot size is changed from 7-6-5-4-5-6-7, and potential is measured for that. Initially, when the electron beam is turned on, a big jump (around 200 mV) is observed in the positive direction. Unlike ultra pure water, this did not drift to the negative potential region. After that, as the dose rate is increased the potential goes towards more positive. And when the dose rate is decreased the potential jumps towards negative. These potential jumps are around 10 mV (figure 4.7).
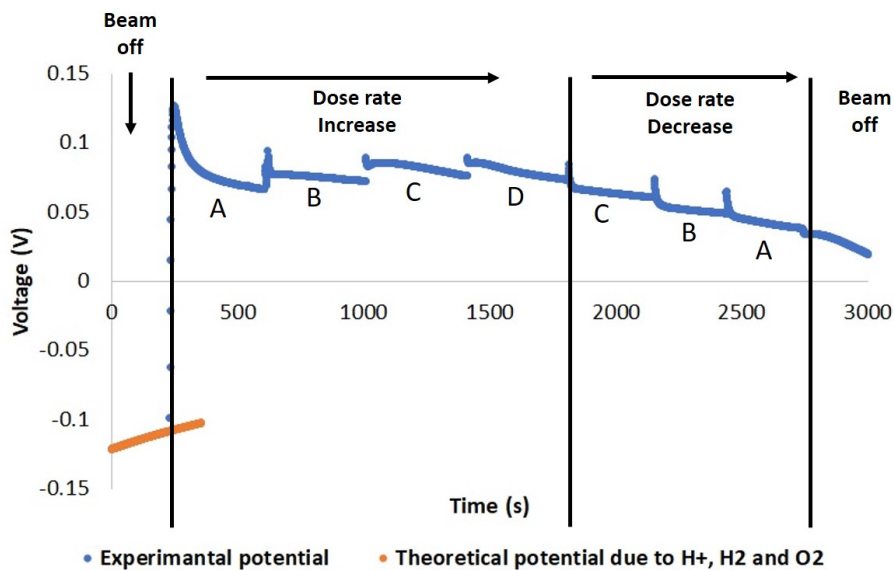
Figure 4.7: Potential between WE and RE, for pH buffer 4.01 with changing electron beam spot size. A, B, C, D corresponds to spot size 7, 6, 5, 4 respectively. Dose rate calculation for a given spot size is given in appendix D.4. Theoretical potential is relevant for only jump in potential when the electron beam is turned on. Before that, the drift in potential is superimposed with the experimental result.

In both experiments (figure 4.6 and 4.7), potential jumps are in the opposite way with the dose rate change. From the spot size, current is calculated and from the current, dose rate is obtained (appendix D.4). This dose rate ranges from 10^6 to 10^8 $\frac{Gy}{s}$. COMSOL simulation (appendix C.1) is done to see species concentration at two electrodes (WE and RE) (appendix D.2). From simulations, potential change due to $H_2 \& H^+$ and $O_2 \& H^+$ generation is calculated. The orange line (figure 4.6 and 4.7) in both figures represents theoretical potential change due to the generation of H_2, O_2 and H^+. Theoretical potential is relevant for the jump in potential when the electron beam is turned on. Before that, the drift in potential is superimposed with the experimental result. For Ultra pure water potential change is a few mV positive and for pH buffer 4.01 potential change is less than 1 mV (appendix D.5). Theoretical potential change is not matching with experimental potential change. The reason can be other species that are generated in comparable concentrations (mostly H_2O_2 and O_2^-). A similar experiment is done for H_2SO_4 solution(figure D.5) of pH 2.45. The potential for that varies in similar trends to the pH buffer 4.01 solution.

The experiments discussed above are potential measurements between WE and RE. Those both electrodes are 20 μm apart from each other. Other experiments are done to see the species diffusion effect in far away areas. For this, potential measurement is done between WE and CE. WE and CE electrodes are around 400 μm apart from each other. So this can give information about less diffusing species. Ultra pure water + KCl (40 g/L) solution (pH 7.2) is prepared. This solution is illuminated with an electron beam similar to previous experiments, and with different spot size potential between WE and

CE is measured. Figure 4.8 shows the potential change between WE and CE electrodes. Here, potential increases with dose rate increase and decrease with dose rate decrease. For this solution potential between WE and RE (figure D.6) follows a similar trend with potential from Ultra pure water.
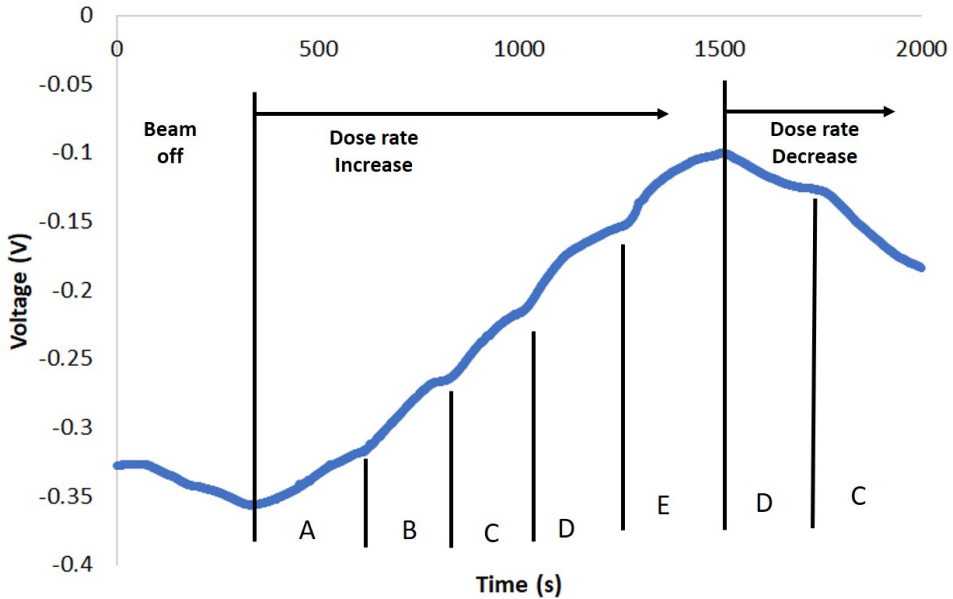
Figure 4.8: Potential between WE and CE, for Ultra pure water + (40 g/L) solution (pH 7.2) with changing electron beam spot size. A, B, C, D, E corresponds to spot size 7, 6, 5, 4, 3 respectively. Dose rate calculation for a given spot size is given in appendix D.4.

4.2. CHARACTERIZATION FOR IRIDIUM OXIDE

pH sensing properties of the Iridium oxide electrode are analyzed in this section. Iridium oxide gets equilibrium with H^+ ion, the equilibrium reaction is as follows.

$$IrO_x(OH)_{n-x} + xH^+ + xe^- \rightleftarrows Ir(OH)_n \tag{4.3}$$
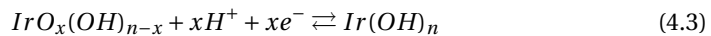
4.2.1. SENSITIVITY AND LINEARITY

Ideally at $25\,^{\circ}C$, slope from the Nernst equation defines sensitivity -0.059 $\frac{V}{pH}$ (equation 2.5). For the Iridium oxide electrode slope is varying between -0.63 to -0.7 $\frac{V}{pH}$ (figure 4.10). For four days this slop is measured, and it is changing over time. For first the day linearity (R^2) of 0.942 is observed and for the third day, it increased to 0.997. Results for sensitivity and linearity are calculated after 500 seconds when a new solution is inserted.
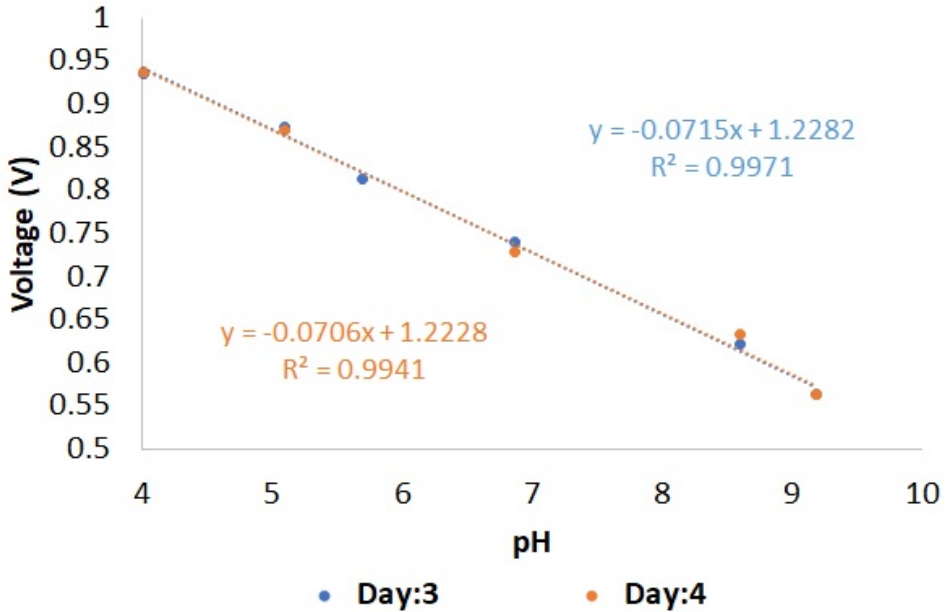
Figure 4.9: Calibration of Iridium oxide electrode showing change in sensitivity and linearity for two days

Day	Slope (mV/pH)	R^2
1	-63.9	0.942
2	-66.1	0.958
3	-71.5	0.997
4	-70.6	0.994

Figure 4.10: Sensitivity and linearity of Iridium oxide over four days

4.2.2. DRIFT AND HYSTERESIS

Compared to the commercial pH meters, a large drift is found. Also drift is changing for different pH solutions and over time also change in drift is observed. A normal TEM experiment can be several hours long. Drift that is measured here, makes a potential shift of 4 to 53 mV in one hour. This potential correlates to the pH change of 0.05-0.75 per hour. This magnitude error due to drift is generally undesirable. Drift and Hysteresis are calculated after 500 seconds when a new solution is inserted.

	Drift (mV/min)	
pH	Day 3	Day 4
4.01	0.13	-1.38
5.1	-0.07	-0.32
5.7	0.70	-0.59
6.86	-0.23	-2.77
8.6	-0.68	-
9.18	-0.89	0.45

Table 4.3: Drift for Platinum electrode over two days

To measure hysteresis, pH solutions from 4-9.18 are inserted in the nanocell (figure 4.11). Maximum hysteresis of 12 mV is found for pH buffer 8.6 solution. From the sensitivity graph (figure 4.9) it can be seen that the potential of the reference electrode is shifted by -6 mV, so compensating that hysteresis for pH 4.01, 5.1, 6.86, and 8.6 is 7 mV, 2 mV, -5, and 18 mV respectively.
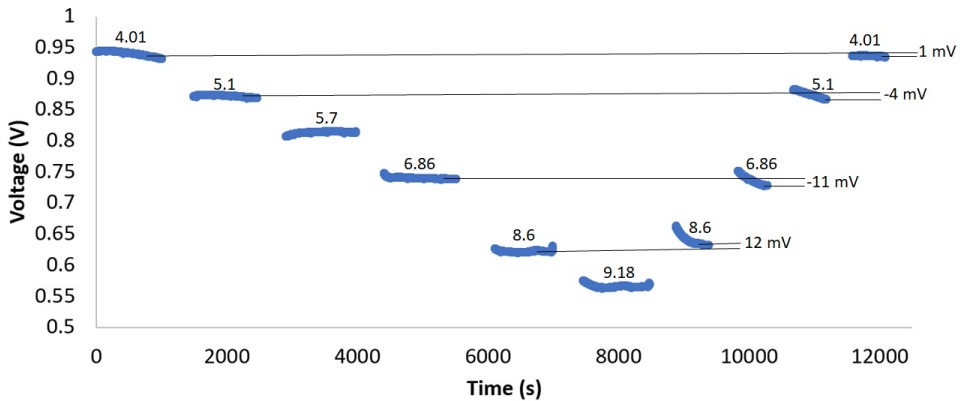
Figure 4.11: Hysteresis for Iridium oxide electrode

4.3. DISCUSSION FROM EXPERIMENTS

PLATINUM ELECTRODE

Sensitivity changes from -0.056 to -0.055 $\frac{mV}{pH}$ over one day. So if it is calibrated, after one day this calibration can give an error of 1 $\frac{mV}{pH}$. This translates to an error per pH change of 0.02. Due to linearity on day 1 error is zero, but on day 2 linearity is 0.995, this gives a maximum error of 0.1 pH. As discussed in section 4.1.2, because of drift pH error can be 0.86 per hour. Due to hysteresis pH error can be 0.3. Analyzing data, it can be said that due to drift absolute pH measurement is not possible with the Platinum electrode with current design and manufacturing. Only if pH change is to be measured, the error can be the sum of errors due to sensitivity, hysteresis, and linearity. This gives a maximum error of 0.4 pH.

Impedance analysis suggests that charge transfer resistance is in order of GOhm. Potentiostat measuring potential has a resistance of 1 TOhm. This gives an error in a potential measurement of 0.1 %. Generally, as the surface area of electrode decrease, charge transfer resistance increase. So if charge transfer resistance increases to 10 GOhm error in potential measurement can be 1 %.

PLATINUM ELECTRODE TEM EXPERIMENT

As discussed in section 4.1.4, the potential measurement can not be explained by only considering the effect of H_2, O_2, and H^+. So here an attempt is made to describe this potential change with other species that are present in relatively high concentration (H_2O_2 and O_2^-). For H_2O_2 potential change is given in figure 4.12. As concentration of H_2O_2 increases potential increases. For O_2^- effect of potential is unknown.
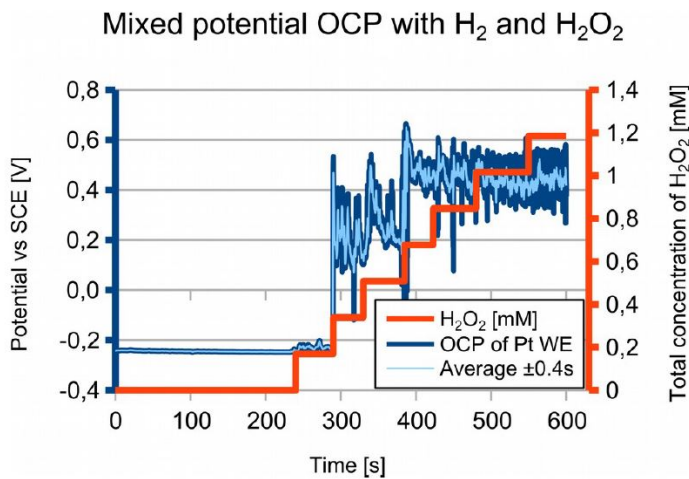
Figure 4.12: Potential change due to H_2O_2 over Platinum electrode [2]

Generation of H_2O_2 is higher for acidic solutions and for basic solutions generation of O_2^- is higher (appendix D.3). For pH buffer 4.01 and H_2SO_4 solutions, the potential jump is positive with the dose rate increase. And from simulation (appendix D.2), these solutions has almost twice concentration of H_2O_2 and 10 times less concentration of O_2^- compared to water(pH 7). So positive potential shift can be due to H_2O_2 in acidic solutions. For ultra pure water (figure 4.6), a negative potential shift can be due to O_2^- ions. When potential is measured between WE and CE for Ultra pure water + KCl solution (figure 4.8), potential increases. From simulation (figure 4.13), concentration decrease for H_2O_2 is more than twice compared to O_2^- over distance between WE and CE. This implies potential difference can be affected more by H_2O_2. The overall conclusion from this experiment is the position of electrodes can affect the potential measurement and two Major potential affecting species for a Platinum electrode are H_2O_2 and O_2^-. Another takeaway point from these experiments is, simulation for radiolysis species generation may not be accurate but qualitatively it is useful to reason out potential change.
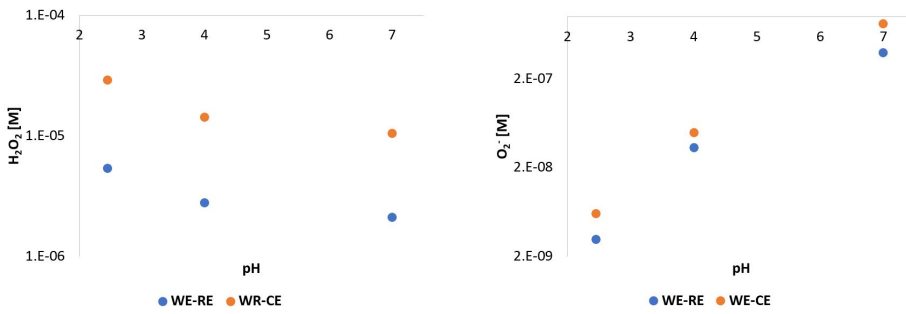
Figure 4.13: Concentration difference over WE & RE and WE & CE for (a) H_2O_2 (b) O_2^- at dose rate of 10^8 Gy/s with numerical simulation

4

IRIDIUM OXIDE ELECTRODE

As equation 4.3 suggests, Iridium oxide gets hydrated and then gets equilibrium with H^+ ions. Literature suggests hydration of Iridium oxide may take several hours. A major change in sensitivity is observed for day 1 and day 2, so it is assumed that this is due to the time it took for hydration of film. Apart from that, oxide composition may change to a more stable composition over time. So here error is calculated from results for day 3 and day 4. Sensitivity changes from -0.071 to -0.07 $\frac{mV}{pH}$ from day 3 to 4. So if it is calibrated, after one day this calibration can give an error of 1 $\frac{mV}{pH}$. This translates to an error per pH change of 0.015. Due to linearity on day 3 maximum error is 0.13 pH, but on day 4 linearity is 0.994, this gives a maximum error of 0.16 pH. As discussed in section 4.2.2, because of the drift pH error can be 0.75 pH per hour. Due to the hysteresis pH error can be 0.25 pH. Analyzing data, it can be said that due to drift absolute pH measurement is not possible with the Iridium oxide electrode with current design and manufacturing. Only if pH change is to be measured, the error can be sum of errors due to sensitivity, hysteresis, and linearity. This gives a maximum error of 0.4 pH.

4.4. DESIGN OF PH MEASURING ELECTRODE

Here, an attempt is made to design electrodes to measure pH with minimum interference from other species due to radiolysis. From experiments with the Platinum, it is clear that pH measurement with potential measurement technique is not possible because of interference of H_2O_2 and O_2^-. From the literature review, it is found that Iridium oxide is the best choice to reduce species interference. It has selectivity of around 10^{-4} for H_2O_2 [3]. For H_2 and O_2 it's potential changes negligible [4]. So selectivity for H_2 and O_2 is taken as zero. For O_2^- selectivity of Iridium oxide is not known. So optimization code is written (appendix C.2) to find the optimum positions and dimensions of two potential measuring electrodes. The Geometry of these two electrodes would be circular because of the radial diffusion of radiolytic products. One of the constrain for the optimization is WE and RE should have the same area. This constraint is placed to reduce drift in the sensor. If both electrodes are made of the same material with the same area, drift due to some unknown slow processes occurring at surface would be reduced up to a certain extent. Optimized dimensions for WE and RE are also found without considering same

surface area constraint.

One of the important things here is that Since selectivity of O_2^- is unknown, the design is made for two selectivities, 1 and 0.1.

- Selectivity $H_2O_2 = 10^{-4}$ ans $O_2^- = 1$

  For these parameters, the optimization code gives the position of both electrodes should be as far away as possible from the center of the beam. If both electrodes are allowed to be placed up to 100 μm radius far from the electron beam, then WE would be at radius 95 μm and RE would be at 99μm radius with the center of the beam (figure 4.14). With this design 1, measurable pH change is shown in figure 4.16. Practically this arrangement is too far to measure noticeable pH change.
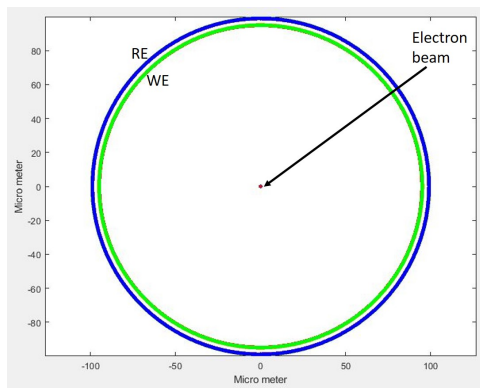
Figure 4.14: Design 1: Optimized design of electrodes for selectivity $H_2O_2 = 10^{-4}$ ans $O_2^- = 1$. Green color: WE, and Blue color: RE

- Selectivity $H_2O_2 = 10^{-4}$ and $O_2^- = 0.1$

  With the constraint of similar area for WE and RE optimized position and size of electrodes is: 2.4 μm (r1) to 6.78 μm (r2) and for RE: 9μm (r3) to 11 μm (r4) (figure 4.15a). Without the constraint of similar area for WE and RE optimized position and size of electrodes is: 2.4 μm (r1) to 4.4 μm (r2) and for RE: 47μm (r3) to 50 μm (r4) (figure 4.15b). For both designs, pH change from radiolysis simulation is given in figure 4.16. It is obvious that within beam region pH change is maximum and for design 1, pH change is almost negligible to detect. With design 2 measurable pH change is 0.12 to 0.44 pH, and for design 3 it is 0.44 to 1.34 pH with the dose rate of 10^7 to 10^{10} Gy/s.

(a) Design 2

(b) Design 3
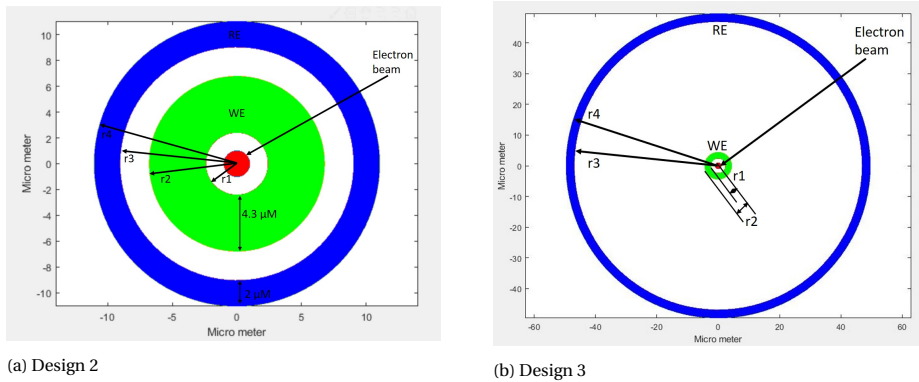
Figure 4.15: Electrode dimensions and position (a) Optimized with constraint of similar area of WE and RE (b) Optimized without constraint of similar area for WE and RE, Green color: WE and Blue color: RE

4
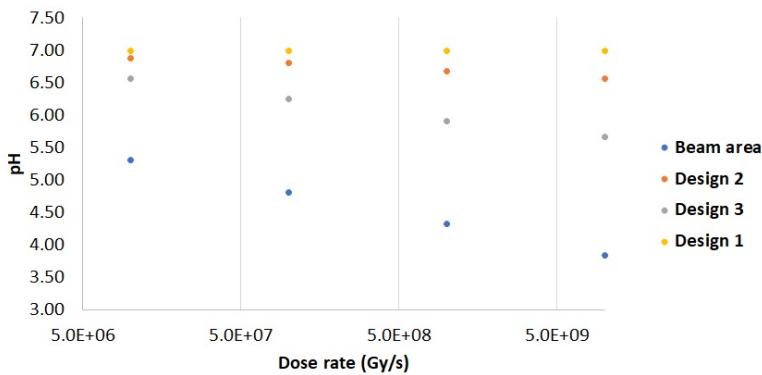
Figure 4.16: Simulation result showing measurable pH change for different placement of electrodes (Design 1, Design 2 and Design 3) for solution with initial pH 7

PROPOSED DESIGN FOR PH SENSOR

Measurable pH change due to $H+$ ions outside the beam area with three discussed designs is 1.34 pH at maximum. From the Iridium oxide pH characteristics measurements, the maximum pH error is 0.4. So it is possible to measure pH at dose rate in the range of 10^8 to 10^{10} Gy/s. For pH measurement, one requires two electrodes on-chip, and the current chip configuration offers space to place four electrodes on-chip. So a combination of design 2 and design 3 can be made on a chip that measures pH with different accuracy and magnitude. Placing two WE from design 2 and design 3 is not possible because they overlap. To assess that same area for WE and RE results in reduced drift, WE and RE from design 2 are considered. To measure large voltage differences RE from design 3 is considered so that large pH change can be observed. The final design with three electrodes is shown in figure 4.17. Overall chip design (figure 4.18) and layer by layer design (appendix D.7) of pH sensing electrode shows visualization of the final design.
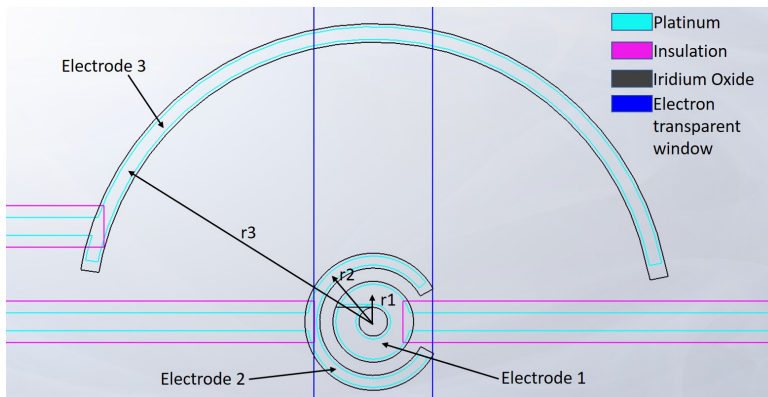
Figure 4.17: Electrode configuration for pH measurement with three different layer on chip, Average distance from center r1=4.5 μm, r2=10.2 μm, r3=48.4 μm. Two pH measurement configurations, Configuration A: Electrode 1 and Electrode 2, Configuration B: Electrode 1 and Electrode 3
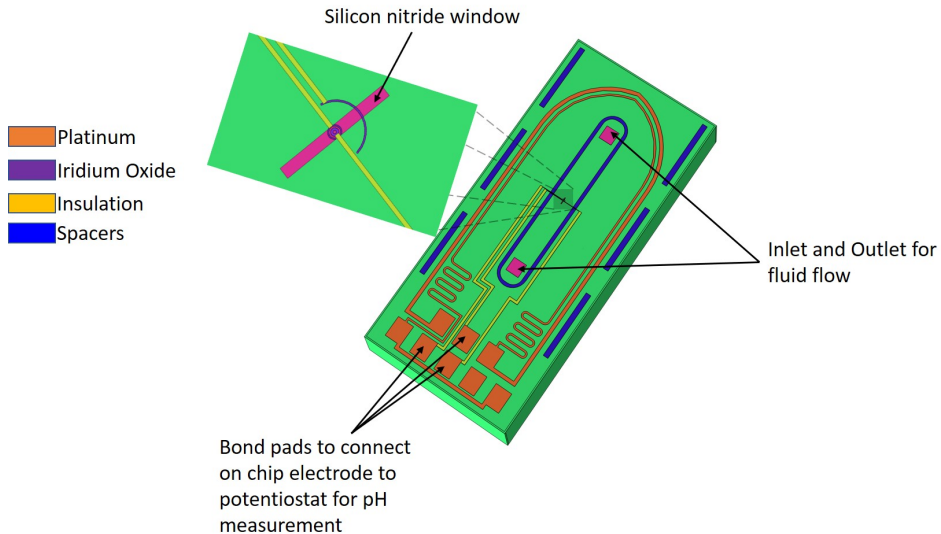
Figure 4.18: Overall chip design representing pH sensing electrodes and other features

From this design, two configurations can be used to measure pH change. Electrode 1 and Electrode 2 can be used to measure pH (configuration A), where Electrode 1 should be connected to the working electrode probe and Electrode 2 to the reference electrode probe of the potentiostat. Configuration B can be using Electrode 1 and Electrode 3, where Electrode 1 should be connected to the working electrode probe and Electrode 3 to the reference electrode probe of the potentiostat. COMSOL 2D simulation for this design is done with dose rate ranging from 10^7 to 10^{10} Gy/s, for pH solution 4, 7, and 9. This simulation gives species distribution because of radiolysis over three electrodes. Exam-

ple is given in figure 4.19 for H^+ distribution over three electrodes. From experiments, the sensitivity of the Iridium oxide is taken as 70 $\frac{mV}{pH}$. Using the Nearest equation, the potential is calculated based on simulation. For this selectivity of $H_2O_2 = 10^{-4}$ and $O_2^- = 0.1$, is considered. Calculated potential change and error are shown in appendix 4.17. For pH 7 solution, error ranges from 0-12 % in configuration A, and 1-22 % in configuration B. But the configuration B measures the potential change almost 2 to 3 times than configuration A. For the pH 4 solution, error in measurement is big. It is because due to radiolysis there is no pH change and all potential change that is measured is because of interference from H_2O_2 and O_2^-. Similarly, for the pH 9 solution, error in measurement is big. This is because for basic solutions generation of O_2^- is more that makes a shift in potential. So this design can only be used for the solutions that are near neutral pH to reliably measure pH.
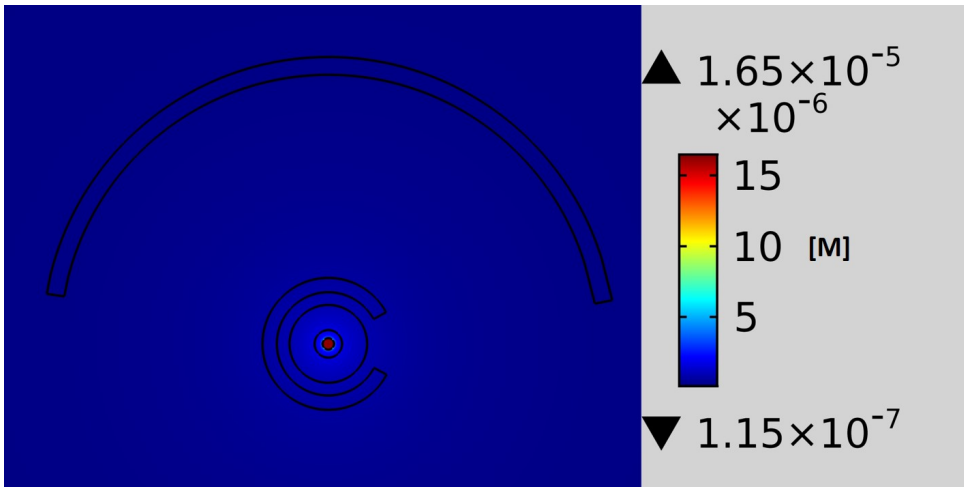
Figure 4.19: Distribution of H^+ ions over area of three electrodes with electron beam of 1 μm radius and 10^8 Gy/s dose rate for initial pH of solution 7

Figure 4.20 shows pH measurement region considering the maximum error for the Iridium oxide pH measurement 0.4 pH and species interference error from simulation (table 4.4 and 4.5). Up to the dose rate of $5 * 10^7$ Gy/s, pH measurement is not possible for any solution with the current design. The typical dose rate in in-situ studies ranges from 10^6 to 10^{10} Gy/s. Within this region pH measurement is possible for solutions with initial pH from 6 to 8. Solutions below pH 6 have very little pH change outside the beam region, which makes potential shift mainly due to other species interference. For basic solutions above pH 8, change in pH is large but due to more generation of O_2^- potential change is getting influenced and makes pH measurement error greater than pH change.

		Configuration A		
Dose rate (Gy/s)	Initial pH	Potential change considering all species (mV)	Potential change considering only H+	Error (%)
1.00E+07	7	9	8	4
5.00E+07	7	13	13	0
1.00E+08	7	16	16	1
1E+09	7	23	25	5
1E+10	7	28	32	12
1.00E+07	4	9	0	79216
5.00E+07	4	11	0	41949
1.00E+08	4	11	0	32775
1E+09	4	12	0	15218
1E+10	4	12	0	6632
1.00E+07	9	4	1	419
5.00E+07	9	5	2	164
1.00E+08	9	5	3	52
1E+09	9	12	120	90
1E+10	9	24	122	81

Table 4.4: Potential change and Error estimation from simulation for configuration A with change in initial pH and dose rate. This error is only due to species interference of H_2O_2 and O_2^-.

		Configuration B		
Dose rate (Gy/s)	Initial pH	Potential change considering all species (mV)	Potential change considering only H+	Error (%)
1.00E+07	7	29	27	8
5.00E+07	7	42	42	1
1.00E+08	7	48	48	1
1E+09	7	60	66	9
1E+10	7	60	77	22
1.00E+07	4	-221	0	1087879
5.00E+07	4	-202	0	513104
1.00E+08	4	-194	0	388561
1E+09	4	-171	0	166021
1E+10	4	-146	0	66549
1.00E+07	9	13	2	727
5.00E+07	9	17	5	253
1.00E+08	9	19	9	115
1E+09	9	30	156	81
1E+10	9	40	189	79

Table 4.5: Potential change and Error estimation from simulation for configuration B with change in initial pH and dose rate. This error is only due to species interference of H_2O_2 and O_2^-.
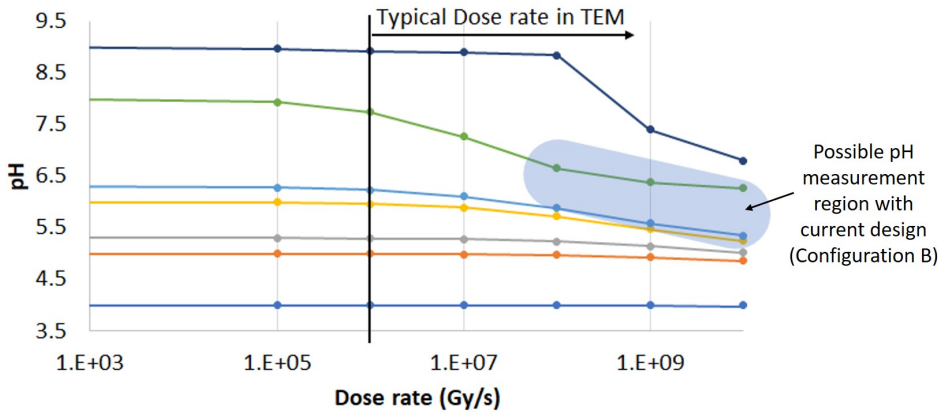
Figure 4.20: pH change with dose rate for configuration B. With Configuration B, pH measurement is possible within the blue region considering error in pH measurement from experiment and species interference error from the simulation.

REFERENCES

[1] "Tecnai 20 mechanics manual, chapter 4." Section 4.6.4.

[2] Møller-Nilsen, *In-situ SEM electrochemistry and radiolysis.* PhD thesis, DTU nanotech, 2016.

[3] K. G. Kreider, M. J. Tarlov, and J. P. Cline, "Sputtered thin-film ph electrodes of platinum, palladium, ruthenium, and iridium oxides," *Sensors and Actuators B: Chemical*, vol. 28, no. 3, pp. 167 – 172, 1995.

[4] S. Głab, A. Hulanicki, G. Edwall, and F. Ingman, "Metal-metal oxide and metal oxide electrodes as ph sensors," *Critical Reviews in Analytical Chemistry*, vol. 21, no. 1, pp. 29–47, 1989.

5

CONCLUSION AND RECOMMENDATION

5.1. CONCLUSION

In liquid cell transmission electron microscopy, the interaction of electron beam with liquid generates many species. One of the species that is getting generated is H^+ ions. This changes the pH of the liquid. The goal of this project was to measure this pH change due to the electron beam. This problem is mainly divided into two challenges. The first challenge is to design a pH sensor for nanocell. The second challenge is to estimate radiolysis products and measure only H^+ ions out of that.

Measuring pH due to radiolysis is a challenging task due to other species present. Just under the beam area, 15 species are present, and evaluating the effect of each one of them on potential is difficult to characterize. So here, an approach is taken to measure pH just outside the beam area, which reduces species from 15 to 5.

Literature review is done to study micro pH sensor characteristics and parameters that affect those characteristics. From the literature review, it is found that the selection of pH sensing material is important for species interference characteristics. As a result IrO_2 is selected as the best material to overcome species interference. Other characteristics like drift, sensitivity, hysteresis depend mainly on the manufacturing technique and post-processing technique used for sensing layer. A limited amount of drift can be controlled by choosing the same area for WR and RE electrodes. Another literature survey is done to estimate radiolysis products. Only numerical studies are available for the estimation of radiolysis. COMSOL simulation is set up for a given chip design to reason out the experimental potential measurement.

Potential measurement while applying electron beam over liquid, verifies relative generation of H_2O_2 and O_2^-. H_2O_2 is generated less in pH 7 solutions compared to acidic solutions, here potential is affected mainly by O_2^- ions. For acidic solutions, O_2^- is generated approximately 10 times less, and H_2O_2 is generated almost two times compared to pH 7 solution. So potential in acidic solution is mostly affected by H_2O_2. Also, species

diffusion is observed with water + KCL solution. For electrodes placed approximately 400 μm far from each other, potential change is mainly due to H_2O_2. Because H_2O_2 does not diffuse to very long distance compared to O_2^-. These observations confirm the qualitative validity of radiolysis simulation. Another takeaway from this experiment is the placement of electrodes compared to the electron beam is very important to shield the effect of radiolysis generated species.

pH sensing properties of Platinum reveals a maximum error of 0.4 pH in measurement. Manufacturing of the Iridium oxide membrane is done to see pH sensing properties. Error estimation concludes that due to Iridium oxide with the current manufacturing technique maximum error is 0.4 pH. Now according to simulations outside the beam area, maximum pH change is 1.34 pH. So there is a possibility of pH measurement within a limited range of dose rate and initial solution of pH.

The proposed optimization code indicated that just by optimizing geometry O_2^- effect can not be shielded. So material should be chosen in such a way that it has selectivity to $O_2^- = 0.1$ or less to measure meaningful pH change outside the beam area. From literature selectivity of Iridium oxide for H_2O_2 is 10^{-4}. From the optimization code dimensions of two pH sensing electrodes are decided. Considering maximum error from pH measurement experiments and error from species interference from simulations for configuration B, pH measurement is possible for dose rate $5*10^7$ Gy/s and above for initial pH of solution ranging from 6 to 8. Improvement in pH sensing layer hysteresis and linearity can further extend this range for pH measurement.

5.2. RECOMMENDATION

The pH measurement process for radiolytic pH change is not straightforward. Stepwise attempts should be made to achieve this target. There is plenty of room to characterize the effect of each radiolytic product on the sensing electrode.

- Radiolysis simulations are several orders of magnitude extrapolation for species generation. No experimental results are available that quantify species generation for a given dose rate. From experiments done to measure potential with neutral and acidic solutions with the change in dose rate shows quantification of H_2O_2 is possible with the Platinum electrode. The Objective function in optimization code can be modified to maximize the effect of H_2O_2 on an electrode and a new design can be proposed for this measurement. The Platinum electrode can be calibrated for H_2O_2 in a similar way as pH sensing properties are measured. For measurement of H_2O_2, acidic solutions are recommended because simulation shows the generation of H_2O_2 is higher at those pH. Other than that dose rate to measure H_2O_2 is recommended to be higher than $5*10^7$ Gy/s, so that solution is near saturation with H_2 dissolved gas. This makes interference from H_2 less and makes measurement of H_2O_2 more accurate. For acidic solutions generation of O_2 is less, so making solution saturated with O_2 can help reducing potential change due to O_2.

- pH sensing membrane should have good selectivity for H^+ ions compared to H_2, O_2, H_2O_2 and O_2^-. For Iridium oxide selectivity with respect to H_2, O_2 and H_2O_2 is known. So it is extremely important to check selectivity for O_2^- and calibration for

that is a challenge. Because for calibration with O_2^-, a known amount of species should be inserted, and a change in potential should be measured. O_2^- is not generally stable species that known amount can be inserted. So another approach for approximate calibration can be made with O_2^- generated with the electron beam. For that optimization code can be used for the objective to maximize the effect of O_2^- ions on an electrode. For measurement of O_2^-, basic pH solutions are recommended because simulation shows generation of O_2^- is higher at those pH. Other than that dose rate to measure O_2^- is recommended to be higher than 10^8 Gy/s, so that solution is near saturation with O_2 dissolved gas. This makes interference from O_2 less and measurement of O_2^- more accurate. For basic solutions generation of H_2 is less, so making solution saturated with H_2 can help reducing potential change due to H_2.

- The current pH sensing layer has a maximum error of 0.4 pH for pH measurement. Error due to linearity and hysteresis is the main contributing factor. The reason for hysteresis can be a permanent change in the oxidation state of Iridium oxide. So making stable state oxide can improve this property. Now each manufacturing technique and post-processing on the pH sensing layer generates different surface property of oxide, that ultimately changes chemical and physical property. Generally, micro layer Iridium oxide deposition techniques generate polycrystalline layer. So modeling that is a highly complex task and one needs to improve hysteresis property by empirical data and trial and error method. Here no post-processing technique is used for the Iridium oxide layer, from the literature it is found that conditioning with acid solution may help improve hysteresis. So further investigation can be done on this.

5

A

APPENDIX: LITERATURE REVIEW

A.1. PH ERROR DUE TO TEMPERATURE

Sensitivity of pH sensor is defined as, $\frac{R*T}{n*F}$. R: Universal gas constant, T: Temperature of solution, F: Faraday constant, n: Number of charge transfer by molecule

If pH sensor is calibrated at 25 $^\circ C$, but solution temperature is 5 K more than error is given by: Here pH range of 3-10 is considered, which is within required range of pH for current application. As pH range increases this error increases.

pH	Potential at		Error in pH
	25 $^\circ C$	30 $^\circ C$	
3	236.5053	240.4736	-0.067114094
4	177.379	180.3552	-0.05033557
5	118.2527	120.2368	-0.033557047
6	59.12634	60.11839	-0.016778523
7	0	0	0
8	-59.1263	-60.1184	0.016778523
9	-118.253	-120.237	0.033557047
10	-177.379	-180.355	0.05033557

A.2. Review table for pH sensing

No.	Material	Surface structure / Preparation method	Method	Sensing area	Thickness	Range	Sensitivity	SD/ Accuracy	Drift	Hyste resis	Time (Sec)	Interfering ions	Ref.
1	OsO_2		OCP			2-11	-51.2	15 mV		25 mV		Affected by Oxidizing and reducing agents	[1]
2	IrO_2		OCP			2-10	-59.8	2 mV		25 mV		Sensitive to Cl^- and Br^- and I^-	[1]
		Electro deposited	OCP	>1.5 mm2 *		2-12	-78.8	r=0.999				Affected by redox solution	[2]
		Anodic IROF	OCP	0.28 cm2,	0.2 um	2-12	-75						[3]
		Sputtered IROF	OCP	0.28 cm2,	0.15 um	2-12	-60.5						[3]
		Sputtered	ISFET	0.0075 mm2	100 nm	2-10	-59.4	r=0.999	0.68 mV/Hr				[4]
		Monocrystalline	OCP				-69 to -74					Affected by redox solution, O_2	[5]
		Anodic IROF	OCP			2.5-8.5	-62 to -68					Not affected by common ligands except bicarbonate, slightly affected by Oxalate. Affected by redox solution, O_2	[5]
		Sputtered resistivity: 1e2 ohm_cm	OCP				-58 to -59		0.36 mV/Hr			Oxidant interference:1-1.5 pH, Reductant int.: 1.7-3.4	[6]
		+Ta2O5 resistivity: 5e12 ohm_cm	OCP			2-12	-58 to -59		0.24 mV/Hr			Oxidant interferance:0.3-0.6 pH, Reductant int.: 0.02-0.05 pH	[6]
		Ta_2O_5 film on IrO_2,Sputtered	OCP	<0.8 mm2	77 nm, 647nm	2-13	-59.4 to -59.5	r=0.999	<0.1 mV/Hr		15 Max.	Selectivity : K+, Na+, Li+: -12.4	[7]
		Anodic IROF	OCP	0.196 mm2		3-12	-69	r=0.999				Sensitive to Cl-, O2,N2: Max 0.9 mV change	[8]
		Sputtered	OCP	0.01 mm2		4-10	-65.9	r=0.9083	<0.004 mV/Hr		<3		[9]
3	RuO_2		OCP			2-12	-61.8	2 mV		9 mV		Sensitive to I-	[1]
		Reactively sputtered	OCP		<1 um	2-12	-54 to -60		2.75 mV/pH	<40 mV			[10]
		Screen printing	Chemi resistor	247 mm2	10 um	2-12							[11]
		+ TiO2 (30%), screen printed	Chemi resistor	221 mm2	10 um	4-11						Li+, Ni+, K+ affects <15 mV	[12]
		+ TiO2 (30%), Screen printed	OCP	100 mm2	10 um	2-12	-56.11	r=0.999	3% initially	5 mV	15	Li+, Ni+, K+ affects <15 mV	[12]
		Pt doped, sintering	OCP	60 mm2		2-13	-58		0.41 mV/Hr		1-2	Sensitive to O2-	[13]
4	RhO_2		OCP			2-12	-68.2	1 mV		20 mV		Sensitive to Br- and I-	[1]
5	Ta_2O_5	Thermally prepared oxide	OCP			3-10	-49.3	30 mV		50 mV		Sensitive to I- and F-	[1]
		Screen printing	Chemi resistor	234 mm2	8 um	3-12	-						[14]
		Screen printing	OCP	10 mm2	8 um	2-10	-45.92	r=0.972					[14]
		on SiO2, Electron beam evaporation	ISFET		53 nm	2-9	-59.3	r=0.999					[15]
		RF sputtering	EIS(CV)		155 nm	1-10	-56.19	r=0.999		5 mV		Cu+2, Fe+2, Fe+3 (pH change: 0.23 for 0.1 mM)	[16]
		Atomic Layer Deposition	OCP		3.3 nm	4-9	-53.6		54 mV/Hr				[17]
		Vapour deposited Thin film	ISFET	0.03 mm2	100 nm	1-13	-56 to -57		0.1 - 0.2 mV/Hr	0.2 mV	<0.1	Na+: <1 mV, K+:<1 mV	[18]
		Sputtered resistivity: 1e14 ohm_cm	OCP						large				[6]
6	SnO_2		OCP				-46.6	65 mV		75 mV			[1]
		on Al/ Corning Glass, Sputtering	ExGFET		300 nm	4-10	-46						[19]
		on Al/ Micro side glass,Sputtering	ExGFET		300 nm	4-10	-54						[19]
		on ITO glass, Sputtering	ExGFET	>4 mm2			-57		0.5 mV/Hr				[19]
		on glass, Sputtering	ExGFET				-55		1.88 mV/Hr				[19]
		on ITO glass, Sputtering	OCP	4 mm2	200 nm	2-12	-59.17	r=0.999			0,1		[20]
		With 30% RuO2, Screen printing	Chemi resistor	Several hundred mm2 *		3-11	-					Li+, Ni+, K+ no significant effect	[21]
		With 30% RuO2, Screen printing	OCP	Several mm2 *		2-12	-56.5			7 mV	5-9	Li+, Ni+, K+ no significant effect	[21]
		on SiO2, thermal evaporation	ISFET	0.05 mm2	150 nm	2-10	-58		0.23 mV/Hr	2.7 mV	<0.1		[22]
		Screen printed	Chemi resistor	Several mm2 *	10 um	2-7				Large			[23]
7	Sb/ Sb_2O_3	Powdered	OCP	>several mm2*		1-10		0.14 mV	0.25 mV/Hr		Large	Oxygen affects its potential	[24]
		Monocrystalline	OCP	several hunderd mm2*		2-10	-52	0.3 mV				Sensitive to complexing agents. Affected by redox solution, O2	[5]
8	Ir/ IrO_2	Thermally prepared oxide	OCP	>15 mm2		2-9	-67		<0.041 mV/day		Max: 30		[24]

No.	Material	Surface structure / Preparation method	Method	Sensing area	Thickness	Range	Sensitivity mV/pH	SD/ Accuracy	Drift	Hysteresis	Time (Sec)	Interfering ions	Ref.
9	Pd/PdO	Thermally prepared oxide	OCP			2.5-8.2	-59.6		0.41 mV/Hr		<10	Not affected by common ligands except for bicarbonate. Affected by redox solution, O2	[5]
10	PtO_2		OCP			5-10	-46.7	4 mV		100 mV		Sensitive to I- and H2O2	[1]
		Reactively sputtered	OCP		0.6 um	5-10	-50		9.1 mV/pH	>250 mV			[10]
		Nano porous, Electro deposited	OCP	>3.1 mm2 *		2-12	-55	r=0.999			<60	Small shift: NaCl, LiCl, KCl. Some shift: NH4Cl, Affected by redox	[2]
		Nano porous + Polyphenol, Electrodeposited	OCP	>3.1 mm2 *		2-12	-44	r=0.997				Film reduces affect of Redox	[2]
			OCP			5-10	-46.7	r=0.976		100 mV	>5000	Severely affected by redox couple	[2]
11	TiO_2		OCP			2-12	-55	15 mV		30 mV		Non reproducible effects with H2O2	[1]
		on Alumina., Screen printing	Chemi resistor	221 mm2	10 um *	4-10		Error: 3%					[25]
		5.5 nm dia TiO2 + multiwall CNT	Chemi resistor			2-12	0.44 uA/pH						[26]
		Sputtered	ISFET		25 nm	1-13	-56.2						[27]
		RF sputtering	ISFET	<0.36 cm2	25.6 nm	1-13	-56.2						[28]
		Electrochemical anodization	OCP			2-12	-59	r=0.999			<30	(Na+, K+, Cl-, NO3-,F-)in range 1e-11, (SO4-, I)in range of 1e-10	[29]
		MOCVD	EIS(CV)		80 nm	3-11	-57.4 to -62.3		-0.038 mV/Hr	27 mV		Light interferance: 20 - 200 mV	[30]
		sol–gel spin coating	ExGFET	4 mm2		1-11	-58.73	r= 0.991	3.64 mV/Hr		40		[31]
		Ru doped, Co sputtering	ExGFET	0.25 cm2	48.3 nm	1-13	-55.2	r=0.999	0.745 mV/Hr				[32]
		nano particles , Layer by layer				4-10	-57	r= 0.997	Several mV/Hr				[33]
		Gd2Ti2O7: Reactive co sputtring	EIS(CV)		40 nm	2-12	-58.31		0.38 mV/Hr	2.9 mV			[34]
		Er2TiO5: Reactive co sputtering	EIS(CV)		40 nm	2-12	-56.6		0.29 mV/Hr	2 mV			[34]
		Lu2Ti2O7: Reactive co sputtering	EIS(CV)		40 nm	2-12	-59.32		0.55 mV/Hr	5.2 mV			[34]
12	PdO	Reactively sputtered	OCP		0.5 um	2-9	-46		10.25 mV/pH	<20 mV			[10]
		Reactive electron beam evaporation	ExGFET	0.25 cm2	130 nm	2-12	-62.87	r= 0.999	2.32 mV/Hr	7.9 mV			[35]
13	Pt	Physical vapor deposition	potentio metric	<1 mm2	100 nm	4-10	-	r= 0.952					[36]
			CV			7.2-7.6	-49 to -76						[37]
14	ZnO	on Silicon nano rod, Atomic layer deposition	ExGFET	4 mm2	50 nm	1-13	-46.25	r= 0.990		9.7 mV			[38]
		nanorod with 80 nm diameter	OCP			4-11	-51.88						[39]
		nano particles	SAW			2-7	-						[40]
		RF sputtering and annealing	EIS(CV)		50 nm	2-12	-42	Max 97%	2.64 mV/Hr	35.1 mV		Na+: 5.74 mV/pNa, K+: 7.33mV/pK	[41]
		amorphous, sol gel	ExGFET			2-12	-38						[42]
		Single nano rod	Chemi resistor			2-12	8.5 nS/pH						[43]
15	ITO	on glass	ExGFET	20 mm2 *	120-160 nm	8-10.8	-52.31	r= 0.995				Corrosion of ITO in acids	[44]
		on touch panel film, sputtering	ExGFET	121 mm2	25 nm	3-13	-59.2	r= 0.994	<2%	1.80%	1	Slightely Sensitive to Na+	[45]
		on PET, RF sputtering	ExGFET	12.5 mm2		2-12	-50.1	r= 0.998	13.2 mV/Hr				[46]
		on glass, Sputtering	ExGFET	>0.8 mm2	23 nm	2-12	-58		6.11 mV/Hr	9.8 mV			[19]
		on glass (70-100 ohm/sq)	Impedance	50 mm2		3-8	400 o/pH	r=0.95					[47]
16	Si_3N_4	on SiO2, thermal evaporation	ISFET	0.05 mm2	Several nm		-49						[22]
		Plasma Treated on SiO2	ISFET		60 - 110 nm	4-10	-45.3							[48]
		Vapour deposited Thin film	ISFET	0.03 mm2	100 nm	1-13	-46 to -56		10 mV/Hr	30 mV	<0.1	Na+: 5-20-50 mV, K+:5-25 mV	[18]
17	SiO_2	Flower like nano wires	Soln. R			2-12							[49]
			ISFET		29 nm	3-12	-258	98.80%	13.34 mV/Hr	54.49 mV			[50]
		Vapour deposited Thin film	ISFET	0.03 mm2	100 nm	4-10	-25 to -35		Un stable		1	Na+: 30-50 mV, K+:20-30 mV	[18]
18	Al_2O_3	RF Sputtered and Anodic oxidation	ExGFET	9 mm2	1 um	4-10	-56		4.5 mV/Hr	3.75 mV			[51]
		Atomic Layer Deposition	OCP		2.5 nm	4-9	-36.4		43 mV/Hr				[17]
		Vapour deposited Thin film	ISFET	0.03 mm2	100 nm	1-13	-53 to -57		0.2 mV/Hr	8 mV	<0.1	Na+: 2 mV, K+: 2 mV	[18]
19	TiN	Sputtered	ExGFET		50 nm	4-10	-59.82						[52]
20	InN	Molecular beam epitaxy	ISFET		100 nm	4-12	-52.04					Selectivity Na: -7.62, K:-7.901	[53]
21	NiO	Sputtered	OCP		355 nm	1-13	-63.37	r= 0.989	-4 mV/Hr	4 mV			[54]
		Nano porous	OCP			2-12	-43.74				<10		[55]

A

No.	Material	Surface structure/ Preparation method	Method	Sensing area	Thick ness	Range	Sensitivity mV/pH	SD/ Accuracy	Drift	Hyste resis	Time (Sec)	Interfering ions	Ref.
22	Zr/ZrO_2	Thin film of ZrO2 on Zr, chemically prepared	OCP		20 um	1-8	-58.22	r= 0.997					[56]
23	ZrO_2	DC Sputtering	ISFET			1-13	-56.7 to -58.3		0.831 mV/Hr				Sensitivity Slightely affected by NaCl	[57]
24	Ta_2O_5: RuO_2	10.5 : 31.2 %	OCP			1-12	-55.5 to -58.6						Negligible effect of Cl-	[58]
		15 : 15.1 %	OCP			1-12	-56.5 to -58						Negligible effect of Cl-	[58]
		8.6 : 26.2 %	OCP			1-12	-57.5 to -58.9						Negligible effect of Cl-	[58]
25	Gd_2O_3	(resistivity: 5-10 ohm_cm) Polycrystaline, RF sputtering	EIS(CV)		40 nm	2-12	-59.63	r= 0.999	0.6 mV/Hr				[59]
26	AlN	nanocrystalline , sputtered	ISFET		20 nm	4-10	-43.33					225		[60]
		nanocrystalline , sputtered	ISFET		40 nm	4-10	-45					225		[60]
		nanocrystalline , sputtered	ISFET		80 nm	4-10	-54.5					300		[60]
27	CuO	Nanoflowers	OCP			2-11	-28		150 mV/Hr			25		[61]
28	Co_3O_4	nanostructures grown by hydrothermal method	OCP			3-13	-58.45					53		[62]
29	WO_3	Electrodeposited nano particles,Wax printing	OCP	1 mm2		9-5	-56.7	r= 0.995				28		[63]
		Sputtring deposition (Resistivity: 13-33 mu_ohm_cm)	OCP	0.0019 mm2		2-12	-55		6 mV/Hr	50 mV		<28		[64]
30	Diamond	Boron doped HFCVD	OCP	94.2 um2		2-12	-50.8	r= 0.997				<1		[65]
		Boron doped MPCVD	chrono potentio metric	0.283 cm2	40 um	1-6							Influnced by active electrochemical couple	[66]
		Boron doped MPCVD	OCP	0.283 cm2	40 um	1-12	-53.6						Na+, K+ has no effect, Influnced by active electrochemical couple	[66]
31	Poly bisphenol	On ITO electrochemically synthesized	OCP			-1-15	-56.7	0.12 pH				<20	No significant effectNa+,K+,Clor SO42of 2.0 mol L1	[67]
		On ITO electrochemically synthesized	Redox peak potential			-1-12	-58.6	0.18 pH					No significant effectNa+,K+,Clor SO42of 2.0 mol L1	[67]
32	polyethyl eneimine (PEI)	Electropolymerization on Pt	OCP	0.785 mm2		2-11	-46	r= 0.9967				15	Sensitivity decreases considerably with time, not stable over 1 month, can not be used for several measurement	[42]
33	polypropyl eneimine (PPI)	Electropolymerization on Pt	OCP	0.785 mm2		2-11	-43	r= 0.9937				15	Sensitivity doesnot decreases too much over one month	[42]
34	polypyrrole (Ppy)	Electropolymerization on Pt	OCP	0.785 mm2		2-11	-48	r= 0.9966				120	Sensitivity decreases considerably with time, not stable over 1 month, can not be used for several measurement	[42]
35	(p-phenyl enediamine) (PPPD)	Electropolymerization on Pt	OCP	0.785 mm2		2-11	-34	r= 0.9950				60	Sensitivity doesnot decreases too much over one month	[42]
36	polyaniline (PANI)	Electropolymerization on Pt	OCP	0.785 mm2		2-9	-52	r= 0.9573				60	Sensitivity decreases considerably with time, not stable over 1 month, can not be used for several measurement	[42]

*Area estimated by setup/description

REFERENCES

[1] A. Fog and R. P. Buck, "Electronic semiconducting oxides as ph sensors," *Sensors and Actuators*, vol. 5, no. 2, pp. 137 – 146, 1984.

[2] S. Park, H. Boo, Y. Kim, J.-H. Han, H. C. Kim, and T. D. Chung, "ph-sensitive solid-state electrode based on electrodeposited nanoporous platinum," *Analytical Chemistry*, vol. 77, no. 23, pp. 7695–7701, 2005.

[3] M. Yuen, I. Lauks, and W. Dautremont-Smith, "ph dependent voltammetry of iridium oxide films," *Solid State Ionics*, vol. 11, no. 1, pp. 19 – 29, 1983.

[4] J. Hendrikse, W. Olthuis, and P. Bergveld, "A method of reducing oxygen induced drift in iridium oxide ph sensors," *Sensors and Actuators B: Chemical*, vol. 53, no. 1, pp. 97 – 103, 1998.

[5] E. Kinoshita, F. Ingman, G. Edwall, S. Thulin, and S. Głab, "Polycrystalline and monocrystalline antimony, iridium and palladium as electrode material for ph-sensing electrodes," *Talanta*, vol. 33, no. 2, pp. 125 – 134, 1986.

[6] I. Lauks, "5009766 united states patent." http://www.everypatent.com/comp/pat5009766.html, 1991.

[7] L.-M. Kuo, Y.-C. Chou, K.-N. Chen, C.-C. Lu, and S. Chao, "A precise ph microsensor using rf-sputtering iro2 and ta2o5 films on pt-electrode," *Sensors and Actuators B: Chemical*, vol. 193, pp. 687 – 691, 2014.

[8] D. O'Hare, K. H. Parker, and C. P. Winlove, "Metal–metal oxide ph sensors for physiological application," *Medical Engineering Physics*, vol. 28, no. 10, pp. 982 – 988, 2006. Developments in Biosensors: New Structural Designs for Functional Interfaces.

[9] M. A. G. Zevenbergen, G. Altena, V. A. T. Dam, M. Goedbloed, P. Bembnowicz, P. McGuinness, H. Berney, A. Berduque, T. O'Dwyer, and R. van Schaijk, "Solid state ph and chloride sensor with microfluidic reference electrode," in *2016 IEEE International Electron Devices Meeting (IEDM)*, pp. 26.1.1–26.1.4, Dec 2016.

[10] K. G. Kreider, M. J. Tarlov, and J. P. Cline, "Sputtered thin-film ph electrodes of platinum, palladium, ruthenium, and iridium oxides," *Sensors and Actuators B: Chemical*, vol. 28, no. 3, pp. 167 – 172, 1995.

[11] L. Manjakkal, E. Djurdjic, K. Cvejin, J. Kulawik, K. Zaraska, and D. Szwagierczak, "Electrochemical impedance spectroscopic analysis of ruo2 based thick film ph sensors," *Electrochimica Acta*, vol. 168, pp. 246 – 255, 2015.

[12] L. Manjakkal, K. Cvejin, J. Kulawik, K. Zaraska, D. Szwagierczak, and R. P. Socha, "Fabrication of thick film sensitive ruo2-tio2 and ag/agcl/kcl reference electrodes and their application for ph measurements," *Sensors and Actuators B: Chemical*, vol. 204, pp. 57 – 67, 2014.

[13] S. Zhuiykov, "Morphology of pt-doped nanofabricated ruo2 sensing electrodes and their properties in water quality monitoring sensors," *Sensors and Actuators B: Chemical*, vol. 136, no. 1, pp. 248 – 256, 2009.

[14] L. Manjakkal, K. Cvejin, B. Bajac, J. Kulawik, K. Zaraska, and D. Szwagierczak, "Microstructural, impedance spectroscopic and potentiometric analysis of ta2o5 electrochemical thick film ph sensors," *Electroanalysis*, vol. 27, no. 3, pp. 770–781, 2015.

[15] P. Gimmel, B. Gompf, D. Schmeisser, H. Wiemhöfer, W. Göpel, and M. Klein, "Ta2o5-gates of ph-sensitive devices: Comparative spectroscopic and electrical studies," *Sensors and Actuators*, vol. 17, no. 1, pp. 195 – 202, 1989.

[16] M. Chen, Y. Jin, X. Qu, Q. Jin, and J. Zhao, "Electrochemical impedance spectroscopy study of ta2o5 based eios ph sensors in acid environment," *Sensors and Actuators B: Chemical*, vol. 192, pp. 399 – 405, 2014.

[17] E. Nycander, "Evaluation of ald oxides as the sensing layer for ion sensors," 2016.

[18] T. Matsuo and M. Esashi, "Methods of isfet fabrication," *Sensors and Actuators*, vol. 1, pp. 77 – 96, 1981.

A

[19] L.-T. Yin, J.-C. Chou, W.-Y. Chung, T.-P. Sun, and S.-K. Hsiung, "Separate structure extended gate h+-ion sensitive field effect transistor on a glass substrate," *Sensors and Actuators B: Chemical*, vol. 71, no. 1, pp. 106 – 111, 2000.

[20] C.-W. Pan, J.-C. Chou, T.-P. Sun, and S.-K. Hsiung, "Development of the tin oxide ph electrode by the sputtering method," *Sensors and Actuators B: Chemical*, vol. 108, no. 1, pp. 863 – 869, 2005. Proceedings of the Tenth International Meeting on Chemical Sensors.

[21] K. Arshak, E. Gill, A. Arshak, and O. Korostynska, "Investigation of tin oxides as sensing layers in conductimetric interdigitated ph sensors," *Sensors and Actuators B: Chemical*, vol. 127, no. 1, pp. 42 – 53, 2007. Special Issue: Eurosensors XX The 20th European Conference on Solid-State Transducers.

[22] H.-K. Liao, J.-C. Chou, W.-Y. Chung, T.-P. Sun, and S.-K. Hsiung, "Study of amorphous tin oxide thin films for isfet applications," *Sensors and Actuators B: Chemical*, vol. 50, no. 2, pp. 104 – 109, 1998.

[23] K. Arshak, E. Gill, A. Arshak, and O. Korostynska, "Investigation of tin oxides as sensing layers in conductimetric interdigitated ph sensors," *Sensors and Actuators B: Chemical*, vol. 127, no. 1, pp. 42 – 53, 2007. Special Issue: Eurosensors XX The 20th European Conference on Solid-State Transducers.

[24] S. Głab, A. Hulanicki, G. Edwall, and F. Ingman, "Metal-metal oxide and metal oxide electrodes as ph sensors," *Critical Reviews in Analytical Chemistry*, vol. 21, no. 1, pp. 29–47, 1989.

[25] M. Simić, L. Manjakkal, K. Zaraska, G. M. Stojanović, and R. Dahiya, "Tio2-based thick film ph sensor," *IEEE Sensors Journal*, vol. 17, pp. 248–255, Jan 2017.

[26] Y. Chen, S. C. Mun, and J. Kim, "A wide range conductometric ph sensor made with titanium dioxide/multiwall carbon nanotube/cellulose hybrid nanocomposite," *IEEE Sensors Journal*, vol. 13, pp. 4157–4162, Nov 2013.

[27] J. C. Chou and L. P. Liao, "Study of TiO2thin films for ion sensitive field effect transistor application with RF sputtering deposition," *Japanese Journal of Applied Physics*, vol. 43, pp. 61–65, jan 2004.

[28] J. C. Chou and L. P. Liao, "Study of TiO_2 Thin Films for Ion Sensitive Field Effect Transistor Application with RF Sputtering Deposition," *Japanese Journal of Applied Physics*, vol. 43, p. 61, Jan 2004.

[29] R. Zhao, M. Xu, J. Wang, and G. Chen, "A ph sensor based on the tio2 nanotube array modified ti electrode," *Electrochimica Acta*, vol. 55, no. 20, pp. 5647 – 5651, 2010.

[30] P.-K. Shin, "The ph-sensing and light-induced drift properties of titanium dioxide thin films deposited by mocvd," *Applied Surface Science*, vol. 214, no. 1, pp. 214 – 221, 2003.

[31] Y.-H. Liao and J.-C. Chou, "Preparation and characterization of the titanium dioxide thin films used for ph electrode and procaine drug sensor by sol–gel method," *Materials Chemistry and Physics*, vol. 114, no. 2, pp. 542 – 548, 2009.

[32] J. Chou and C. Chen, "Fabrication and application of ruthenium-doped titanium dioxide films as electrode material for ion-sensitive extended-gate fets," *IEEE Sensors Journal*, vol. 9, pp. 277–284, March 2009.

[33] N. C. Vieira, A. Figueiredo, A. D. Faceto, A. A. de Queiroz, V. Zucolotto, and F. E. Guimarães, "Dendrimers/tio2 nanoparticles layer-by-layer films as extended gate fet for ph detection," *Sensors and Actuators B: Chemical*, vol. 169, pp. 397 – 400, 2012.

[34] T.-M. Pan, P.-Y. Liao, K.-Y. Chang, and L. Chi, "Structural and sensing characteristics of gd2ti2o7, er2tio5 and lu2ti2o7 sensing membrane electrolyte–insulator–semiconductor for bio-sensing applications," *Electrochimica Acta*, vol. 89, pp. 798 – 806, 2013.

[35] A. Das, D. H. Ko, C.-H. Chen, L.-B. Chang, C.-S. Lai, F.-C. Chu, L. Chow, and R.-M. Lin, "Highly sensitive palladium oxide thin film extended gate fets as ph sensor," *Sensors and Actuators B: Chemical*, vol. 205, pp. 199 – 205, 2014.

[36] W.-C. Lin, K. Brondum, C. W. Monroe, and M. A. Burns, "Multifunctional water sensors for ph, orp, and conductivity using only microfabricated platinum electrodes," *Sensors*, vol. 17, no. 7, 2017.

[37] N. J. Finnerty and F. B. Bolger, "A platinum oxide-based microvoltammetric ph electrode suitable for physiological investigations," *Analyst*, vol. 143, pp. 3124–3133, 2018.

[38] H.-H. Li, C.-E. Yang, C.-C. Kei, C.-Y. Su, W.-S. Dai, J.-K. Tseng, P.-Y. Yang, J.-C. Chou, and H.-C. Cheng, "Coaxial-structured zno/silicon nanowires extended-gate field-effect transistor as ph sensor," *Thin Solid Films*, vol. 529, pp. 173 – 176, 2013. TACT2011 International Thin Films Conference.

[39] M. Willander and S. Al-Hilli, *ZnO Nanorods as an Intracellular Sensor for pH Measurements*, pp. 187–200. Totowa, NJ: Humana Press, 2009.

[40] H. Oh, K. J. Lee, J. Baek, S. S. Yang, and K. Lee, "Development of a high sensitive ph sensor based on shear horizontal surface acoustic wave with zno nanoparticles," *Microelectronic Engineering*, vol. 111, pp. 154 – 159, 2013.

[41] C. Haur Kao, H. Chen, M. Ling Lee, C. Chun Liu, H.-Y. Ueng, Y. Cheng Chu, Y. Jie Chen, and K. Ming Chang, "Multianalyte biosensor based on ph-sensitive zno electrolyte–insulator–semiconductor structures," *Journal of Applied Physics*, vol. 115, no. 18, p. 184701, 2014.

[42] B. Lakard, G. Herlem, S. Lakard, R. Guyetant, and B. Fahys, "Potentiometric ph sensors based on electrodeposited polymers," *Polymer*, vol. 46, no. 26, pp. 12233 – 12239, 2005.
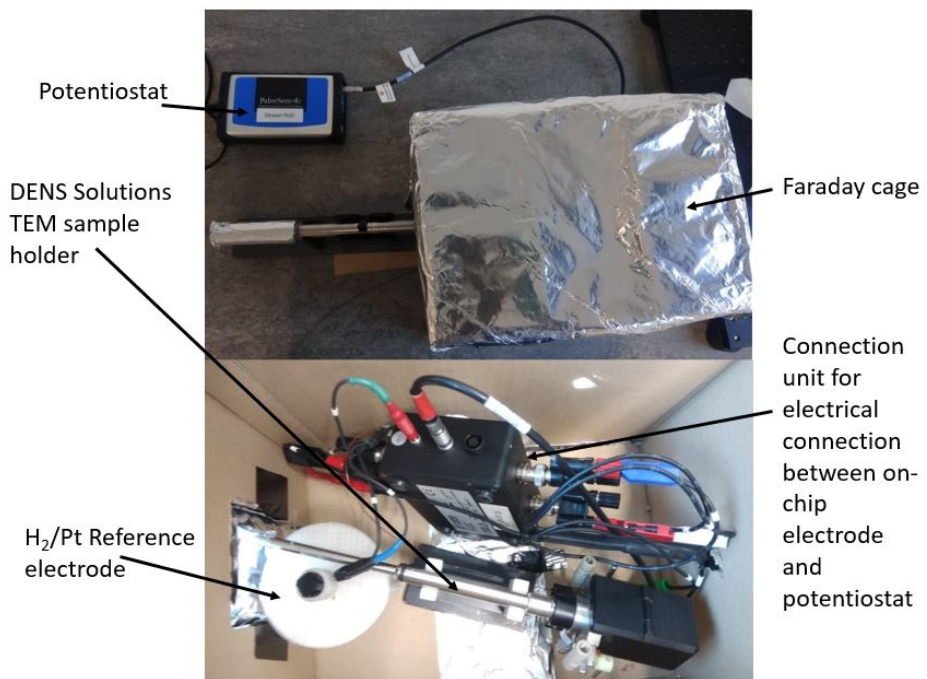
[43] B. S. Kang, F. Ren, Y. W. Heo, L. C. Tien, D. P. Norton, and S. J. Pearton, "ph measurements with single zno nanorods integrated with a microchannel," *Applied Physics Letters*, vol. 86, no. 11, p. 112105, 2005.

[44] N. Mokhtarifar, F. Goldschmidtboeing, and P. Woias, "Ito/glass as extended-gate of fet: A low-cost method for differential ph-sensing in alkaline solutions," *Journal of The Electrochemical Society*, vol. 166, no. 12, pp. B896–B902, 2019.

[45] Y. Wu, S. Wu, and C. Lin, "High performance egfet-based ph sensor utilizing low-cost industrial-grade touch panel film as the gate structure," *IEEE Sensors Journal*, vol. 15, pp. 6279–6286, Nov 2015.

[46] C.-E. Lue, I.-S. Wang, C.-H. Huang, Y.-T. Shiao, H.-C. Wang, C.-M. Yang, S.-H. Hsu, C.-Y. Chang, W. Wang, and C.-S. Lai, "ph sensing reliability of flexible ito/pet electrodes on egfets prepared by a roll-to-roll process," *Microelectronics Reliability*, vol. 52, no. 8, pp. 1651 – 1654, 2012. ICMAT 2011 - Reliability and variability of semiconductor devices and ICs.

[47] L. Folkertsma, L. Gehrenkemper, J. Eijkel, K. Gerritsen, and M. Odijk, "Reference-electrode free ph sensing using impedance spectroscopy," *Proceedings*, vol. 2, p. 742, Nov 2018.

[48] Li-Te Yin, Jung-Chuan Chou, Wen-Yaw Chung, Tai-Ping Sun, and Shen-Ken Hsiung, "Characteristics of silicon nitride after o/sub 2/ plasma surface treatment for ph-isfet applications," *IEEE Transactions on Biomedical Engineering*, vol. 48, pp. 340–344, March 2001.

[49] Q. Shao, R. hui Que, M. wang Shao, Q. Zhou, D. D. D. Ma, and S.-T. Lee, "Shape controlled flower-like silicon oxide nanowires and their ph response," *Applied Surface Science*, vol. 257, no. 13, pp. 5559 – 5562, 2011.

[50] J.-K. Park, H.-J. Jang, J.-T. Park, and W.-J. Cho, "Soi dual-gate isfet with variable oxide capacitance and channel thickness," *Solid-State Electronics*, vol. 97, pp. 2 – 7, 2014. Selected papers from EuroSOI 2013.

[51] J.-L. Lin, Y.-M. Chu, S.-H. Hsaio, Y.-L. Chin, and T.-P. Sun, "Structures of anodized aluminum oxide extended-gate field-effect transistors on pH sensors," *Japanese Journal of Applied Physics*, vol. 45, pp. 7999–8004, oct 2006.

[52] Y. Rayanasukha, S. Porntheeraphat, W. Bunjongpru, N. Khemasiri, A. Pankiew, W. Jeamsaksiri, A. Srisuwan, W. Chaisriratanakul, C. Hruanun, A. Poyai, and J. Nukeaw, "High sensitive nanocrystal titanium nitride eg-fet ph sensor," in *Advances in Material Science and Technology*, vol. 802 of *Advanced Materials Research*, pp. 232–236, Trans Tech Publications Ltd, 12 2013.

[53] C.-T. Lee, Y.-S. Chiu, and X.-Q. Wang, "Performance enhancement mechanisms of passivated inn/gan-heterostructured ion-selective field-effect-transistor ph sensors," *Sensors and Actuators B: Chemical*, vol. 181, pp. 810 – 815, 2013.

A

[54] J. Chou, S. Yan, Y. Liao, C. Lai, J. Chen, H. Chen, T. Tseng, and T. Wu, "Characterization of flexible arrayed ph sensor based on nickel oxide films," *IEEE Sensors Journal*, vol. 18, pp. 605–612, Jan 2018.

[55] Z. H. Ibupoto, K. Khun, and M. Willander, "Development of a ph sensor using nanoporous nanostructures of nio," *Journal of Nanoscience and Nanotechnology*, vol. 14, no. 9, pp. 6699–6703, 2014.

[56] R. Zhang, X. Zhang, and S. Hu, "Zr/zro2 sensors for in situ measurement of ph in high-temperature and -pressure aqueous solutions," *Analytical Chemistry*, vol. 80, no. 8, pp. 2982–2987, 2008.

[57] K.-M. Chang, K.-Y. Chao, T.-W. Chou, and C.-T. Chang, "Characteristics of zirconium oxide gate ion-sensitive field-effect transistors," *Japanese Journal of Applied Physics*, vol. 46, pp. 4333–4337, jul 2007.

[58] C. Miao and V. Mikko, "2015227394 al, australian patent." https://worldwide.espacenet.com/publicationDetails/biblio?FT=D&date=20180425&DB=&locale=en_EP&CC=EP&NR=3189327A4&KC=A4&ND=1, 2015.

[59] J. Her, M.-H. Wu, Y.-B. Peng, T.-M. Pan, W.-H. Weng, S.-T. Pang, and L. Chi, "High performance gdtixoy electrolyte-insulator-semiconductor ph sensor and biosensor," *International Journal of Electrochemical Science*, vol. 8, pp. 606–620, 01 2013.

[60] W. Bunjongpru, S. Porntheeraphat, O. Trithaveesak, N. Somwang, P. Khomdet, W. Jeamsaksiri, C. Hruanun, A. Poyai, and J. Nukeaw, "The innovative aln-isfet based ph sensor," in *2008 5th International Conference on Electrical Engineering/Electronics, Computer, Telecommunications and Information Technology*, vol. 2, pp. 833–836, May 2008.

[61] S. Zaman, M. Asif, A. Zainelabdin, G. Amin, O. Nur, and M. Willander, "Cuo nanoflowers as an electrochemical ph sensor and the effect of ph on the growth," *Journal of Electroanalytical Chemistry*, vol. 662, no. 2, pp. 421 – 425, 2011.

[62] M. Hussain, Z. H. Ibupoto, M. A. Abbasi, O. Nur, and M. Willander, "Effect of anions on the morphology of co3o4 nanostructures grown by hydrothermal method and their ph sensing application," *Journal of Electroanalytical Chemistry*, vol. 717-718, pp. 78 – 82, 2014.

[63] L. Santos, J. P. Neto, A. Crespo, D. Nunes, N. Costa, I. M. Fonseca, P. Barquinha, L. Pereira, J. Silva, R. Martins, and E. Fortunato, "Wo3 nanoparticle-based conformable ph sensor," *ACS Applied Materials & Interfaces*, vol. 6, no. 15, pp. 12226–12234, 2014.

[64] A. Lale, A. Tsopela, A. Civélas, L. Salvagnac, J. Launay, and P. Temple-Boyer, "Integration of tungsten layers for the mass fabrication of wo3-based ph-sensitive potentiometric microsensors," *Sensors and Actuators B: Chemical*, vol. 206, pp. 152 – 158, 2015.

A

A

[65] E. Silva, A. Bastos, M. Neto, R. Silva, M. Ferreira, M. Zheludkevich, and F. Oliveira, "Novel diamond microelectrode for ph sensing," *Electrochemistry Communications*, vol. 40, pp. 31 – 34, 2014.

[66] S. Fierro, N. Mitani, C. Comninellis, and Y. Einaga, "ph sensing using boron doped diamond electrodes," *Phys. Chem. Chem. Phys.*, vol. 13, pp. 16795–16799, 2011.

[67] Q. Li, H. Li, J. Zhang, and Z. Xu, "A novel ph potentiometric sensor based on electrochemically synthesized polybisphenol a films at an ito electrode," *Sensors and Actuators B: Chemical*, vol. 155, no. 2, pp. 730 – 736, 2011.

B

APPENDIX: EXPERIMENTAL SETUP

C

APPENDIX: RADIOLYSIS SIMULATION

C.1. COMSOL 2D MODEL SETUP

COMSOL radiolysis model is setup in chemistry and transport of diluted species module. In the chemistry module, 73 reactions are defined for 16 species. In the transport of diluted species, diffusion coefficients and generation of species are defined.

C.2. MATLAB OPTIMIZATION

Files Hi.txt, O2i.txt, H2O2.txt and OH.txt is input from 1D axis symmetry COMSOL simulation. These files represents concentration of respective species with distance from center of beam.

```matlab
clc;
clear;
close;

%Fmincon function for optimization
xq=[1 3 5 10]; %Coordinates in Micron
options = optimoptions('fmincon','OptimalityTolerance',1e-7,'MaxFunctionEvaluations',↙
50000,'ConstraintTolerance',1e-7,'FunctionTolerance',1e-7,'OptimalityTolerance',1e-7);
[x,fval,exitflag,output,lambda] = fmincon('Objectivefunction',xq,[],[],[],[],[],↙
[],'Constraints',options)
```

```matlab
function f=Objectivefunction(xq)
x1=xq(1);
x2=xq(2);
x3=xq(3);
x4=xq(4);
%Concentration in Molar
Hi=load('Hi.txt');
P=griddedInterpolant(Hi(:,1),Hi(:,2));
CHi=@(t) P(t);
O2i=load('O2i.txt');
Q=griddedInterpolant(O2i(:,1),O2i(:,2));
CO2i=@(t) Q(t);
H2O2=load('H2O2.txt');
R=griddedInterpolant(H2O2(:,1),H2O2(:,2));
CH2O2=@(t) R(t);
OH=load('OH.txt');
S=griddedInterpolant(OH(:,1),OH(:,2));
COH=@(t) S(t);

we=((integral(CHi,x1,x2))-(integral(CO2i,x1,x2))-(1e-4*integral(CH2O2,x1,x2))-(integral↙
(COH,x1,x2)))/(x2-x1);
re=((integral(CHi,x3,x4))-(integral(CO2i,x3,x4))-(1e-4*integral(CH2O2,x3,x4))-(integral↙
(COH,x3,x4)))/(x4-x3);

f=(-we+re)*1e6;
```

C

```matlab
%Constraints
function [gc,geq] = Constraints(xq)
x1=xq(1);
x2=xq(2);
x3=xq(3);
x4=xq(4);


gc(1)=2-x3+x2;  %2um distance because of feature size
gc(2)=x3-x4+2;  %2um distance because of feature size
gc(3)=x4-100;
gc(4)=2-x2+x1;  %2um distance because of feature size
gc(5)=1-x1;     %1um distance from center of beam

geq(1)=(x2^2-x1^2)-(x4^2-x3^2);  %Both electrode should have same area to reduce drift


end
```
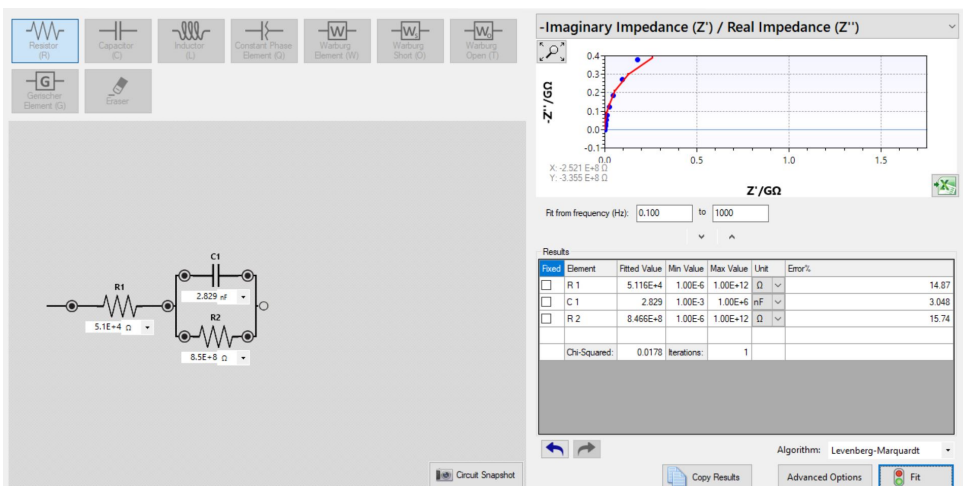
C

APPENDIX: RESULTS

D.1. IMPEDANCE ANALYSIS CIRCUIT FITTING

Software from potentiostat (Palmsens 4), is used to estimate fitting parameters for equivalent electric circuit.

D.2. Species selection table

Concentration of radiolysis product average over WE from 3.5 μm beam near electrode (WE). Highlighted cells are concentration greater than 0.1 times concentration of H^+ ions.

D (W/kg)	pH	Concentration (M), Hi	Concentration (M), H2	Concentration (M), H2O2	Concentration (M), CO2	Concentration (M), eaq	Concentration (M), H	Concentration (M), HO2	Concentration (M), HO2i	Concentration (M), HO3	Concentration (M), O2i	Concentration (M), O3	Concentration (M), O3i	Concentration (M), OH	Concentration (M), OHi	Concentration (M), Oi
1.E+07	7	2.23E-07	0.00024	0.000201	2.04E-05	1.82E-14	1.1E-12	5.01E-09	2.13E-09	9.86E-17	5.23E-07	6.74E-14	5.68E-15	3.71E-11	4.76E-08	4.43E-16
5.E+07	7	2.73E-07	0.00054	0.000425	5.92E-05	6.67E-14	2.32E-13	1.02E-08	3.84E-09	5.22E-16	7.82E-07	1.25E-13	1.18E-14	9.88E-12	4.05E-08	8.02E-16
1.E+08	7	2.92E-07	0.000764	0.000577	9.61E-05	1.09E-13	1.24E-13	1.34E-08	4.98E-09	1.18E-15	9.01E-07	1.47E-13	1.46E-14	4.87E-12	3.87E-08	1.67E-15
1.E+07	4	0.0001	0.000426	0.000422	4.18E-06	1.24E-14	1.35E-11	1.12E-07	9.47E-12	1.04E-19	3.01E-08	9.06E-18	6.98E-21	4.31E-11	1E-10	5.77E-18
5.E+07	4	0.0001	0.000784	0.000763	1.44E-05	4.59E-14	2.14E-12	1.61E-07	1.71E-11	5.46E-18	4.33E-08	2.36E-16	1.31E-19	1.23E-11	1E-10	6.74E-17
1.E+08	4	0.0001	0.001028	0.000988	2.51E-05	7.79E-14	8.19E-13	1.85E-07	2.22E-11	2.92E-17	4.99E-08	8.71E-16	2.21E-18	6.48E-12	1E-10	1.92E-16
1.E+07	2.45	0.003548	0.001095	0.001101	2.88E-06	1.5E-15	1.46E-11	4.53E-07	6.95E-13	1.51E-24	3.44E-09	6.91E-23	2.57E-25	2.64E-11	2.83E-12	1.37E-20
5.E+07	2.45	0.003548	0.002169	0.002182	6.74E-06	6.66E-15	4.48E-12	7.01E-07	1.38E-12	6.41E-23	5.32E-09	1.02E-21	5.31E-24	8.45E-12	2.83E-12	1.19E-19
1.E+08	2.45	0.003548	0.00287	0.002874	9.48E-06	1.24E-14	2.61E-12	8.27E-07	1.82E-12	3.63E-22	6.27E-09	3.34E-21	3.7E-23	5.07E-12	2.83E-12	5.78E-19

Concentration of radiolysis product average over RE from 3.5 μm beam near electrode (WE). Highlighted cells are concentration greater than 0.1 times concentration of H^+ ions.

D (W/kg)	pH	Concentration (M), Hi	Concentration (M), H2	Concentration (M), H2O2	Concentration (M), CO2	Concentration (M), eaq	Concentration (M), H	Concentration (M), HO2	Concentration (M), HO2i	Concentration (M), HO3	Concentration (M), O2i	Concentration (M), O3	Concentration (M), O3i	Concentration (M), OH	Concentration (M), OHi	Concentration (M), Oi
1.E+07	7	1.94E-07	2.40E-04	2.00E-04	2.06E-05	6.61E-15	4.44E-15	2.68E-09	2.36E-09	1.53E-19	3.50E-07	5.67E-17	1.47E-17	1.08E-13	5.29E-08	5.20E-17
5.E+07	7	2.37E-07	5.40E-04	4.23E-04	5.97E-05	1.52E-14	8.21E-15	4.61E-09	4.18E-09	5.00E-18	4.70E-07	7.34E-17	1.26E-16	2.25E-13	4.42E-08	2.15E-16
1.E+08	7	2.57E-07	7.63E-04	5.74E-04	9.68E-05	2.13E-14	1.58E-14	5.53E-09	5.31E-09	2.48E-17	5.08E-07	7.66E-17	2.75E-16	3.23E-13	4.14E-08	3.71E-16
1.E+07	4	1.00E-04	4.25E-04	4.21E-04	4.26E-06	2.53E-15	9.77E-15	4.55E-08	9.43E-12	8.24E-22	1.22E-08	1.28E-20	7.16E-22	4.54E-14	1.00E-10	4.39E-19
5.E+07	4	1.00E-04	7.83E-04	7.61E-04	1.46E-05	7.85E-15	3.29E-14	5.61E-08	1.70E-11	7.98E-21	1.51E-08	5.26E-19	1.77E-20	2.14E-13	1.00E-10	3.52E-18
1.E+08	4	1.00E-04	1.03E-03	9.85E-04	2.53E-05	1.25E-14	4.27E-14	6.07E-08	2.21E-11	5.51E-20	1.63E-08	1.18E-18	6.59E-20	3.20E-13	1.00E-10	8.08E-18
1.E+07	2.45	3.55E-03	1.09E-03	1.10E-03	2.99E-06	1.78E-16	2.78E-14	2.63E-07	6.93E-13	2.97E-26	1.99E-09	4.16E-26	-1.75E-26	5.34E-14	2.82E-12	-6.27E-22
5.E+07	2.45	3.55E-03	2.17E-03	2.18E-03	6.95E-06	7.88E-16	8.01E-14	3.67E-07	1.37E-12	2.91E-24	2.79E-09	-2.24E-25	-1.03E-25	5.99E-14	2.83E-12	3.42E-22
1.E+08	2.45	3.55E-03	2.87E-03	2.87E-03	9.76E-06	1.47E-15	1.41E-13	4.14E-07	1.81E-12	2.09E-23	3.14E-09	-4.06E-24	-1.08E-24	1.50E-13	2.83E-12	-3.26E-21

Concentration of radiolysis product average over CE from 3.5 μm beam near electrode (WE). Highlighted cells are concentration greater than 0.1 times concentration of H^+ ions.

D (W/kg)	pH	Concentration (M), Hi	Concentration (M), H2	Concentration (M), H2O2	Concentration (M), CO2	Concentration (M), eaq	Concentration (M), H	Concentration (M), HO2	Concentration (M), HO2i	Concentration (M), HO3	Concentration (M), O2i	Concentration (M), O3	Concentration (M), O3i	Concentration (M), OH	Concentration (M), OHi	Concentration (M), Oi
1.E+07	7	1.35E-07	2.40E-04	1.98E-04	2.11E-05	1.08E-23	2.13E-18	2.89E-10	3.28E-09	2.34E-28	5.74E-08	5.79E-28	4.36E-21	9.56E-17	7.42E-08	8.88E-22
5.E+07	7	1.44E-07	5.39E-04	4.18E-04	6.09E-05	1.57E-23	1.76E-18	3.33E-10	6.51E-09	2.76E-27	6.22E-08	2.02E-27	1.18E-20	1.00E-16	6.98E-08	8.75E-22
1.E+08	7	1.48E-07	7.62E-04	5.66E-04	9.86E-05	2.06E-23	1.53E-18	3.48E-10	8.57E-09	2.10E-26	6.31E-08	2.91E-27	1.79E-20	9.91E-17	6.78E-08	8.38E-22
1.E+07	4	1.00E-04	4.24E-04	4.16E-04	4.42E-06	4.06E-24	3.08E-18	2.41E-09	9.31E-12	7.56E-31	6.48E-10	1.42E-28	4.93E-28	2.22E-17	1.00E-10	2.79E-25
5.E+07	4	1.00E-04	7.81E-04	7.52E-04	1.51E-05	7.86E-24	1.84E-18	2.53E-09	1.68E-11	1.24E-29	6.80E-10	3.76E-27	1.62E-27	2.12E-17	1.00E-10	2.69E-25
1.E+08	4	1.00E-04	1.02E-03	9.74E-04	2.63E-05	1.19E-23	1.43E-18	2.57E-09	2.18E-11	8.27E-29	6.91E-10	7.73E-27	2.80E-27	2.08E-17	1.00E-10	2.67E-25
1.E+07	2.45	3.55E-03	1.09E-03	1.09E-03	3.16E-06	3.51E-24	8.03E-17	2.52E-08	6.86E-13	2.72E-35	1.91E-10	2.06E-37	3.53E-30	2.83E-16	2.82E-12	1.00E-25
5.E+07	2.45	3.55E-03	2.16E-03	2.15E-03	7.28E-06	3.73E-24	8.14E-17	2.80E-08	1.36E-12	2.68E-33	2.13E-10	4.66E-37	8.73E-30	3.04E-16	2.82E-12	1.08E-25
1.E+08	2.45	3.55E-03	2.86E-03	2.85E-03	1.02E-05	4.15E-24	8.14E-17	2.90E-08	1.80E-12	1.92E-32	2.20E-10	2.41E-38	1.27E-29	3.11E-16	2.82E-12	1.10E-25

D

D.3. SPECIES CONCENTRATION WITHIN BEAM REGION WITH DOSE RATE AND INITIAL PH

Generation of species from numerical simulation with different electron beam dose rate and initial pH of solution.
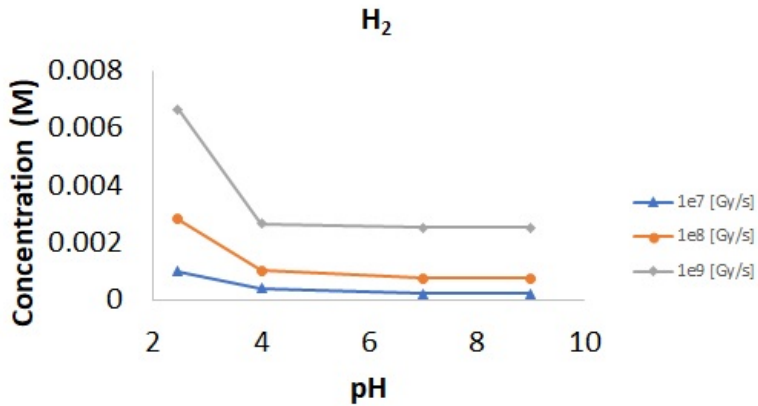

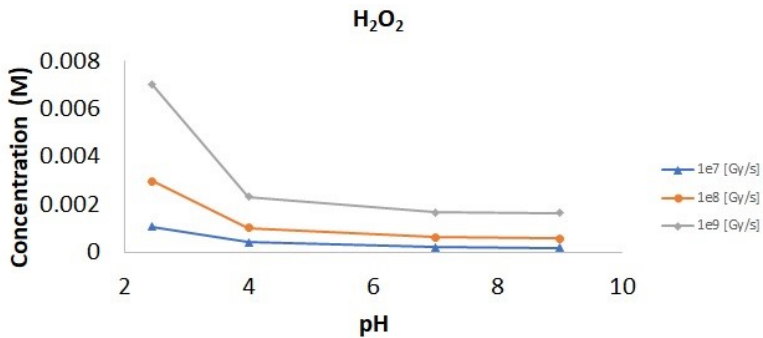Figure D.1: Concentration of H_2 with different dose rate and initial pH of solution

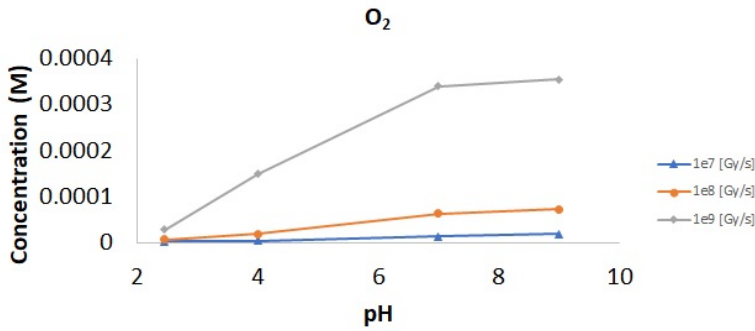Figure D.2: Concentration of H_2O_2 with different dose rate and initial pH of solution

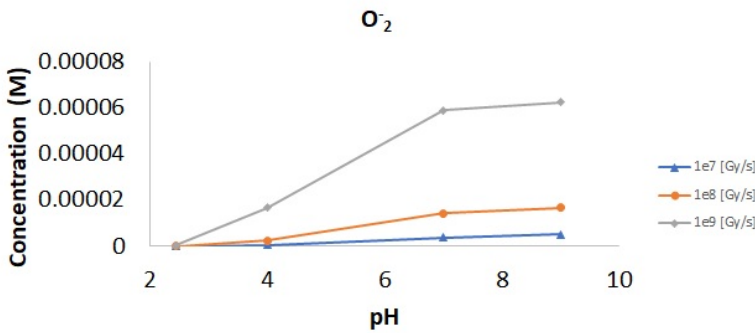Figure D.3: Concentration of O_2 with different dose rate and initial pH of solution

D

Figure D.4: Concentration of O_2^- with different dose rate and initial pH of solution

D.4. DOSE RATE CALCULATION

Dose rate and electron beam current calculation for different spot size with nano cell thickness of 200 and 500 nm.

Nano cell thickness:			500 nm	200 nm
Spot size	Exposure time (s)	Current (A)	Dose rate (Gy/s)	Dose rate (Gy/s)
3	1.3	3.8E-09	1.5E+08	8.6E+07
4	2.9	1.7E-09	7.0E+07	3.8E+07
5	5.8	8.4E-10	3.4E+07	1.8E+07
6	11	4.4E-10	1.8E+07	9.8E+06
7	19	2.6E-10	1.0E+07	5.8E+06

D.5. POTENTIAL FOR HYDROGEN, OXYGEN AND HYDROGEN ION

-

$$2H^+ + 2e^- \rightleftarrows H_2 \tag{D.1}$$

According to Nernst potential,

$$E = E^0 + \frac{RT}{nF} * (ln(H^+) - 0.5 * ln(pH_2)) \tag{D.2}$$

-

$$O_2 + 4H^+ + 4e^- \rightleftarrows 2H_2O \tag{D.3}$$

According to Nernst potential,

$$E = E^0 + \frac{RT}{nF} * (ln(H^+) + 0.25 * ln(pO_2)) \tag{D.4}$$

D.6. POTENTIAL CHANGE FOR TEM EXPERIMENT

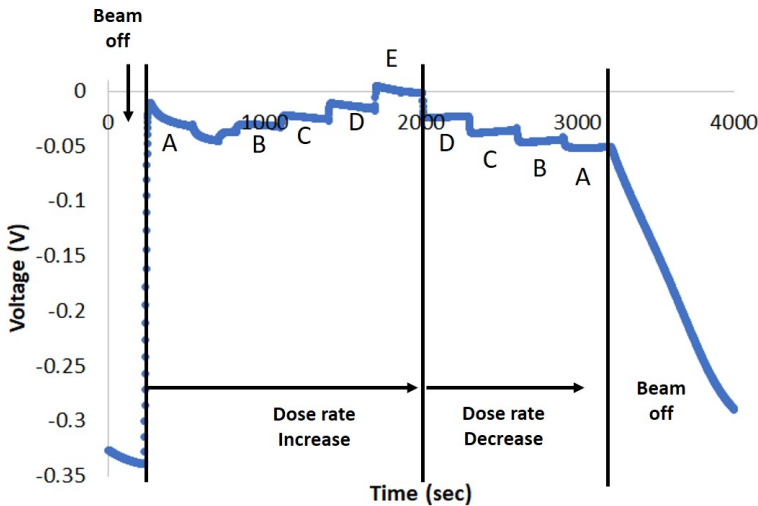Potential measurement for H_2SO_4 (pH 2.45) between WE and RE.

Figure D.5: Potential for H_2SO_4 (pH 2.45) between WE and RE, with changing electron beam spot size. A, B, C, D, E corresponds to spot size 7, 6, 5, 4, 3 respectively. Dose rate calculation for given spot size is given in appendix D.4.

Potential measurement for Ultra pure water + KCl (40 g/L) solution (pH 7.2) between WE and RE.
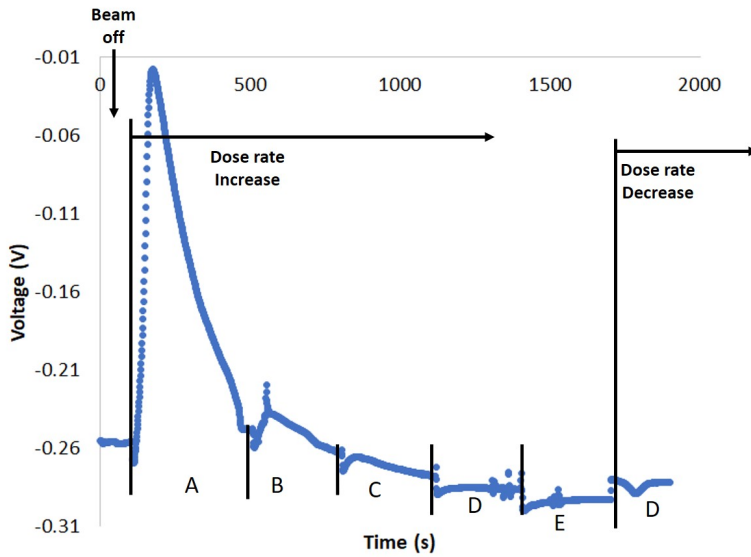
Figure D.6: Potential for Ultra pure water + KCl (40 g/L) solution (pH 7.2) between WE and RE, with changing electron beam spot size. A, B, C, D, E corresponds to spot size 7, 6, 5, 4, 3 respectively. Dose rate calculation for given spot size is given in appendix D.4.
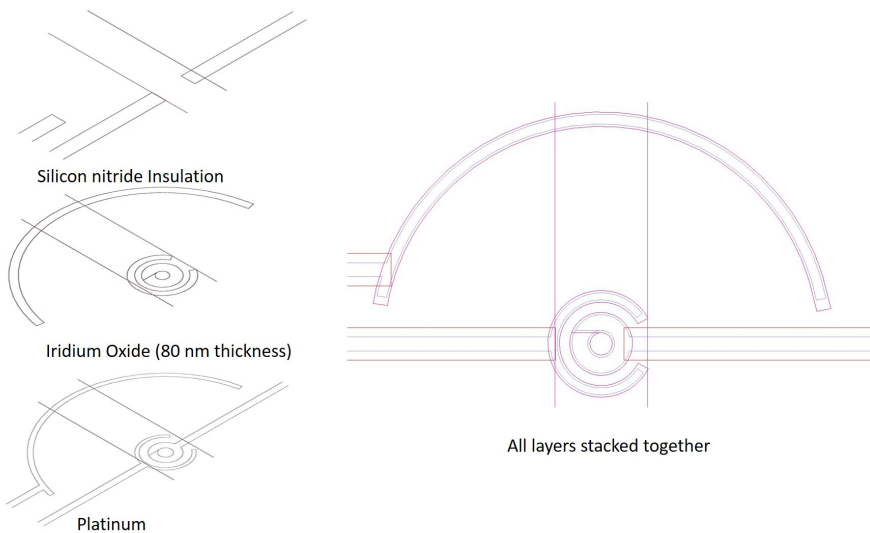
D.7. PH SENSOR CHIP DESIGN

Figure D.7: Layer by layer design of pH sensing electrodes